UCLA
UCLA Electronic Theses and Dissertations

Title
Spin-Orbit Torques in Topological Insulator-based Magnetic Structures

Permalink
https://escholarship.org/uc/item/7825b65f

Author
Fan, Yabin

Publication Date
2016

Peer reviewed|Thesis/dissertation

eScholarship.org Powered by the California Digital Library
University of California

UNIVERSITY OF CALIFORNIA

Los Angeles

Spin-Orbit Torques in Topological Insulator-based Magnetic Structures

A dissertation submitted in partial satisfaction of the

requirements for the degree Doctor of Philosophy

in Electrical Engineering

by

Yabin Fan

2016

© Copyright by

Yabin Fan

2016

ABSTRACT OF THE DISSERTATION

Spin-Orbit Torques in Topological Insulator-based Magnetic Structures

by

Yabin Fan

Doctor of Philosophy in Electrical Engineering

University of California, Los Angeles, 2016

Professor Kang Lung Wang, Chair

During recent years, enormous progress has been made in the spintronics research field which utilizes the spin degree of freedom of electrons in addition to their charge for information processing with the goal to achieve non-volatile spintronic memory and logic devices with fast speed, high density, good reliability and low power consumption. In particular, novel materials have been incorporated in the magnetic structures to realize manipulation and/or switch of magnetic moment using the least possible power. Among them, heavy metals and topological insulators (TIs), which exhibit strong spin-orbit coupling, have been employed to generate spin-orbit torques (SOTs) to enable efficient switching of magnetic moment, which may thus lead to the next generation green spintronic devices.

In this work, we will explore the current-induced SOTs in TI-based magnetic structures. First, we present the magnetization switching through giant SOT induced by an in-plane current in a TI/Cr-doped TI bilayer heterostructure. The critical current density required for switching is

below 8.9×10^4 A/cm^2 at 1.9 K. Both the effective spin-orbit field to current ratio and the spin-torque efficiency are found to be three orders of magnitude larger than those reported for conventional heavy metal/ferromagnet heterostructures.

Second, we show the effective electric-field control of the giant SOT in a uniformly Cr-doped TI thin film using a top-gate field-effect transistor structure. We demonstrate that the SOT strength can be modulated by a factor of 4 within the accessible gate voltage range, and it shows strong correlation with the spin-polarized surface current arising from surface spin-momentum locking in the film. Furthermore, we demonstrate the magnetization switching by scanning gate voltage with constant current and in-plane magnetic field applied in the Cr-doped TI thin film.

Last but not least, we summarize the research results and discuss future potential research opportunities and challenges in this field. There are still many unresolved questions in this new research field. Nevertheless, the giant current-induced SOT we have observed in TI-based magnetic structures suggests that it might have wide implications in the next generation gate-controlled, ultralow power spintronic devices.

The dissertation of Yabin Fan is approved.

Benjamin S. Williams

Louis-Serge Bouchard

Kang Lung Wang, Committee Chair

University of California, Los Angeles

2016

This dissertation is dedicated to my family,

for their unconditional love, encouragement and support.

TABLE OF CONTENTS

Abstract ii

Table of Contents vi

List of Figures ix

List of Tables xiii

Symbols and Acronyms xiv

Acknowledgements xvi

Vita xix

1. Introduction 1

 1.1 Introduction to Spin-Orbit Torques 1

  1.1.1 Spin-Transfer Torque 2

  1.1.2 Spin Hall Effect and Spin-Orbit Torques 4

  1.1.3 Spin-Orbit Torques in Materials beyond the Heavy Metals 9

 1.2 Introduction to Topological Insulators 11

  1.2.1 3-Dimentional Topological Insulators 13

  1.2.2 Surface Spin-Momentum Locking in 3-Dimensional Topological Insulators 16

 1.3 Motivation for Exploring Spin-Orbit Torques in Topological Insulator-based Magnetic Structures 20

 1.4 Dissertation Outline 22

2. Magnetization Switching through Giant Spin-Orbit Torque in a Magnetically Doped Topological Insulator Heterostructure....23
2.1 Overview 23
2.2 Topological Insulator/Cr-doped Topological Insulator Bilayer Heterostructure Magnetic Properties 26
2.3 Magnetization Switching through Giant SOT in the Bilayer Heterostructure 33
2.4 Second Harmonic Method to Evaluate the Current-induced Spin-Orbit Torques 39
2.5 Thermal Effect and Temperature Dependence of the Switching Current Density....55
2.6 Discussion on the Switching Process, the Anisotropic Magneto-Resistance (AMR) Effect and the Planar Hall Effect (PHE) in the Bilayer Heterostructure 60

3. Electric-Field Control of Spin-Orbit Torque in a Magnetically Doped Topological Insulator .66
3.1 Overview 66
3.2 Magnetization Switching through Current-induced Spin-Orbit Torque in the Al_2O_3/Cr-doped TI/GaAs (substrate) Structure 69
3.3 Electric-Field Effect on Material Properties of the Cr-doped Topological Insulator....79
3.4 Estimation of the Two Surfaces' Carrier Densities and Mobilities in the Cr-doped TI Film under Different Gate Voltages 86
3.5 Electric-Field Control of Spin-Orbit Torque and Magnetization Switching Behaviors in the Au(electrode)/Al_2O_3/Cr-TI/GaAs (substrate) Structure....92
3.6 Discussion on Correlations between the Topological Surface Current and the Electric-Field Control of Spin-Orbit Torque in the Structure 97

3.7 Comparison of the Current-induced Spin-Orbit Torques in Cr-doped TI Films Grown on GaAs Substrates with Smooth and Rough Surface Morphologies 101

4. Summary 107

4.1 Conclusion 107

4.2 Outlook 109

References 112

LIST OF FIGURES

Figure 1-1. Illustration of the current-induced STT and the 2-terminal MTJ structure..................3

Figure 1-2. Illustration of the SHE in a heavy metal and the 3-terminal MTJ structure based on current-induced SOT in high SOC material...6

Figure 1-3. Magnetization switching through SHE-induced SOT in the HMFHs with out-of-plane and in-plane anisotropies 8

Figure 1-4. 2-dimensional topological insulator band structure and the spin polarized edge channels...12

Figure 1-5. 3-dimensional topological insulator with bulk band inversion and surface spin-polarized Dirac states 15

Figure 1-6. Charge current-induced surface spin polarization in TI..17

Figure 1-7. Electrical detection of the spin-polarized surface states conduction in $(Bi_{0.53}Sb_{0.47})_2Te_3$...19

Figure 2-1. Various research topics in TI-based topological spintronics 24

Figure 2-2. HRSTEM and EDX spectrum of the $(Bi_{0.5}Sb_{0.5})_2Te_3/(Cr_{0.04}Bi_{0.57}Sb_{0.39})_2Te_3$ bilayer thin film...27

Figure 2-3. Experimental setup and magnetic properties of the $(Bi_{0.5}Sb_{0.5})_2Te_3$ $/(Cr_{0.08}Bi_{0.54}Sb_{0.38})_2Te_3$ bilayer heterostructure..29

Figure 2-4. Magneto-conductivity data showing similar conductivities for the 6 QL $(Bi_{0.5}Sb_{0.5})_2Te_3$ and the 6 QL $(Cr_{0.08}Bi_{0.54}Sb_{0.38})_2Te_3$ thin films on GaAs (111)B substrate at 1.9 K...32

Figure 2-5. Illustration of the spin accumulation in the Cr-doped TI layer and the resulted SOTs 34
Figure 2-6. Magnetization switching due to the SOT induced by an in-plane DC current in the TI/Cr-doped TI bilayer heterostructure..37
Figure 2-7. Equilibrium orientation of the magnetization in the presence of the external magnetic field and with/without the longitudinal current 42
Figure 2-8. Fitting to obtain the anisotropy coefficient and the saturation AHE resistance..........43
Figure 2-9. The orientation of the magnetization in the presence of a large in-plane external magnetic field B_y along the y-axis and an AC current, $I_{ac} = I_0 \sin(\omega t)$ 45
Figure 2-10. Second harmonic AHE resistance as a function of the in-plane external magnetic field 46
Figure 2-11. Harmonic signals and effective spin-orbit fields obtained from the rotation experiment...49
Figure 2-12. Second harmonic measurement to evaluate the field-like SOT 53
Figure 2-13. The coercivity field B_C as a function of the temperature 56
Figure 2-14. The critical switching current density and the anisotropy field coefficient as a function of temperature...57
Figure 2-15. The percentage change in R_{xx} as a function of the temperature and the current, respectively 59
Figure 2-16. Comparison of the phase diagrams obtained from the experiments and from the single domain simulations...62
Figure 2-17. Rotation experiment to obtain the AMR and PHE resistances 65

Figure 3-1. Various research topics in the field of electric-field control of magnetic properties in spintronics 67

Figure 3-2. Material properties and measurement set-up of the Al_2O_3(20nm)/Cr-TI(7nm)/GaAs(substrate) structure device 71

Figure 3-3. Determination of the out-of-plane anisotropy coefficient K and the saturation AHE resistance R_{AHE} 75

Figure 3-4. Current-induced magnetization switching and second harmonic measurements in the Al_2O_3(20nm)/Cr-TI(7nm)/GaAs(substrate) structure device....76

Figure 3-5. Top-gate Hall bar configuration and gate electric-field effect on material properties in the Au(electrode)/Al_2O_3(20nm)/Cr-TI(7nm)/GaAs(substrate) structure device 82

Figure 3-6. Curie temperature T_{C} as a function of gate voltage V_g in the Au(electrode)/Al_2O_3/Cr-TI/GaAs structure....85

Figure 3-7. SdH quantum oscillations from the top and bottom surface states in the $(Bi_{0.53}Sb_{0.47})_2Te_3$ thin film 90

Figure 3-8. Longitudinal sheet conductance and surface carrier mobility in the Cr-doped TI film under different gate voltages....91

Figure 3-9. Second harmonic measurements under different gate voltages and voltage-induced magnetization switching behaviors....95

Figure 3-10. Correlations between the surface carrier densities, surface currents, surface band structures and the measured electric-field control of SOT in the top-gate Hall bar device 99

Figure 3-11. Surface morphologies and interfacial properties of the Cr-doped TI films grown on GaAs (111)B substrates pre-annealed with / without Se vapor protection....104

Figure 3-12. Magneto-transport and second harmonic measurements in the Al_2O_3/Cr-TI/(rough GaAs substrate) structure 105

LIST OF TABLES

Table 1-1. Spin-torque ratios for different high SOC materials 10

Table 2-1. Electric properties of both the 6QL TI and the 6QL Cr-doped TI thin films at 1.9 K .32

Table 2-2. Comparison of the SOTs generated by TIs and heavy metals......................................54

Table 3-1. Comparison of the SOTs in TI/Cr-doped TI bilayer and uniformly Cr-doped TI........78

SYMBOLS AND ACRONYMS

1D/2D/3D	One-/Two-/Three-Dimensional
AFM	Atomic Force Microscope
AHE	Anomalous Hall Effect
ALD	Atomic Layer Deposition
AMR	Anisotropic Magneto-Resistance
ARPES	Angle-Resolved Photoemission Spectrum
BC	Bulk Conduction
BV	Bulk Valence
CMOS	Complementary Metal-Oxide-Semiconductor
Cr-TI	Cr-doped Topological Insulator
EDX	Energy-Dispersive X-ray
FET	Field-Effect Transistor
FIB	Focused Ion Beam
GMR	Giant Magneto-Resistance
HAADF	High Angle Annular Dark Field
HMFH	Heavy Metal/Ferromagnet Heterostructure
HRS	High-(magneto)-Resistance State
HRSTEM	High-Resolution Scanning Transmission Electron Microscopy
ISHE	Inverse Spin Hall Effect
LLG	Landau-Lifshitz-Gilbert
LRS	Low-(magneto)-Resistance State

MBE	Molecular Beam Epitaxy
MMM	Magnetism and Magnetic Materials
MR	Magneto-Resistance
MRAM	Magnetic Random Access Memory
MTJ	Magnetic Tunnel Junction
PHE	Planar Hall Effect
PPMS	Physical Property Measurement System
QL	Quintuple Layer
QSHE	Quantum Spin Hall Effect
RHEED	Reflection High-Energy Electron Diffraction
SdH	Shubnikov-de Haas
SHE	Spin Hall Effect
SOC	Spin-Orbit Coupling
SOT	Spin-Orbit Torque
SQUID	Superconducting Quantum Interference Device
SS	Surface States
ST-FMR	Spin Torque-Ferromagnetic Resonance
STT	Spin-Transfer Torque
TI	Topological Insulator
TMR	Tunneling Magneto-Resistance
TRS	Time-Reversal-Symmetry
YIG	Yttrium Iron Garnet
rms	root-mean-square

ACKNOWLEDGEMENTS

It has been a really wonderful experience to have my graduate studies in the DRL group, and I have received numerous help from many people here to make the work possible. I would love to especially thank my advisor, Prof. Kang L. Wang, for his continuous guidance, support and encouragement in both the academic research and the daily life, for leading me to this fascinating field of topological spintronics, for guiding me to overcome various difficulties in the research, and for challenging me to come up with better ideas. I have also learned a lot from Prof. Wang the principles and philosophy in managing the lab, organizing the research and interacting with different people, which I really appreciate and would benefit a lot for my future career.

I also would like to acknowledge Prof. Oscar M. Stafsudd, Prof. Benjamin S. Williams, and Prof. Louis-Serge Bouchard for serving as my doctoral committee members and giving me insightful comments and advice that greatly help me improve my work.

I am deeply grateful to my outstanding collaborators for their indispensable support and contribution to my research work. In particular, I acknowledge Prof. Yaroslav Tserkovnyak and Dr. So Takei at UCLA for substantial theoretical support, Prof. Yong Wang and Dr. Jun Liu at Zhejiang University for carrying out nice TEM characterization, Prof. Allan H. MacDonald and Dr. Massoud Ramezani Masir at UT Austin for more detailed theoretical explanation of the spin-orbit torque, Prof. Yugui Yao and Dr. Jianmin Zhang at Beijing Institute of Technology for *ab initio* calculations of the magnetic topological insulators, and many others.

I have the great pleasure to work with many talented students and postdocs in DRL at UCLA. In particular, I want to thank the MBE/TI sub-group for the collaborative work on spin-orbit torque. I want to thank Xufeng Kou, Liang He, Lei Pan and Koichi Murata for growing the

wonderful materials. I want to thank Qiming Shao for carrying out the delicate transport measurement. I would like to acknowledge Murong Lang and Xiaoyu Che for fabricating the beautiful devices. I also want to thank the other group members (Jianshi Tang, Li-Te Chang, Mohammad Montazeri, Tianxiao Nie, Kin L. Wong and Robert N. Schwartz) for their contributions to the measurement and analysis. I would like to specifically thank Pramey Upadhyaya and Igor Ovchinnikov for their in-depth theoretical analysis and support. Furthermore, I always enjoy the inspiring discussion and collaboration with the Spintronics sub-group (Guoqiang Yu, Mohammad Montazeri, Pramey Upadhyaya, Aryan Navabi) and the Carbon sub-group (Xiaodan Zhu, Caifu Zeng, Carlos Torres), and many other former colleagues including Wanjun Jiang, Zhenxing Wang, Mustafa Akyol as well as the other DRL members for their kind collaborations and support.

I acknowledge our staff members Eileen Panguito and Wendy Sanchez for their kind assistance and support in preparing many documents, paperwork and mailings in my graduate studies and research.

In this Dissertation, Chapter 2 is based on our manuscript titled with "Magnetization switching through giant spin-orbit torque in a magnetically doped topological insulator heterostructure" and Chapter 3 is based on our manuscript titled with "Electric-field control of spin-orbit torque in a magnetically doped topological insulator".

I also gratefully acknowledge sources of financial support for this work. Studies presented in Chapters 2&3 of this Dissertation are supported by the DARPA Meso program under contract No.N66001-12-1-4034 and N66001-11-1-4105, and the FAME Center, one of six centers of STARnet, a Semiconductor Research Corporation sponsored by MARCO and DARPA. The studies presented in Chapter 2 are also supported by the Western Institute of Nanoelectronics

(WIN). The studies presented in Chapter 3 are partially supported by the Spins and Heat in Nanoscale Electronic Systems (SHINES), an Energy Frontier Research Center funded by the U.S. Department of Energy (DOE), Office of Science, Basic Energy Sciences (BES), under Award # DE-SC0012670. I also acknowledge the support from the U.S. Army Research Office under grants W911NF-14-1-0607 and W911NF-15-1-0561.

Last but not least, I express my deepest love and special gratitude to my family for their unconditional love, encouragement and support.

VITA

Education

2012-2016	***Graduate Student Researcher*** in **Electrical Engineering** University of California, Los Angeles, USA
2009-2012	***M.S.*** in **Electrical Engineering** University of California, Los Angeles, USA
2005-2009	***B.S.*** in **Physics** Nankai University, Tianjin, P. R. China

Selected Publications

[1] **Y. Fan**, X. Kou, P. Upadhyaya, Q. Shao, L. Pan, M. Lang, X. Che, J. Tang, M. Montazeri, K. Murata, L. T. Chang, M. Akyol, G. Yu, T. Nie, K. L. Wong, J. Liu, Y. Wang, Y. Tserkovnyak and K. L. Wang, "Electric-field control of spin-orbit torque in a magnetically doped topological insulator", ***Nature Nanotechnology*** **11**, 352-359 (2016).

[2] **Y. Fan**, *et al.*, "Enhanced Surface-related Magnetism in a Topological Insulator with Optimal Magnetic δ-doping", *ready for submission to* ***Solid State Communications*** (2016).

[3] X. Kou, L. Pan, J. Wang, **Y. Fan**, E. S. Choi, W. L. Lee, T. Nie, K. Murata, Q. Shao, S.-C. Zhang & K. L. Wang, "Metal-to-insulator switching in quantum anomalous Hall states", ***Nature Communications*** **6**:8474 (2015).

[4] M. Montazeri, P. Upadhyaya, M. C. Onbasli, G. Yu, K. L. Wong, M. Lang, **Y. Fan**, X. Li, P. K. Amiri, R. N. Schwartz, C. A. Ross & K. L. Wang, "Magneto-optical investigation of spin-orbit torques in metallic and insulating magnetic heterostructures", ***Nature Communications*** **6**:8958 (2015).

[5] **Y. Fan**, P. Upadhyaya, X. Kou, M. Lang, S. Takei, Z. Wang, J. Tang, L. He, L. T. Chang, M. Montazeri, G. Yu, W. Jiang, T. Nie, R. N. Schwartz, Y. Tserkovnyak and K. L. Wang, "Magnetization switching through giant spin-orbit torque in a magnetically doped topological insulator heterostructure", ***Nature Materials*** **13**, 699-704 (2014).

[6] X. Kou[†], S. T. Guo[†], **Y. Fan**[†], L. Pan, M. Lang, Y. Jiang, Q. Shao, T. Nie, K. Murata, J. Tang, Y. Wang, L. He, T. K. Lee, W. L. Lee, and K. L. Wang, "Scale-Invariant Quantum

Anomalous Hall Effect in Magnetic Topological Insulators beyond the Two-Dimensional Limit", ***Phys. Rev. Lett.*** **113**, 137201 (2014). (†: **equal first authors**)

[7] G. Yu, P. Upadhyaya, **Y. Fan**, J. G. Alzate, W. Jiang, K. L. Wong, S. Takei, S. A. Bender, L. T. Chang, Y. Jiang, M. Lang, J. Tang, Y. Wang, Y. Tserkovnyak, P. K. Amiri and K. L. Wang, "Switching of perpendicular magnetization by spin-orbit torques in the absence of external magnetic fields", ***Nature Nanotechnology*** **9**, 548-554 (2014).

[8] W. Jiang, P. Upadhyaya, **Y. Fan**, J. Zhao, M. Wang, L. T. Chang, M. Lang, K. L. Wong, M. Lewis, Y. T. Lin, J. Tang, S. Cherepov, X. Zhou, Y. Tserkovnyak, R. N. Schwartz, and K. L. Wang, "Direct Imaging of Thermally Driven Domain Wall Motion in Magnetic Insulators", ***Phys. Rev. Lett.*** **110**, 177202 (2013).

[9] **Y. Fan,** I. V. Ovchinnikv, W. Jiang, R. N. Schwartz, and K. L. Wang, "Fluctuations in nanoscale magnetoelectronics devices", ***J. Appl. Phys.*** **112**, 094302 (2012).

Conference Presentations

[1] **Y. Fan**, **MMM invited talk** "Current-induced spin-orbit torque in magnetically doped topological insulators", ***2016 MMM-Intermag Joint Conference***, San Diego, California, (Jan. 11-15, 2016).

[2] **Y. Fan**, *et al.*, "Electric-field control of spin-orbit torque in magnetically doped topological insulators", ***APS March Meeting***, Baltimore, Maryland, (Mar. 14-18, 2016).

[3] **Y. Fan**, **APS invited talk** "Magnetization switching through giant spin-orbit torque in the magnetically doped topological insulators", ***APS March Meeting***, San Antonio, Texas, (Mar. 2-6, 2015).

[4] **Y. Fan**, *et al.*, "Spin-orbit torque induced magnetization switching in magnetically doped topological insulators", ***59th Annual Conference on Magnetism and Magnetic Materials (MMM)***, Honolulu, Hawaii, (Nov. 3-7, 2014), **Best Student Presentation Finalist Award**.

[5] **Y. Fan**, *et al.*, "Current-induced Giant Spin-Orbit Torque in a Magnetically Doped Topological Insulator Heterostructure", ***APS March Meeting***, Denver, Colorado, (Mar. 3-7, 2014).

Chapter 1

Introduction

1.1 Introduction to Spin-Orbit Torques

Spintronics is a research field that utilizes the spin and charge degrees of freedom to control equilibrium and non-equilibrium properties of magnetic materials and devices [1-3]. The spintronics research field has developed very fast in the past decade with outcome technologies that have high potential to replace the conventional complementary metal-oxide-semiconductor (CMOS) technology [4]. The generation of spin current and use of it to control magnetization dynamics is one of the key objectives in the spintronics research field, with the aim to develop non-volatile spintronic memory and logic devices with faster speed, higher density, better reliability and lower power consumption as compared with today's CMOS devices [5-7]. Among the notable spintronic technologies developed so far, spin-transfer torque (STT) [7,8], *i.e.*, transfer of spin angular momentum from the spin current to the adjacent magnetic moment, offers one effective way to control the magnetization dynamics electrically. Besides STT, people have developed more advantageous ways to generate spin torque by employing high spin-orbit coupling (SOC) materials, and the spin torque exerted on an adjacent magnet by the applied current is hereby named spin-orbit torque (SOT) [9]. The SOT can be used to manipulate or even switch a magnet with far greater efficiency. Therefore, it has attracted extensive research interest during the past few years and shows promising application potential on the next-generation magnetic memory and logic devices. In the following sub-sections, we will briefly introduce the research status on both STT and SOT.

1.1.1 Spin-Transfer Torque

In 1989, Slonczewski *et al.* first theoretically predicted that STT could happen between conduction electrons and magnetization: spin-polarized electrical currents can transfer spin angular momentum to the magnetic moments of a ferromagnet, thus reorienting them [10-12]. When the spin polarization of the electrons incident on a magnetic layer is not aligned with its magnetization, as shown in Fig. 1-1(a), the electron spin precesses quickly around a momentum-dependent internal field of the ferromagnet. Electron spins dephase rapidly because of the distribution of electron momenta associated with the current flow [13]. As a result, the component of spin polarization transverse to the magnetization decays, transferring spin angular momenta to the ferromagnet. The change in spin polarization between the outgoing electrons and the incident electrons thus causes torques on the ferromagnet [14], both a torque lying in the plane of the incident and outgoing electron spin directions, called the STT, and a torque perpendicular to that plane, called the field-like torque, as illustrated in Fig. 1-1(a).

STT can provide an efficient means to reorient the magnetization direction. In 1999, Ralph group demonstrated the STT-induced magnetization switching in a Co/Cu/Co sandwich structure [15,16]. After that, rapid growth in the field of STT-driven magnetization dynamics emerged, especially in the magnetic tunnel junction (MTJ) structure which is made of a ferromagnetic metal/insulator/ferromagnetic metal stack [17]. The MTJ structure is a crucial element in the STT magnetic random access memory (MRAM) bit cell. As shown in Fig. 1-1(b), the orientation of magnetization of one electrode in the MTJ junction is fixed (the fixed layer) and serves as a reference layer that sets the spin-polarization direction of the incident current. The other magnetic electrode acts as a 'free layer" in which the information can be stored. The incident spin-polarized current I_S can exert STT on the free layer and switch its magnetization direction

(the write process). The information is encoded in the tunneling magnetoresistance (TMR) which refers to the percentage change in resistance between parallel and antiparallel magnetization alignment of the electrodes in the MTJ. Until 2004, the maximum TMR reported [18-20] at room temperature was 70%. TMR greater than 100% had, however, been predicted in crystalline Fe/MgO/Fe tunnel junctions [21] and was then observed experimentally [22,23]. Subsequent rapid advances in the growth of thin-film materials have led to junctions with large TMR of several hundred percent, through the use of transition metal electrodes (typically CoFeB).

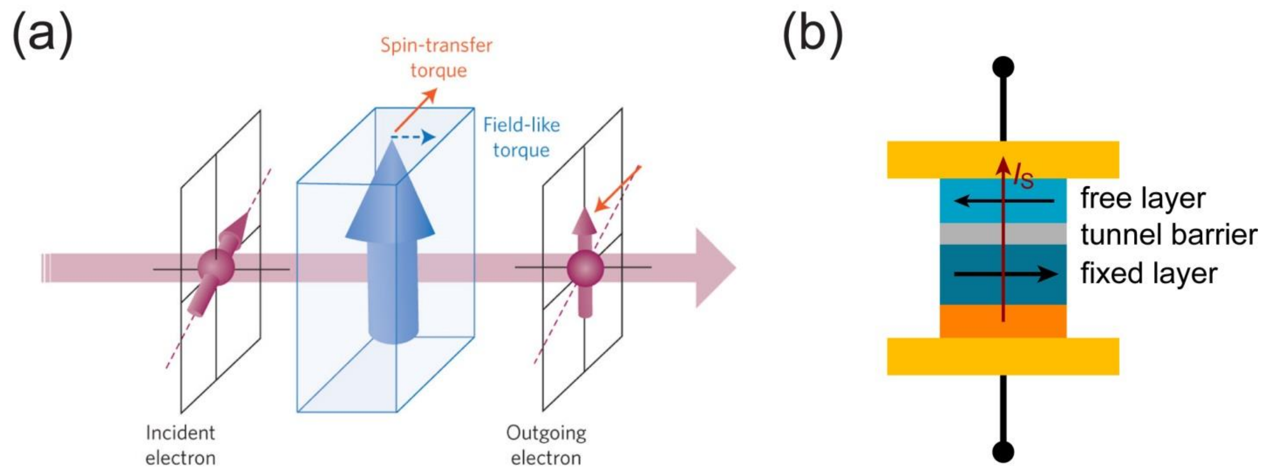

Figure 1-1. Illustration of the current-induced STT and the 2-terminal MTJ structure. (a) A spin-polarized current applies torques on a ferromagnet: a STT lying in the plane of the incident and outgoing electron spin directions and a field-like torque perpendicular to that plane. The bold vertical arrow is the magnetization of the ferromagnet. This figure is adapted with permission from ref. [14]. (b) 2-terminal MTJ structure consisting of the fixed magnetic layer, the tunnel barrier and the free magnetic layer. A spin current I_S polarized by the fixed layer can exert STT on the free layer and switch its magnetization.

1.1.2 Spin Hall Effect and Spin-Orbit Torques

Although the 2-terminal STT-based MTJ structure has many advantages as compared with traditional charge-based memory cell, it has an intrinsic electrical wear-out problem, that is, the dielectric breakdown of the MgO tunnel barrier due to the large current passing through in the 'write' process [24]. In the 2-terminal MTJ, it is also a challenge to achieve reliable reading of the MTJ resistance without ever causing switching. To avoid these problems, people have explored different ways to generate spin torque without large current traversing the tunnel barrier in MTJ. Among them, SOT [9,25,26] generated by high SOC materials offers a good solution. In particular, spin Hall effect (SHE) in heavy metals has been employed to generate SOT, and it shows tremendous success during the past few years. SHE-induced SOT can effectively manipulate and switch the magnetization in a heavy metal/ferromagnet heterostruture (HMFH), suggesting promising applications in the novel magnetic memory devices. In the following, we briefly discuss the SHE mechanism in heavy metals and the magnetization switching experiments based on the SHE-induced SOT.

In nonmagnetic materials with strong relativistic SOC, the electrons' spin degree of freedom is highly coupled with their orbital momentum. Typically in heavy metals with strong SOC, when passing a charge current through them, the incident electrons will feel an effective spin-orbit field arising from the large SOC. As a result, a certain percentage of the incident electrons will be deflected to the transverse directions, and this effect is called the SHE [27-31]. Since the effective spin-orbit field direction depends on the electron's spin direction, incident electrons with opposite spins will be deflected to opposite transverse directions, forming a spin current perpendicular to the incident charge current. Why there is an effective spin-orbit field for

the incident electrons in heavy metals with strong SOC? People have proposed both intrinsic and extrinsic mechanisms and they have been investigated experimentally.

According to the theory, in the intrinsic mechanism (*i.e.*, the intrinsic SHE) [32,33] which exists in the perfect single-crystalline metals, the effective spin-orbit field arises because of the momentum-space Berry phase contribution [27,34] to the spin Hall conductivity since some bands are mixed/connected via SOC in heavy metals below or near the Fermi level. When calculating the spin Hall conductivity using the Kubo formula, the band mixing/connection below the Fermi level in the Brillouin zone will give rise to a Berry phase term. This nontrivial term is a manifestation of the interband coherence during transport in highly spin-orbit coupled materials. On the other hand, in the extrinsic mechanism (*i.e.*, the extrinsic SHE) [35-37], the spin-dependent scatterings, *e.g.*, the skew scattering or side-jump in the presence of defects or impurities in heavy metals [34], can induce the effective spin-orbit field and incident electrons with different spins will be deflected to opposite transverse directions during the scattering events. Both the intrinsic and extrinsic SHE can produce a transverse spin current. In Fig. 1-2(a), we illustrate the SHE in a heavy metal: when passing a charge current (with density J_C) through the heavy metal along the $-y$ direction, incident electrons with opposite spins (pointing along $-x$ and x axes) are deflected to opposite transverse directions (z and $-z$ directions), resulting in a spin current (with density J_S) along the z-direction.

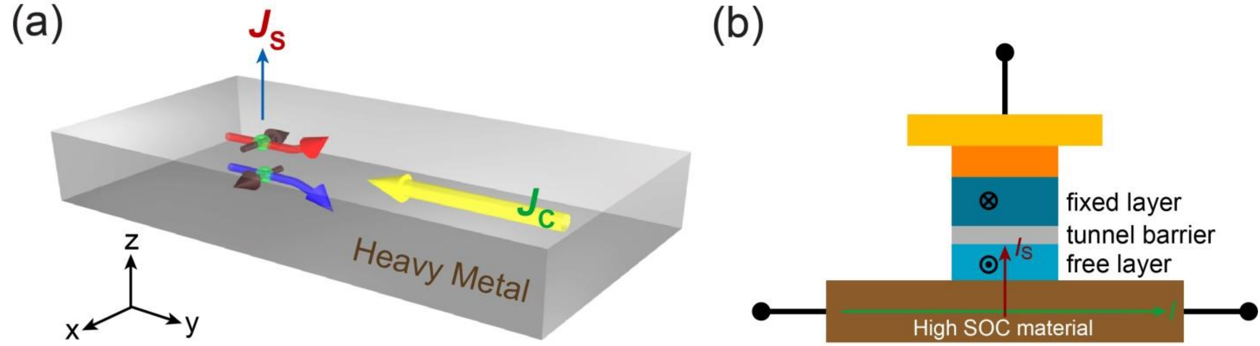

Figure 1-2. Illustration of the SHE in a heavy metal and the 3-terminal MTJ structure based on current-induced SOT in high SOC material. (a) A charge current (with density J_C) passes through the heavy metal along the $-y$ direction. Due to the SHE, incident electrons with different spins are deflected to opposite transverse directions (z and $-z$ directions), which leads to a spin current (with density J_S) along the z-direction. (b) 3-terminal MTJ structure consisting of the fixed magnetic layer, the tunnel barrier, the free magnetic layer and the high SOC material. Charge current passing through the high SOC material can generate a transverse spin current I_S which applies SOT on the free layer and switch its magnetization.

Now let us see how the SHE-induced SOT by heavy metals can solve the dielectric breakdown problem in the 2-terminal MTJ structure as mentioned before. Different from the 2-terminal MTJ structure, the SOT-based MTJ uses 3-terminal structure, as shown in Fig. 1-2(b). During the operation, a lateral current I will pass though the heavy metal layer (or in general, a high SOC material), and a perpendicular spin current I_S will be generated. I_S will exert a SOT on the adjacent free magnetic layer and switch its polarization, as illustrated in Fig. 1-2(b). In this 3-terminal MTJ structure [7,38], the 'read' current path and the 'write' current path are well separated and the SOT is generated without charge current traversing the tunnel barrier. This separation can significantly improve the MTJ reliability while also giving better output signal.

In real experiment, the SHE was first detected in semiconductors with large SOC (*e.g.*, GaAs and InGaAs) using optical method [39,40]. Later, it was discovered in heavy metals (*e.g.*, Pt and Ta) through many experiments [38,41-43] and has ignited extensive research interest. Among all the experiments related to the SHE in heavy metals (*e.g.*, SHE-induced magnetization switching [38,41-43], tuning of magnetic damping [44-47] and spin wave attenuation [48,49], excitation of spin wave oscillations [50], magnetic precession [45], and magnetic domain wall motion [51-53], *etc.*), the SHE-induced magnetization switching in HMFHs provides the most direct evidence of the SOT generated by the SHE in heavy metals and suggests very promising device applications such as the 3-terminal MTJ structures based on HMFHs. In the following, we briefly discuss the representative SHE-induced magnetization switching experiments achieved in HMFHs.

First, as shown in Fig. 1-3(a), in a Pt/Co/Al_2O_x hetrostructure which exhibits out-of-plane anisotropy due to the interfacial SOC, the Co magnetization can be deterministically switched by a positive or negative current pulse in Pt in the presence of an in-plane magnetic field applied along the current direction, as evidenced by the Hall resistance in Fig. 1-3(b). The switching is due to the SHE-induced SOT from the Pt layer. This switching was first reported by Miron *et al.* [41] and was further investigated and clarified by Liu *et al.* [42]. In addition, in Liu's another work [38], the 3-terminal MTJ structure composed of Ta/CoFeB(free layer)/MgO/CoFeB(fixed layer)/(Ta/Ru) was studied, as depicted in Fig. 1-3(c). The in-plane magnetized nano-magnet CoFeB(free layer) can be switched back and forth depending on the lateral current direction applied through the Ta layer, as demonstrated by the hysteretic TMR plotted in Fig. 1-3(d). This experiment demonstrates the pronounced SHE-induced SOT from Ta. The above switching experiments suggest promising applications of SHE in novel MRAM devices [7]. From then, the SHE-related research in HMFHs has become a flourishing topic in the spintronics field.

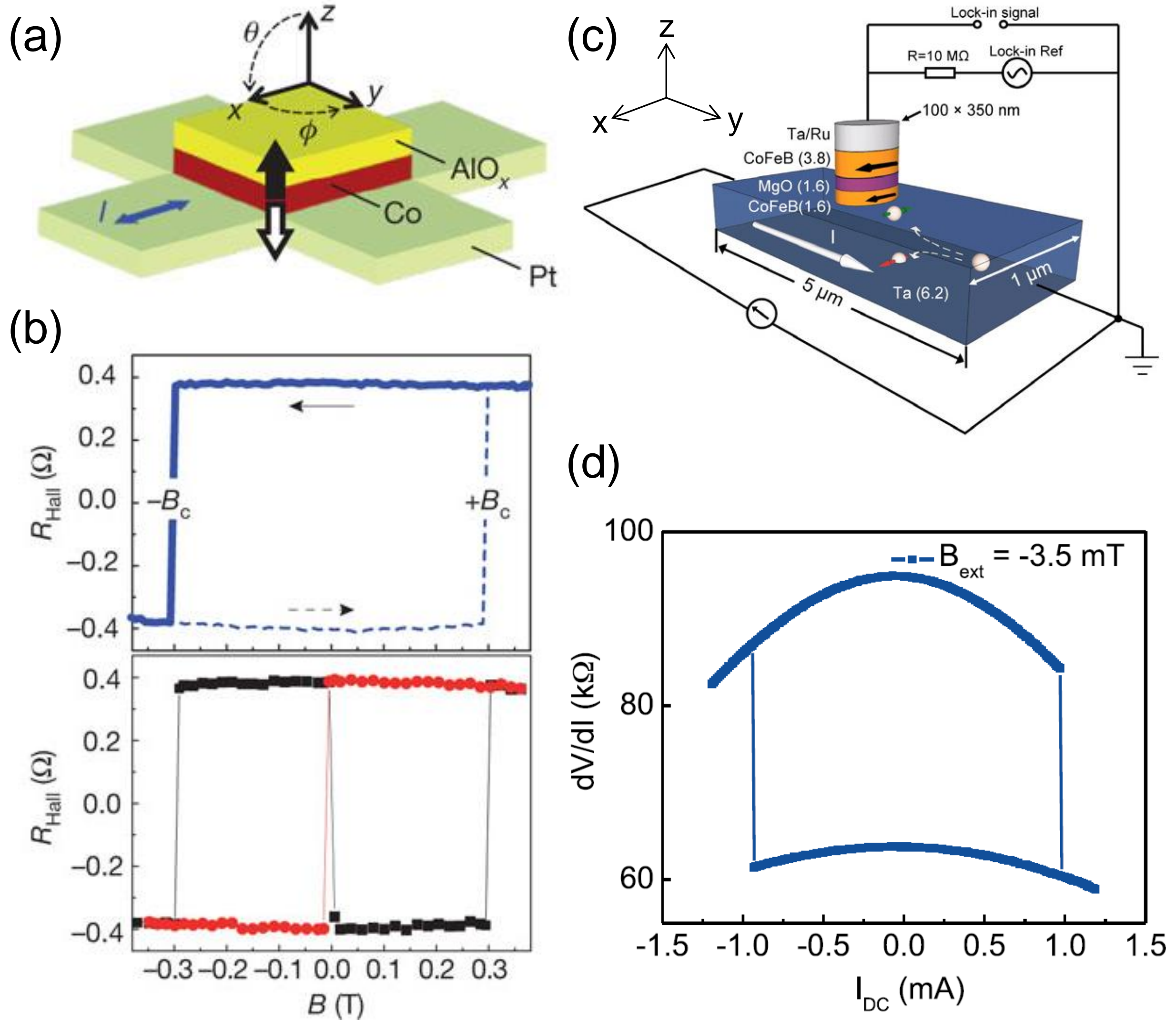

Figure 1-3. Magnetization switching through SHE-induced SOT in the HMFHs with out-of-plane and in-plane anisotropies. (a) Hall cross geometry made of Pt/Co/AlO$_x$ with out-of-plane anisotropy. Black and white arrows indicate the ‘up’ and ‘down’ equilibrium magnetization states of the Co layer, respectively. (b) Upper: z-component magnetization M_z measured by the anomalous Hall resistance as a function of applied field, **B**. Lower: switching of M_z through the injection of positive (black squares) and negative (red circles) current pulses of amplitude I_p = 2.58 mA. The data are reported during a single sweep of **B**, corresponding to the solid line in the upper panel. In both panels, **B** is applied at θ=92°, parallel to the current direction (ϕ=0°). The 2°

offset with respect to the ideal in-plane direction is used to define the residual component B_z unambiguously. Both (a) and (b) are adapted with permission from ref. [41]. (c) Schematic of the 3-terminal MTJ device composed of Ta/CoFeB/MgO/CoFeB/(Ta/Ru) with in-plane anisotropy, and the circuit for measurements. (d) TMR of the device as a function of the applied dc current I_{DC}, demonstrating the SHE-induced switching for the in-plane magnetized CoFeB at room temperature. Both (c) and (d) are adapted with permission from ref. [38].

1.1.3 Spin-Orbit Torques in Materials beyond the Heavy Metals

As we have introduced before, heavy metals can generate efficient SOT through the SHE and enable effective manipulation of magnetization in HMFHs. Besides heavy metals, people have explored other new materials that can generate more efficient SOT through more advanced mechanisms. Among them, topological insulators (TIs) have stood out and caught people's attention. Distinct from heavy metals, TIs not only have very strong SOC, but also possess the unique spin-momentum locked Dirac fermions on the surface [54-56], which make them very promising for generating SOT when passing a charge current through the surface. Indeed, in several experiments [57-65,66], TIs have shown the capability of generating SOT with much better efficiency as compared to heavy metals. In this dissertation, we will specifically report the giant SOT that has been measured in the magnetic TI-based structures.

Before going to the detail, we would like to briefly highlight the efficiency of TIs for generating SOT, namely, the spin-torque ratio ϑ_{ST} [59] (in the heavy metal case, it evolves to the spin Hall angle ϑ_{SH}) which is a measure of the amount of torque that can be generated per unit charge current density. ϑ_{ST} is defined as $\vartheta_{\mathrm{ST}} = \left(\frac{2e}{\hbar}\right) J_{\mathrm{S}}/J_{\mathrm{C}}$, where e is the electron charge, $\hbar$ is the reduced Planck constant, J_{C} and J_{S} are the charge current density applied through the material

and the generated transverse spin current density, respectively. As shown in Table 1-1, we can clearly see that the spin-torque ratios in TIs [57-59] are much larger (almost three orders of magnitude larger) than those reported in heavy metals, suggesting that TIs are much more efficient materials for generating SOT than heavy metals. We note that when considering the 2-dimensional (2D) nature of the surface states in TIs, people also use the characteristic length (*e.g.*, the inverse Edelstein effect length λ_{IEE} as reported in ref. [65]) to quantify the SOT efficiency. This characteristic length can be transformed to the spin-torque ratio if the TI's surface states penetration depth is taken into account. Since TIs are very promising materials for generating SOT for spintronic applications, we will give a more detailed introduction to them and their surface states properties in the next section.

Table 1-1. Spin-torque ratios for different high SOC materials

Materials	$(Bi, Sb)_2Te_3$ (refs. [57,58])	Bi_2Se_3 (ref. [59])	β-Ta (ref. [38])	β-W (ref. [67])	Pt (ref. [45])	Cu(Bi) (ref. [68])
ϑ_{ST}	116-425	2.0-3.5	0.15	0.3	0.08	0.24

1.2 Introduction to Topological Insulators

Topological insulators (TIs) are a new class of materials. The name of TIs originates from the fact that these materials have an insulating energy gap in the bulk but possess the topologically protected metallic states at the boundaries when they are placed next to vacuum or an ordinary insulator [54-56]. The reason for these materials to have the peculiar properties is that they have an inverted band structure in the bulk which is caused by the strong SOC in these materials [69,70]. In normal semiconductors, the conduction band which is formed from electrons in s-type orbitals (wavefunctions have even parity) is always above the valence band that is formed from electrons in p-type orbitals (wavefunctions have odd parity), *i.e.*, the band gap E_g is positive. However, in TIs, which contain heavy elements, the SOC is so strong that the p-type orbital band is pushed above the s-type orbital band----that is, the bands are inverted (*i.e.*, the band gap E_g is negative). As a result, TIs' bulk band topology in the $\mathbf{k}$-space is different from that of conventional semiconductors. When we connect TIs with materials exhibiting a positive energy gap, due to the continuity of wavefunctions of the same parity at the boundary, the energy gap is expected to close and exotic edge/surface states are expected to emerge at the interface.

The above scenario was first theoretically proposed [71] and experimentally realized [72] in a 2D TI material, the CdTe/HgTe/CdTe quantum well [71-74]. When the HgTe quantum well is thicker than 6.3 nm (critical value), the HgTe has a negative energy gap; on the other hand, CdTe is an ordinary insulator which has a positive energy gap. Consequently, in the theoretical calculation, gapless metallic edge states are well resolved in addition to the ordinary parabolic bulk band in the quantum well, as shown in Fig. 1-4(a). Due to the linear $E-k$ dispersion relation, these edge electrons can be viewed as massless Dirac fermions. More strikingly, due to the strong SOC, the edge states are spin-momentum locked: for the right-moving edge mode (red

line), spin is polarized down while for the left-moving edge mode (blue line), spin is polarized up. Every edge mode contributes to one quantum conductance. Due to the spin-momentum locking feature and the protection of time-reversal-symmetry (TRS), the edge modes experience no back-scattering by non-magnetic impurities during the transport process. This leads to exactly the quantum spin Hall effect (QSHE), as illustrated in Fig. 1-4(b), where dissipationless helical spin-polarized conduction is realized without the presence of any external magnetic field [72]. The HgTe quantum well, as a successful implementation of the QSHE insulator (*i.e.*, a 2D TI), has inspired extensive research interest on TI materials. Due to the exotic properties, TI has generated broad interest not only in spintronics, but also among condensed matter physics, material science, and ultralow-dissipation device applications. Moreover, it has also expanded to the 3-dimensinal (3D) regime as we will introduce below.

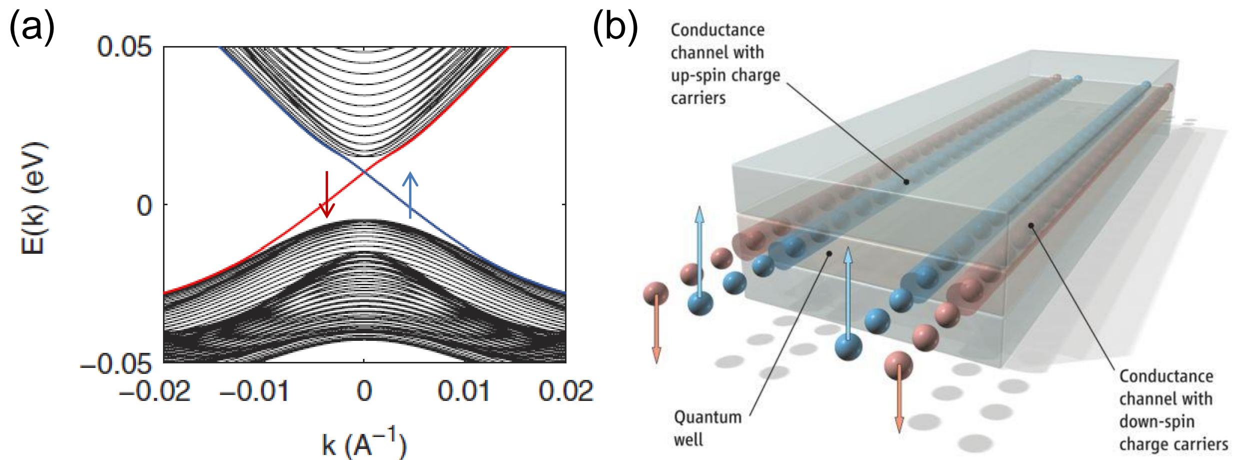

Figure 1-4. 2-dimensional topological insulator band structure and the spin polarized edge channels. (a) The energy band spectrum of a 2D TI, the HgTe quantum well. Blue and red lines show the edge states. Figure is adapted with permission from ref. [75]. (b) Schematic of the spin-polarized edge channels in a 2D TI, the HgTe quantum well. Figure is adapted with permission from ref. [72].

1.2.1 3-Dimensional Topological Insulators

From the above section, we see that the band inversion due to strong SOC in 2D materials gives rise to the QSHE insulators (*i.e.*, 2D TIs). In this section, we will show that the same principle can also be applied to construct 3D TIs where the topological nontrivial boundaries become 2D surface states instead of 1-dimensional (1D) edge channels. Basically, in 3D materials with strong enough SOC, the energy gap in the bulk can also be inverted. For example, displayed in Fig. 1-5(a) is the energy band evolution from atomic energy levels in Bi_2Se_3, which has strong SOC, as obtained by theoretical calculations [69]. Before turning on the SOC interaction in stage IV, the first three stages (stage I, the hybridization of Bi and Se orbitals; stage II, the formation of chemical bonding and antibonding states; stage III, the crystal-field splitting effect) lead to $|P1_z^+ >$ above the Fermi energy and $|P2_z^- >$ below the Fermi energy. $|P1_z^+ >$ and $|P2_z^- >$ are the p_z components of the hybridized states from Bi and Se atoms, and they are the closest states to the Fermi energy. The superscripts $+,-$ stand for even and odd parities, respectively. As shown in Fig. 1-5(a), in stage IV when the strong SOC is turned on, $|P1_z^+ >$ is pushed down below the Fermi energy while $|P2_z^- >$ is pushed up above the Fermi energy, thus leading to an inverted band order in the bulk of Bi_2Se_3 which is analogous to the band inversion in the 2D topological insulator HgTe quantum well.

Since the bulk band is inverted in Bi_2Se_3, its topology in the momentum space is different from that of ordinary semiconductors. Similar to the 2D HgTe quantum well case, when Bi_2Se_3 is placed next to vacuum or an ordinary semiconductor, due to the continuity of wavefunctions of the same parity at the boundary, the energy gap is expected to close and nontrivial surface states are expected to emerge at the interface. Indeed, according to the theoretical calculations, the surface states can be described by the Hamiltonian [54,55,69,70,76]: $H_{\mathrm{surf}}(k_x, k_y) = \hbar v_{\mathrm{D}}(\sigma^x k_y -$

$\sigma^y k_x)$, where $\hbar$ is the reduced Planck constant, v_D is the surface electron velocity, k_x and k_y are the electron momentum on the surface of Bi_2Se_3 and σ^x and σ^y are the Pauli matrices denoting the electron spin. The linear *E*-*k* relation gives rise to the Dirac cone dispersion on the surface of Bi_2Se_3, as shown in Fig. 1-5(b), and the surface electrons can be regarded as massless Dirac fermions. More importantly, the Dirac Hamiltonian naturally gives rise to the spin-momentum locking feature of the surface states, namely, the Dirac electron's spin is locked perpendicular to its momentum in the **k**-space, and the spin texture is clockwise above the Dirac point while anti-clockwise below the Dirac point, as illustrated in Fig. 1-5(b). These features make Bi_2Se_3 a perfect 3D TI material. Besides Bi_2Se_3, other binary compound such as Bi_2Te_3 and Sb_2Te_3 [54,69,77-81], and their derivatives are also reported to be 3D TIs.

To demonstrate the existence of topological surface states, people have used the surface-sensitive angle-resolved photoemission spectroscopy (ARPES) to probe them [78-86]. ARPES is a photon-in electron-out spectroscopy based on the photoelectric effect. An incoming photon, generated in X-ray sources or laser systems, is directed at a sample where it is absorbed. If the photon supplies sufficient energy to the electron, it can overcome the work function and exit the sample as a photoelectron. A movable detector, equipped with an energy filter, captures the photoelectrons in a specific energy range and solid angle. Using conservation of momentum and energy, one can then deduce information about the electron's initial momentum, energy and therefore information about the underlying electronic structure, such as the surface states in TIs. Indeed, from the ARPES measurement the linear Dirac dispersion (surface states) as well as the parabolic bulk bands in Bi_2Se_3 can be well resolved [80,81], as shown in Fig. 1-5(c), demonstrating that Bi_2Se_3 is a robust 3D TI material. Moreover, by using the spin-resolved ARPES [82,85], as shown in Fig. 1-5(d), the spin-momentum locking feature of the surface states is also confirmed.

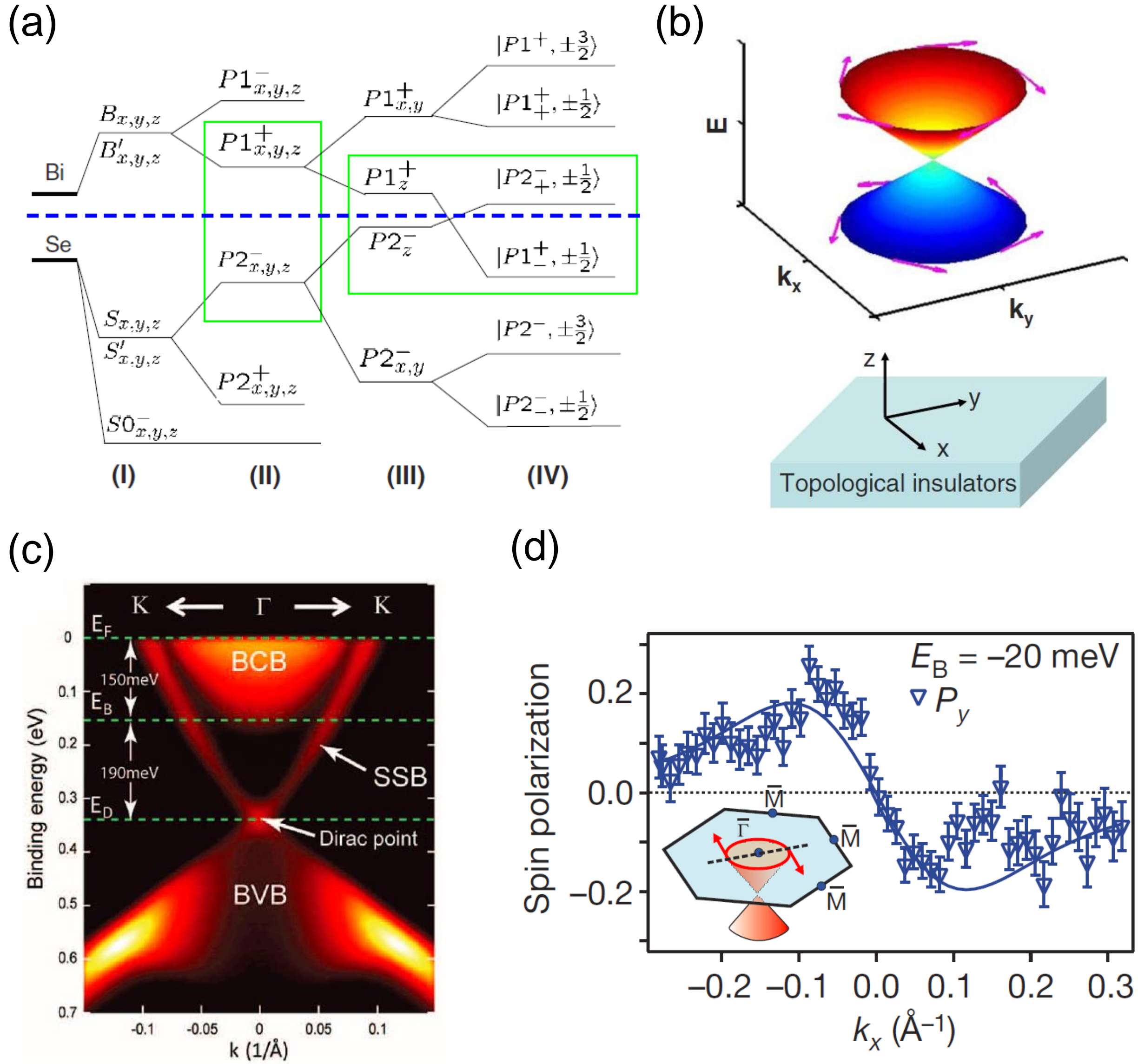

Figure 1-5. 3-dimensional topological insulator with bulk band inversion and surface spin-polarized Dirac states. (a) Schematic picture of the origin of the band structure of Bi_2Se_3: (I) the hybridization of Bi orbitals and Se orbitals, (II) the formation of the bonding and antibonding states due to the inversion symmetry, (III) the crystal field splitting, and (IV) the influence of the SOC. (b) Spin texture of the surface states near the Γ point in Bi_2Se_3. For the conduction band, the helicity is left handed while for the valence band, it is right handed. (a) and (b) are adapted with permission from ref. [76]. (c) ARPES measurement of electronic band structure of Bi_2Se_3

along the K-Γ-K direction, where Γ is the center of the hexagonal surface Brillouin zone. Figure is adapted with permission from ref. [80]. (d) Measured *y* component of spin-polarization along the Γ-M direction at E_B=-20 meV in Bi_2Te_3, which only cuts through the surface states. Inset: schematic of the cut direction. Figure is adapted with permission from ref. [82].

1.2.2 Surface Spin-Momentum Locking in 3-Dimensional Topological Insulators

Besides the optical approaches to probe the surface states spin-momentum locking, such as spin-resolved ARPES [82,85] and circularly-polarized light induced photocurrent on the TI surface [87-89], another important method to detect the surface states spin-momentum locking is to use electrical transport measurement. When a lateral electric field is applied on the TI surface, due to the spin-momentum locking feature of the surface states (Fig. 1-6(a)) and electric field-induced shift of Fermi surface in the **k**-space, there is a certain spin polarization associated with the surface charge current [90], and the spin polarization direction is governed by the charge current direction. For example, when the surface charge current is flowing along the $-x$ direction (*i.e.*, $I_x < 0$), as shown in Fig. 1-6(b), the Dirac electrons' spin is polarized along the $-y$ direction; likewise, when the surface charge current direction is reversed (*i.e.*, $I_x > 0$), as shown in Fig. 1-6(c), the Dirac electrons' spin polarization is also flipped (*i.e.*, pointing along the y direction). In short, the unique spin-momentum locking feature of the surface states in 3D TIs make them perfect candidates for generating spin polarization (or surface spin current) when passing a lateral charge current through the surface, which is significant for potential spintronic applications.

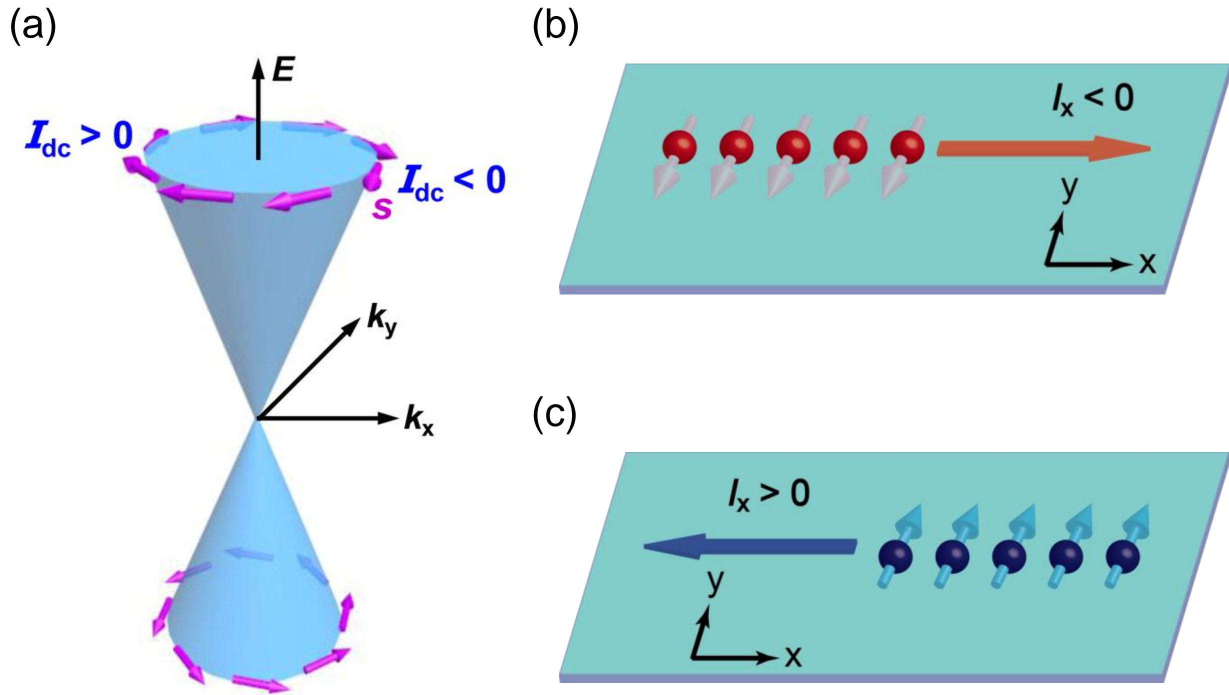

Figure 1-6. Charge current-induced surface spin polarization in TI. (a) Schematic illustration of the helical spin texture of the surface states in TI: clockwise spin texture above the Dirac point while anti-clockwise spin texture below the Dirac point. Figure is adapted with permission from ref. [91] (Y. Fan's publication). (b) Schematic of surface spin polarization for a charge current flowing along –*x* direction (*i.e.*, $I_x < 0$). (c) Schematic of surface spin polarization for a charge current flowing along *x* direction (*i.e.*, $I_x > 0$).

In experiment, in order to detect the surface states spin-momentum locking (*i.e.*, the charge current-induced surface spin polarization) by electrical transport method, a magnet electrode/oxide structure was placed on top of TI to form a ferromagnetic tunneling contact [91], as illustrated in Fig. 1-7(a). In this structure, the magnet electrode is a cobalt (Co) strip with a transverse in-plane easy axis and the oxide layer is Al_2O_3. By passing a longitudinal dc current through the TI film, a steady spin polarization is formed on the surface. If the polarized surface

Dirac electrons' spin magnetic moment is parallel with the Co electrode magnetization direction, a low-(magneto)-resistance state (LRS) between the Co electrode and the TI film is measured; accordingly, when the surface Dirac electrons' spin magnetic moment is antiparallel with the Co magnetization direction, a high-(magneto)-resistance state (HRS) is produced, similar to the giant magneto-resistance (GMR) effect [92,93] observed in the Fe/Cr/Fe trilayer system. The above scenario was successfully demonstrated by switching the Co electrode magnetization direction or changing the longitudinal dc current direction and meanwhile measuring the magnetoresistance (MR) between the Co electrode and the TI layer, as plotted in Fig. 1-7 (c-d). The measured spin polarization of the surface current is consistent with the helical spin texture of the surface states as shown in Fig. 1-7 (b), which is also in agreement with previous spin-resolved ARPES experiments [82,85]. Besides this work [91], there are several other reports [94-98] on similar electrical detection of spin polarization of the surface states conduction in TIs.

The surface charge current-induced spin polarization on TI is robust in the sense that it is protected by the bulk topology in the momentum space. This induced spin polarization can potentially apply very efficient SOT on an adjacent magnetic layer and result in various magnetic dynamics and effects. Compared with the traditional HMFHs [27,38,41,42], where the SOT is generated through the SHE in heavy metals, TIs' surface states spin-momentum locking offers a new and potentially more efficient mechanism to generate SOT. Given the feasibility of combining TIs with various magnetic materials by molecular beam epitaxy (MBE) growth, TI-based magnetic structures may lead to the new generation of spintronic memory and logic devices with far greater energy efficiency and much better performance.

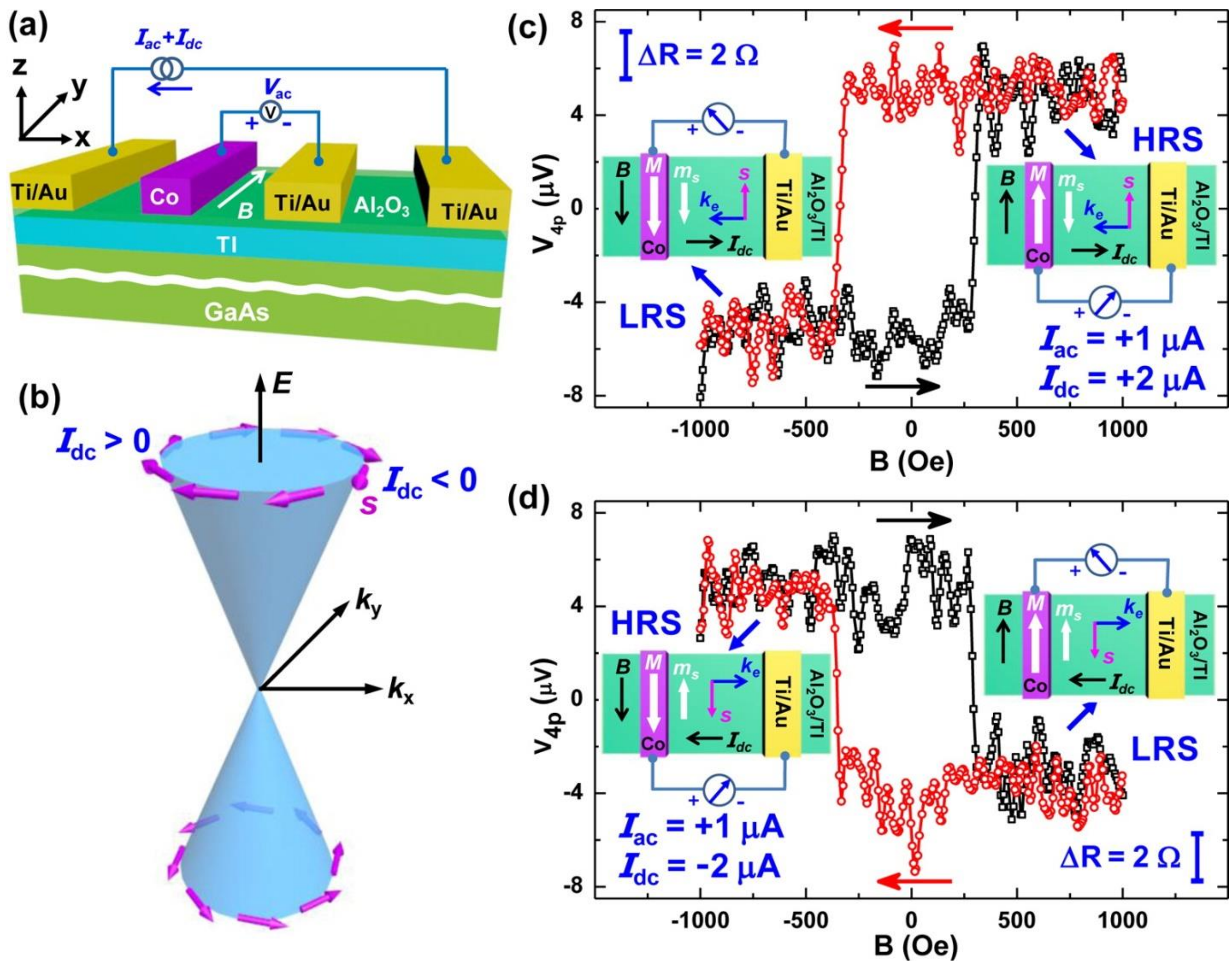

Figure 1-7. Electrical detection of the spin-polarized surface states conduction in $(Bi_{0.53}Sb_{0.47})_2Te_3$. (a) Schematic illustration of the device structure with one ferromagnetic tunneling Co/Al_2O_3 contact for spin detection. The measurement setup with a 4-probe configuration and a lock-in technique is also illustrated. (b) Schematic illustration of the helical spin texture of the surface states in TI: clockwise spin texture above the Dirac point while anti-clockwise spin texture below the Dirac point. (c-d) The measured voltage (resistance) at T=1.9 K as the in-plane magnetic field is swept back and forth under dc bias of I_{dc}= +2 μA and I_{dc}= -2 μA, respectively. The parabolic background MR was subtracted. The scale bar represents a corresponding resistance of 2 Ω. The red and black arrows indicate the magnetic field sweeping

direction. The insets show the high-resistance state (HRS) and low-resistance state (LRS), determined by the relative orientation between the Co electrode magnetization M and the spin polarization s of surface states. The electron spin s is anti-parallel to its magnetic moment m_s because of the negative charge of electron. Figures are adapted with permission from ref. [91] (Y. Fan's publication).

1.3 Motivation for Exploring Spin-Orbit Torques in Topological Insulator-based Magnetic Structures

The motivation is multifold. Firstly, as we discussed above, TIs' surface states spin-momentum locking feature can probably provide a much more efficient way [57-59,99] to generate SOT than other mechanisms such as the SHE in heavy metals. The intuitive reason is that the surface charge current-induced spin polarization in TIs is protected by the bulk topology, which is very robust and immune to nonmagnetic impurity scatterings [54,100,101]. As a result, it is highly worthwhile studying the SOT-related physics in the TI-based magnetic structures, which has both fundamental importance and potential technological applications in spintronics.

Secondly, compared with heavy metals, the bulk of TI materials can be made very insulating by optimizing the material growth technique [102,103]. This is advantageous because when passing a charge current through the TI material with an insulating bulk, most of the current will flow on the surface and participate in the spin polarization or SOT generation as the transport is governed by the surface states Dirac Hamiltonian [54,55]. In contrast, the transport in heavy metals is usually dominated by the bulk kinetic Hamiltonian which accounts for a major portion of the total Hamiltonian [27], and the SOC interaction is incorporated in as a perturbation

part. In the TIs' surface Dirac Hamiltonian, on the contrary, the SOC interaction accounts for the entire Hamiltonian which couples spins with momentum rigorously [70,76,82]. This feature distinguishes TIs from heavy metals. The above argument provides another perspective to suggest that TIs are much more efficient materials in generating SOT than heavy metals.

Thirdly, 3D TIs (Bi_2Se_3, Bi_2Te_3, Sb_2Te_3, *etc*.) are van der Waals materials. This property makes them suitable for growing on quite a large range of different substrates, including the magnetic substrates. Indeed, the TI/ferromagnet (*e.g*., CoFeB, NiFe, *etc*.) [59,60], TI/magnetic insulator (*e.g*., YIG, EuS, *etc*.) [104-106] structures have been successfully prepared by different groups. Besides, when TIs are doped with magnetic elements (Cr, V, *etc*.) [107-114], pronounced ferromagnetic order can be formed in the materials with the surface massless Dirac fermions driven to massive ones [80,115]. This opens up many new opportunities for constructing TI/magnetic TI heterostructures or superlattices by MBE *in situ* growth, which provides the ideal platform for studying SOT-related physics in TI-based magnetic structures. Based on the above motivations, we have carried out the SOT research in the TI-based magnetic structures (more specifically the magnetically doped TI structures [57,58]), which we will describe in detail in this dissertation.

1.4 Dissertation Outline

In this dissertation, we will present two closely-related projects on SOT study in TI-based magnetic structures. In Chapter 2, we will first present the magnetization switching through giant SOT in a TI/Cr-doped TI bilayer heterostructure. Both the effective spin-orbit field to current ratio and the spin-torque ratio are found to be three orders of magnitude larger than those reported for conventional HMFHs. Then in Chapter 3, we will show the effective electric-field control of the giant SOT in a uniformly Cr-doped TI thin film by using a top-gate field-effect transistor (FET) structure. We demonstrate that the SOT strength can be modulated by a factor of 4 within the accessible gate voltage range, which provides strong evidence of topological surface states-related spin-torque physics. We furthermore demonstrate the magnetization switching by scanning gate voltage with constant current and in-plane magnetic field applied in the Cr-doped TI thin film. Finally, a brief discussion and conclusion will be given in Chapter 4, followed by an outlook of future research work.

Chapter 2

Magnetization Switching through Giant Spin-Orbit Torque in a Magnetically Doped Topological Insulator Heterostructure

2.1 Overview

Since TIs are very promising materials for generating giant SOT and enabling efficient manipulation of magnetization, they have attracted enormous research interest during the past few years for potential applications in ultralow power spintronic devices. As summarized in Fig. 2-1, there have been various research topics in the field of topological spintronics based on TIs, including SOT-induced magnetization switching [57,58], electric-field control of SOT [58], spin torque-ferromagnetic resonance (ST-FMR) measurement [59,60] as well as spin pumping and inverse spin Hall effect (ISHE) [61-65] in TI/ferromagnet structures, electrical detection of surface spin-polarized current flowing in TIs [91,94-98], and spin-polarized tunneling spectroscopy study of the TI surface states [66].

Among all these research topics, the SOT-induced magnetization switching in TI-based magnetic structures provides the direct evidence of current-induced giant SOT and suggests tantalizing applications for energy-efficient magnetic memory devices. Switching of a magnet using the least possible energy in a scalable structure is one of the most-pursued goals in spintronic memory devices. Starting from the theoretical prediction of STT [10-12] and the experimental demonstration of STT-induced magnetization switching in a Co/Cu/Co sandwich structure [15,16], people have put enormous effort in optimizing the STT device structure (*e.g.*, by developing MTJ structures using MgO as the tunneling barrier [21-23]) and searching for more

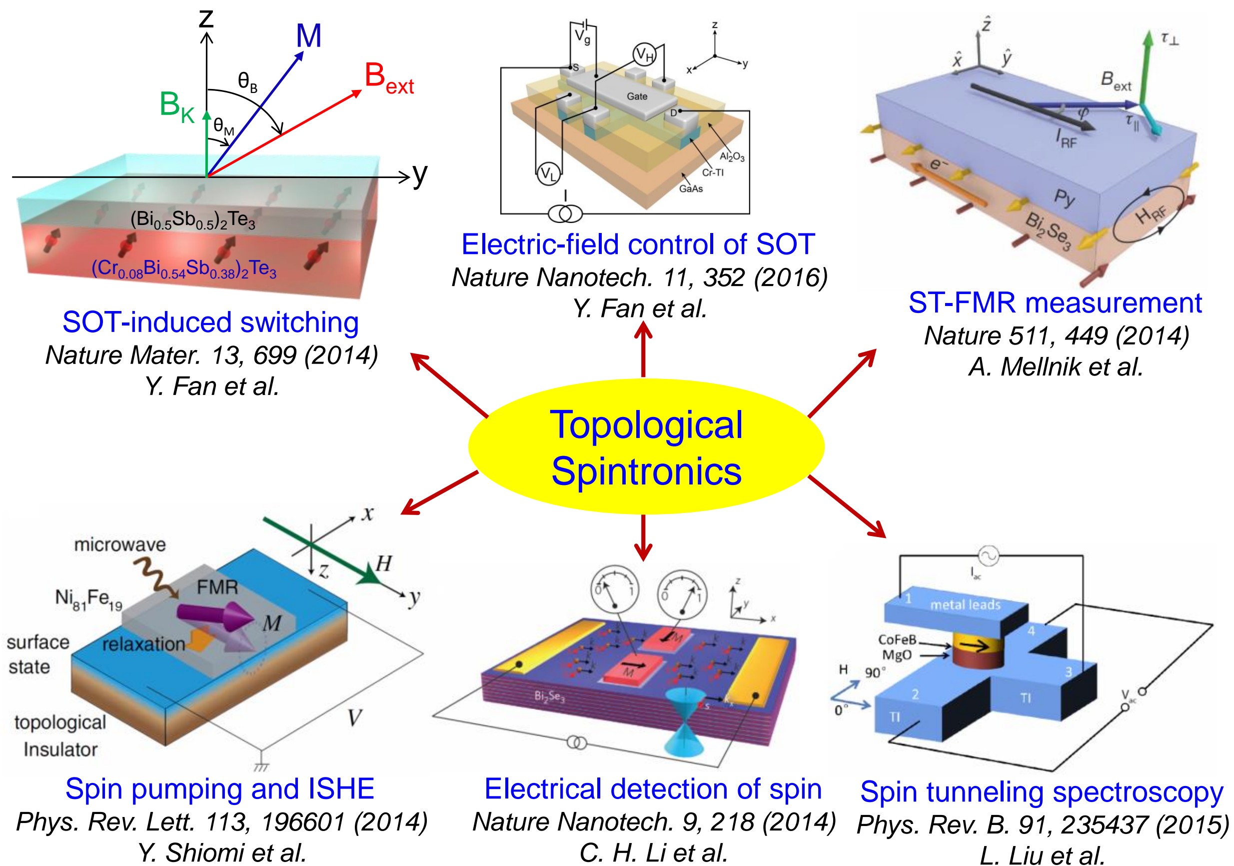

Figure 2-1. Various research topics in TI-based topological spintronics, including SOT-induced magnetization switching, electric-field control of SOT, ST-FMR measurement of spin-torque, spin pumping and ISHE, electrical detection of surface spin-polarized current, and spin tunneling spectroscopy study of TI.

efficient materials for generating the spin-polarized current. Most recently, heavy metals (*e.g.*, Pt) with strong SOC have become such materials under extensive study due to their ability to generate efficient spin current when passing an in-plane charge current through them [9,38,41,42,44,45,51,52,116-119]. Different from the traditional STT-based MTJ structures where the incident current is polarized by the fixed layer, the spin currents generated by heavy metals are

arising from either the SHE [38,42,45,120,121] in the bulk or the Rashba-type effect at the interfaces [26,41,51,118,119,121-126]. The heavy metal-generated spin current can apply efficient spin torques to the adjacent ferromagnet layer (*e.g.*, Co, CoFeB), and result in SOT-induced manipulation of magnetization [44,45,51,52,117-119] and even switching [38,41,42]. Although the underlying mechanisms of the SOTs are still being debated [9,42,121], the ability to manipulate magnetic moments with lateral current has shown promising applications in miniaturized magnetic memory and logic devices, and more appropriate material/structure to generate these SOTs awaits further investigation.

Then it comes to TIs [54-56]. TIs are such materials that the SOC is large enough to invert the band structure in the bulk [69], and consequently they are expected to be the most promising candidate to exploit the SOTs when coupled to magnetic moments [127-129]. In addition, the recently demonstrated magnetism in magnetically doped TIs (*e.g.*, Cr-doped TIs) [80,107,109,112,115,130,131] makes it accessible to study the SOTs in the TI/magnetic-TI bilayer heterostructures [109,132], which we will describe in detail in this chapter. In a pedagogical manner, we will first illustrate the material properties of the TI/Cr-doped TI bilayer heterostructure. After that, we will provide the experimental demonstration of magnetization switching through giant SOT in this bilayer heterostructure and then calibrate the strength of SOT by low-frequency second harmonic analysis [9,116]. Most importantly, we find that the critical current density required for switching is below 8.9×10^4 A/cm^2 at low temperature and the effective spin-orbit field to current ratio, as well as the spin-torque ratio, is nearly three orders of magnitude larger than those reported in HMFHs. Thirdly, we will analyze the thermal effect and the temperature dependence of the SOT in this bilayer heterostructure. Finally, we will examine the multi-domain switching process (through simulation) and the anisotropic magneto-resistance (AMR) and planar Hall effect (PHE) in this bilayer heterostructure and their influence on the SOT.

2.2 Topological Insulator/Cr-doped Topological Insulator Bilayer Heterostructure Magnetic Properties

Epitaxial $(Bi_{0.5}Sb_{0.5})_2Te_3/(Cr_{0.08}Bi_{0.54}Sb_{0.38})_2Te_3$ bilayer films are first grown on an insulating GaAs (111)B substrate using the modulation-doped molecular beam epitaxy (MBE) growth method [109]. The thin film growth was performed using an ultra-high vacuum Perkin Elmer MBE system. Semi-insulating ($\rho > 10^6$ Ω·cm) GaAs (111)B substrates were pre-annealed in the growth chamber at up to 580 °C to remove the native oxide. High-purity Bi (99.9999%), Te (99.9999%), Cr (99.99%) and Sb (99.999%) were evaporated by conventional effusion cells and cracker cells. During the modulation-doped growth, the GaAs (111)B substrate was maintained at 200˚C (growth temperature). Bi and Te cells were kept at 470˚C and 320˚C, respectively, whereas the Sb and Cr temperatures were varied to adjust the carrier densities and the magnetic impurity doping profiles in different layers. Epitaxial growth was monitored by an *in-situ* reflection high-energy electron diffraction (RHEED) technique, and the surface was found to be atomically flat as evidenced by streaky RHEED patterns. Digital images of the RHEED were captured using a KSA400 system built by K-space Associates, Inc.† (†: company)

For the bilayer heterostructure, the top $(Bi_{0.5}Sb_{0.5})_2Te_3$ layer thickness is chosen to be 3 quintuple layers (QLs) while the bottom $(Cr_{0.08}Bi_{0.54}Sb_{0.38})_2Te_3$ layer is 6 QLs, with atomically sharp hetero-interface in between as indicated by the high-resolution scanning transmission electron microscopy (HRSTEM). The HRSTEM experiments were performed on a FEI† TITAN Cs-corrected scanning transmission electron microscope operating at 200 KV and the high angle annular dark field (HAADF) images were acquired using a Fischione† HAADF detector. For example, Fig. 2-2a shows the HRSTEM image on one of the bilayer films we have grown with composition $(Bi_{0.5}Sb_{0.5})_2Te_3/(Cr_{0.04}Bi_{0.57}Sb_{0.39})_2Te_3$, which reveals the atomically sharp TI/Cr-

doped TI – GaAs (111)B interface and highly-ordered tetradymite-type QL structure. Such epitaxially-ordered lattice configuration also confirms that there is no second phase segregation inside the TI/Cr-doped TI bilayer thin film within the resolution of HRSTEM. In addition, the Bi/Sb composition ratio as well as the Cr-doping level is determined by an energy-dispersive X-ray (EDX) spectroscopy as shown in Fig. 2-2b. While the top TI layer shows no obvious Cr peak in the EDX spectrum, there is a clear Cr peak in the bottom Cr-doped TI layer EDX spectrum, indicating that the top TI layer is free of magnetic impurities and the diffusion of Cr dopants from the bottom Cr-doped TI layer into the top TI layer is negligible. (†: companies)

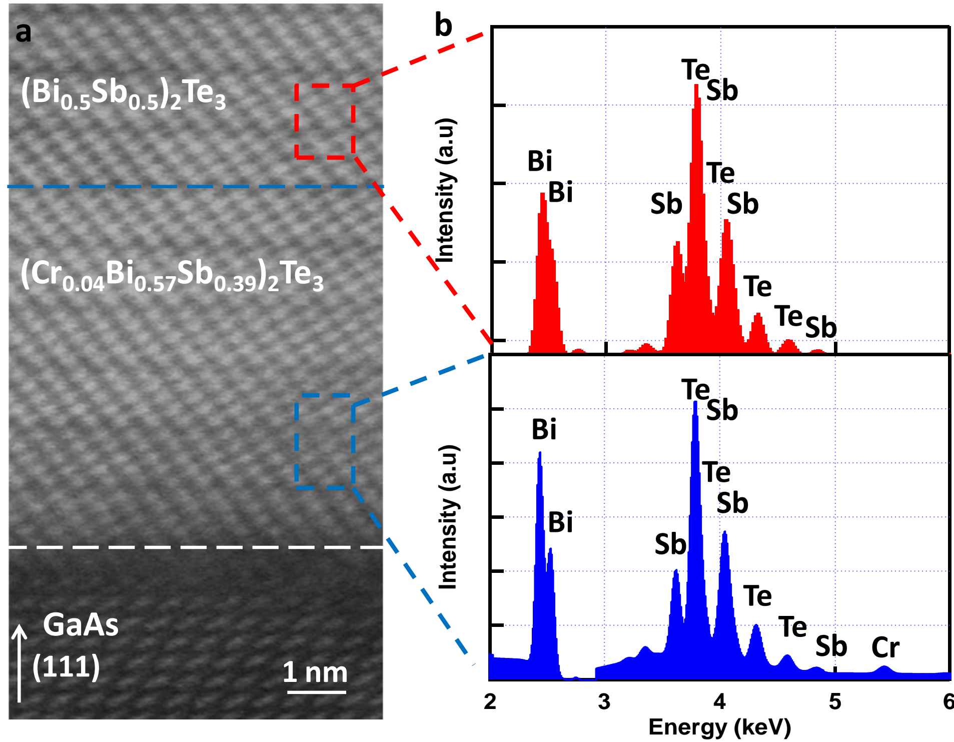

Figure 2-2. HRSTEM and EDX spectrum of the $(Bi_{0.5}Sb_{0.5})_2Te_3/(Cr_{0.04}Bi_{0.57}Sb_{0.39})_2Te_3$ bilayer thin film. **a,** High-resolution cross-section HRSTEM image of the bilayer thin film. Typical quintuple-layered crystalline structure and sharp TI-GaAs interface can be clearly observed. No Cr segregations are detected, which indicates a uniform Cr dopant distribution in the magnetic TI

layer matrix. **b**, EDX spectrum of the $(Bi_{0.5}Sb_{0.5})_2Te_3$ and $(Cr_{0.04}Bi_{0.57}Sb_{0.39})_2Te_3$ layers. Figure is adapted with permission from ref. [109] (Y. Fan's publication).

In the $(Bi_{0.5}Sb_{0.5})_2Te_3/(Cr_{0.08}Bi_{0.54}Sb_{0.38})_2Te_3$ bilayer heterostructure where we studied the SOT, the Bi/Sb ratio is adjusted to 0.5/0.5 in the top $(Bi_{0.5}Sb_{0.5})_2Te_3$ layer and 0.59/0.41 in the bottom $(Cr_{0.08}Bi_{0.54}Sb_{0.38})_2Te_3$ layer so that both layers display similar conductivities (222.7 S/cm and 219.5 S/cm, respectively), which guarantees a uniform current distribution inside the entire structure (we will discuss the impedance-match in more detail later) [109]. Pronounced ferromagnetism has been reported in the $(Cr_xBi_ySb_{1-x-y})_2Te_3$ films [108,109], and with an appropriate doping concentration, the quantum anomalous Hall phase [110-112,114,133] can also be obtained. To investigate the SOTs in our TI/Cr-doped TI bilayer heterostructure, micrometer-size Hall bar devices [134] were prepared, as shown in Fig. 2-3b. The modulation-doped $(Bi_{0.5}Sb_{0.5})_2Te_3/(Cr_{0.08}Bi_{0.54}Sb_{0.38})_2Te_3$ bilayer thin film was patterned into micron-scale Hall bar geometries using conventional optical photolithography with subsequent CHF_3 dry etching for 18s. A 20 nm thick high-k Al_2O_3 dielectric layer was deposited by atomic layer deposition (ALD) at 250°C. The Hall channel contacts were defined by e-beam evaporation after the Al_2O_3 was etched away in the contact areas. A metal stack of Ti/Al (20 nm/100 nm) was directly deposited onto the exposed TI top surface to form the contacts. In this Hall bar geometry, as shown in Fig. 2-3a, when applying a large enough external magnetic field $\mathbf{B_{ext}}$ in the yz-plane, the magnetization $\mathbf{M}$ becomes polarized, and the relative positions between $\mathbf{B_{ext}}$ and $\mathbf{M}$ are also illustrated in Fig. 2-3a, where θ_B and θ_M are the polar angles of $\mathbf{B_{ext}}$ and $\mathbf{M}$ from the z-axis, respectively. Here, $\mathbf{B_K} = K\cos\theta_M\hat{\mathbf{z}}$ is the out-of-plane anisotropy field with K the anisotropy coefficient estimated to be around 0.9T (see Section 2.4).

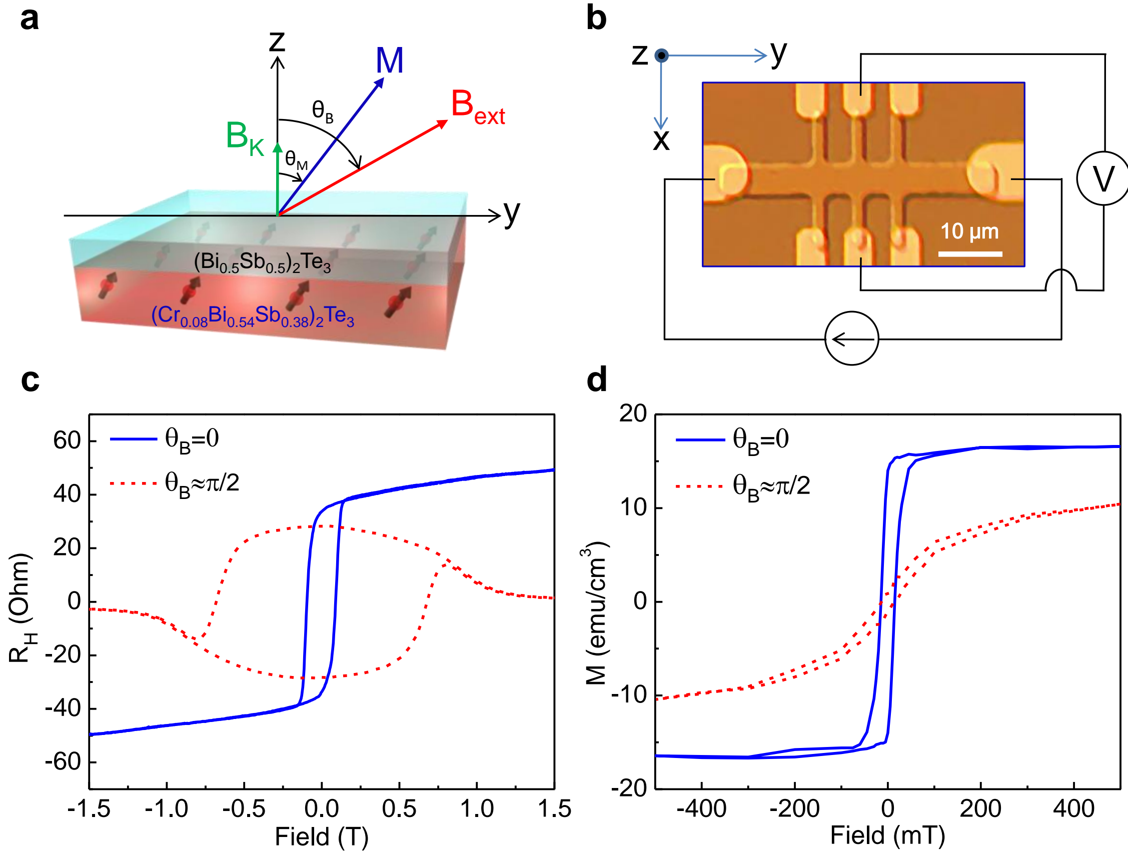

Figure 2-3. Experimental setup and magnetic properties of the $(Bi_{0.5}Sb_{0.5})_2Te_3$ /$(Cr_{0.08}Bi_{0.54}Sb_{0.38})_2Te_3$ bilayer heterostructure. **a,** Three-dimensional schematic of the bilayer heterostructure. The top layer (light blue) shows the 3QLs $(Bi_{0.5}Sb_{0.5})_2Te_3$ and the bottom layer (light red) presents the 6QLs $(Cr_{0.08}Bi_{0.54}Sb_{0.38})_2Te_3$. $\mathbf{B_{ext}}$ (red arrow) represents the external magnetic field and **M** (blue arrow) denotes the magnetization of the bottom $(Cr_{0.08}Bi_{0.54}Sb_{0.38})_2Te_3$ layer. $\mathbf{B_K}$ (green arrow) is the out-of-plane anisotropy field. **b,** Micro-graph of the Hall bar device with schematic illustrations of the Hall measurement set-up. The width of the Hall bar and the length between two neighboring Hall contacts are both 5 μm. **c,** The Hall resistance as a function of the applied external magnetic field for both the out-of-plane ($\theta_B = 0$) and nearly in-plane ($\theta_B \approx \pi/2$) directions, respectively, at 1.9K. **d,** SQUID

measurement of the magnetization for both the out-of-plane ($\theta_{\mathrm{B}} = 0$) and in-plane ($\theta_{\mathrm{B}} \approx \pi/2$) directions, respectively, at 5K for external magnetic fields up to ±500mT. Figure is adapted with permission from ref. [57] (Y. Fan's publication).

In order to examine the magnetic properties of the bilayer heterostructure, four-point Hall measurements were conducted using the Quantum Design Physical Property Measurement System (PPMS). We were able to systematically alter several experimental variables such as temperature, magnetic field and measurement frequency. Multiple lock-in amplifiers and Keithley source meters were connected with the PPMS system, enabling comprehensive and high-sensitivity transport measurements for the Hall bar devices. Field-dependent Hall resistance measurements of the TI/Cr-doped TI bilayer heterostructure for both the out-of-plane ($\theta_{\mathrm{B}} = 0$) and nearly in-plane ($\theta_{\mathrm{B}} \approx \pi/2$) directions were carried out at 1.9 K, and the results are displayed in Fig. 2-3c. The nearly square-shape magnetic hysteresis loop of R_{H} at $\theta_{\mathrm{B}} = 0$ clearly suggests that the magnetization easy axis is out-of-plane (*i.e.*, along the z-direction). In addition, superconducting quantum interference device (SQUID) measurements were carried out to directly probe the magnetization $\mathbf{M}$ for both the out-of-plane ($\theta_{\mathrm{B}} = 0$) and in-plane ($\theta_{\mathrm{B}} \approx \pi/2$) directions, and the results are shown in Fig. 2-3d. The saturation magnetization M_{S} is measured to be around 16 emu/cm^3 along the out-of-plane ($\theta_{\mathrm{B}} = 0$) direction for applied magnetic fields greater than 100 mT. In contrast, $\mathbf{M}$ does not show any saturation behavior even when $|\mathbf{B}_{\mathbf{ext}}| > 500$ mT for fields along the in-plane ($\theta_{\mathrm{B}} \approx \pi/2$) direction, again indicating the robust out-of-plane magnetic anisotropy of our TI/Cr-doped TI heterostructure sample.

As we have mentioned before, next, we will demonstrate the impedance-match for the top $(Bi_{0.5}Sb_{0.5})_2Te_3$ layer and the bottom $(Cr_{0.08}Bi_{0.54}Sb_{0.38})_2Te_3$ layer in the $(Bi_{0.5}Sb_{0.5})_2Te_3$

/$(Cr_{0.08}Bi_{0.54}Sb_{0.38})_2Te_3$ bilayer heterostructure thin film. The essential requirement for our magnetization switching experiments in the following section is to generate a uniform lateral current distribution inside the bilayer thin film. As we show the bilayer-based Hall bar device structure in Fig. 2-3b, the electric current is applied laterally from the source contact (S) to the drain contact (D) during the transport measurements. This in turn results in the parallel conduction configuration between the top undoped TI layer and the bottom Cr-doped TI layer. Consequently, we have to match the conductivities (S/m) between these two channels in order to make sure we have a uniform current density (A/m^2) flowing from S to D inside the whole bilayer film. By taking this concern into consideration, we deliberately adjust the Bi/Sb ratio in both the TI layer and the Cr-doped TI layer during the modulation growth so that the conductivities of them are nearly the same. The requirement is finally achieved in the $(Bi_{0.5}Sb_{0.5})_2Te_3$/$(Cr_{0.08}Bi_{0.54}Sb_{0.38})_2Te_3$ configuration where the conductivities in these two layers are almost the same at 1.9 K. To demonstrate the impedance-match for these two layers, we separately grow a 6QL $(Bi_{0.5}Sb_{0.5})_2Te_3$ thin film and a 6QL $(Cr_{0.08}Bi_{0.54}Sb_{0.38})_2Te_3$ thin film, and the magneto-transport experiments are carried out to probe their magneto-conductivities. In Fig. 2-4, we show the obtained data which demonstrate that the two films have nearly the same magneto-conductivities within a certain magnetic field region. Besides, the measured 2D carrier densities of these two films, as shown in Table 2-1, are low enough to ensure the Fermi level is inside the bulk band gap [108], as comparable with other reported data [102,135,136]. The related electric properties of these two different films are summarized in Table 2-1.

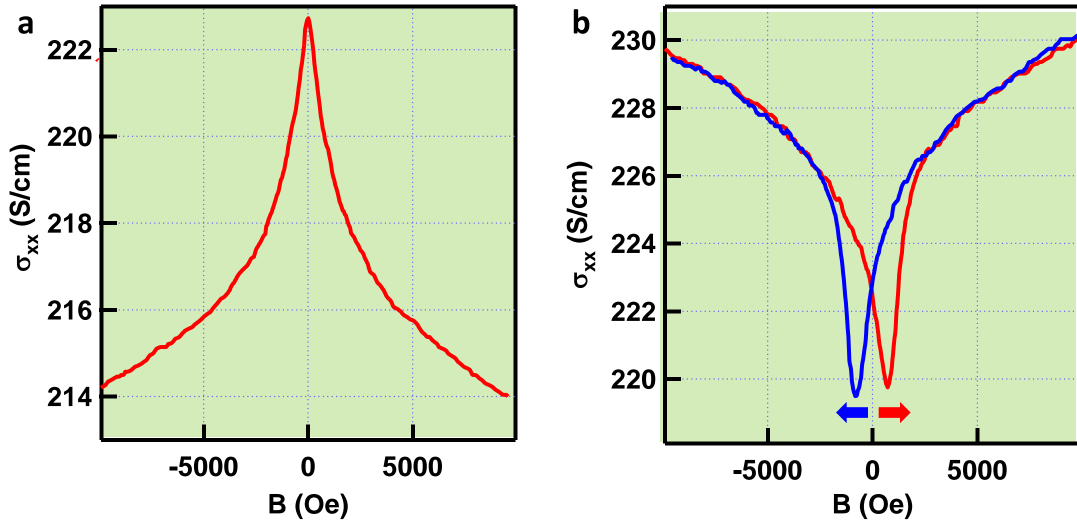

Figure 2-4. Magneto-conductivity data showing similar conductivities for the **(a)** 6 QL $(Bi_{0.5}Sb_{0.5})_2Te_3$ and **(b)** 6 QL $(Cr_{0.08}Bi_{0.54}Sb_{0.38})_2Te_3$ thin films on GaAs (111)B substrate at 1.9 K. The external magnetic field is applied perpendicularly to the samples, and the arrows indicate the sweeping directions of the field. Figure is adapted with permission from ref.[109] (Y. Fan's publication).

Table 2-1. Electric properties of both the 6QL TI and the 6QL Cr-doped TI thin films at 1.9 K

Sample	**σ_{xx} (0 T) (S/cm)**	**R_{sheet} (0 T) (kΩ□$^{-1}$)**	**n_{2D} (×10^{12} cm^{-2})**	**μ (cm^2/V·s)**
$(Bi_{0.5}Sb_{0.5})_2Te_3$	222.7	14.96	0.9	370
$(Cr_{0.08}Bi_{0.54}Sb_{0.38})_2Te_3$	219.5	15.16	5.1	50.8

Table is adapted with permission from ref.[109] (Y. Fan's publication).

2.3 Magnetization Switching through Giant SOT in the Bilayer Heterostructure

In the conductive TI/Cr-doped TI bilayer heterostructure, when passing a charge current in the y-direction, due to the spin-momentum locking of the topological surface states [54,55,82,90,127], a dominant spin accumulation in the Cr-doped TI layer with spin polarized in the x-direction is expected, as shown in Fig. 2-5. There is also possible contribution to the surface spin accumulation in the Cr-doped TI layer arising from the SHE in the bulk and the Rashba-type interactions at the interfaces. The accumulated spins' angular momentum can be transferred to the Cr dopants magnetization $\mathbf{M}$ and therefore apply SOTs to control its dynamics. Based on the symmetry argument [9] and the bilayer heterostructure Hall bar geometry, the accumulated spins can give rise to two types of SOTs, the antidamping-like SOT $\boldsymbol{\tau}_{\mathbf{SO}}$ and the field-like SOT $\boldsymbol{\tau}_{\mathbf{F}}$, as illustrated in Fig. 2-5. To the leading orders, they can be written in the following forms in the extended Landau-Lifshitz-Gilbert (LLG) equation,

$$\frac{\partial \mathbf{M}}{\partial t} = -\gamma \mathbf{M} \times \mathbf{B}_{\mathbf{eff}} + \frac{\alpha}{M_{\mathrm{S}}} \mathbf{M} \times \frac{\partial \mathbf{M}}{\partial t} - \gamma I \lambda_{\mathrm{SO}} \mathbf{M} \times (\hat{\boldsymbol{x}} \times \mathbf{m}) - \gamma I \lambda_{\mathrm{F}} \mathbf{M} \times \hat{\boldsymbol{x}} \qquad (2-1)$$

Here, $\mathbf{B}_{\mathbf{eff}}$ stands for the sum of the external magnetic field $\mathbf{B}_{\mathbf{ext}}$ and the anisotropy field $\mathbf{B}_{\mathbf{K}}$; $\boldsymbol{\tau}_{\mathbf{SO}} = -\gamma I \lambda_{\mathrm{SO}} \mathbf{M} \times (\hat{\boldsymbol{x}} \times \mathbf{m})$ and $\boldsymbol{\tau}_{\mathbf{F}} = -\gamma I \lambda_{\mathrm{F}} \mathbf{M} \times \hat{\boldsymbol{x}}$ are the two-type SOTs; γ is the gyromagnetic ratio, α is the damping constant, λ_{SO} and λ_{F} are the coefficients characterizing the SOC strength in the system, I is the charge current conducting along the longitudinal direction and $\mathbf{m}$ is the unit vector denotes the magnetization direction. For convenience in analyzing the results, the two SOTs can be further formulated as, $\boldsymbol{\tau}_{\mathbf{SO}} = -\gamma \mathbf{M} \times \mathbf{B}_{\mathbf{SO}}$ and $\boldsymbol{\tau}_{\mathbf{F}} = -\gamma \mathbf{M} \times \mathbf{B}_{\mathbf{F}}$, where $\mathbf{B}_{\mathbf{SO}} = I \lambda_{\mathrm{SO}} \hat{\boldsymbol{x}} \times \mathbf{m}$ and $\mathbf{B}_{\mathbf{F}} = I \lambda_{\mathrm{F}} \hat{\boldsymbol{x}}$ are the effective spin-orbit fields corresponding to these two SOTs, as displayed in Fig. 2-5. We found that the field-like SOT is an order of magnitude

smaller than the antidamping-like SOT in our structure (see Sections 2.4 and 2.6). As a result, we will focus mainly on analyzing the antidamping-like SOT in the following.

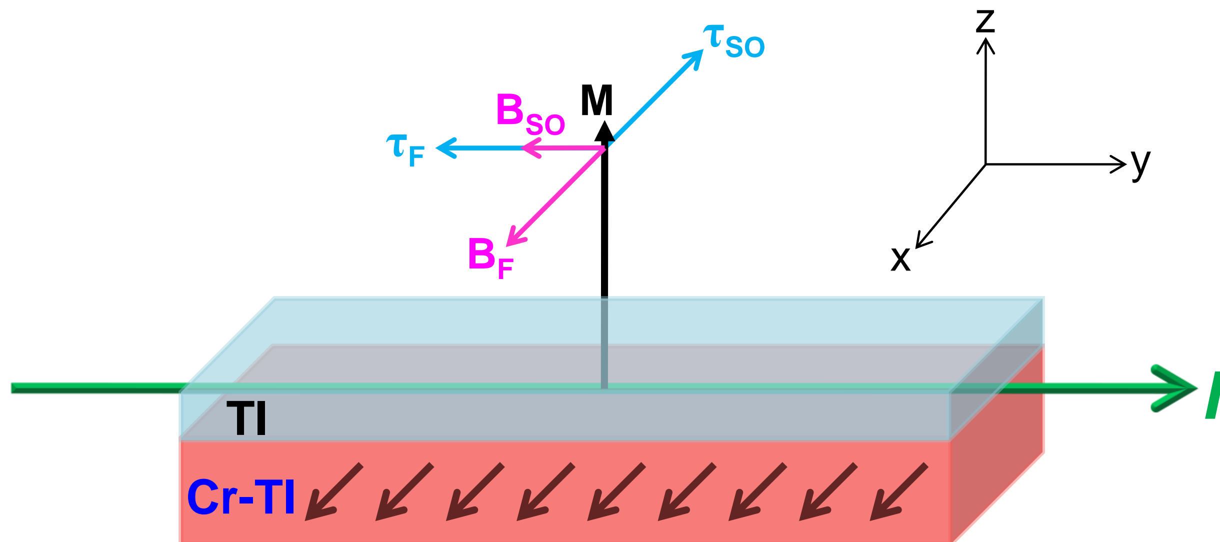

Figure 2-5. Illustration of the spin accumulation (denoted by dark gray arrows) in the Cr-doped TI layer and the resulted SOTs, namely the antidamping-like SOT $\boldsymbol{\tau}_{\mathbf{SO}}$ and the field-like SOT $\boldsymbol{\tau}_{\mathbf{F}}$, as well as the corresponding effective spin-orbit fields ($\mathbf{B}_{\mathbf{SO}}$ and $\mathbf{B}_{\mathbf{F}}$) when passing a lateral charge current *I* through the TI/Cr-doped TI bilayer heterostructure thin film.

Now we analyze the mechanism of the SOT-induced magnetization switching in the bilayer heterostructure. First, we illustrate the four stable states in Fig. 2-6a where the applied DC current, I_{dc}, conducts along the longitudinal direction (*i.e.*, $\pm y$-axis), and the external magnetic field is also applied along the $\pm y$-axis. In panel 1 of Fig. 2-6a, for example, we show the case where the DC current, I_{dc}, and the in-plane external magnetic field, $\mathbf{B}_{\boldsymbol{y}}$, are both applied along the $+y$-axis. The effective spin-orbit field, $\mathbf{B}_{\mathbf{SO}}$, induced by I_{dc} is pointing along the tangential $-\hat{\boldsymbol{\theta}}$ direction of $\mathbf{M}$, which tilts $\mathbf{M}$ up to obtain a positive z-component, M_z, when in equilibrium. The other three cases for different configurations of the applied I_{dc} and $\mathbf{B}_{\boldsymbol{y}}$ are illustrated in

panels 2-4 of Fig. 2-6a, correspondingly. To summarize, in the presence of a constant external magnetic field in the y-direction, the z-component magnetization M_z can be switched, depending on the DC current conduction direction [38,41,42]; likewise, when the applied DC current is fixed, M_z can also be switched by changing the in-plane external magnetic field.

Based on such a scenario, we carried out the (I_{dc}-fixed, $\mathbf{B}_y$-dependent) and the ($\mathbf{B}_y$-fixed, I_{dc}-dependent) experiments at 1.9K; the results are shown in Fig. 2-6b and 2-6c, respectively. Specifically, when $I_{\mathrm{dc}} = +10\mu$A (blue squares in Fig. 2-6b), the anomalous Hall effect (AHE) resistance R_{AHE} goes from negative to positive as the applied in-plane magnetic field $\mathbf{B}_y$ gradually changes from -3T to 3T, indicating the z-component magnetization M_z switches from $-z$ to $+z$. In contrast, when $I_{\mathrm{dc}} = -10\mu$A, the AHE resistance reverses sign (red circles in Fig. 2-6b) and M_z varies from $+z$ to $-z$ as $\mathbf{B}_y$ is swept from -3T to 3T. It should be noted that in both cases the AHE resistance hysteresis loops agree well with our proposed scenario. At the same time, when we scan the DC current I_{dc} at a given fixed magnetic field, we also observe similar magnetization switching behavior: the AHE resistance R_{AHE} changes from negative to positive for $B_y = +0.6$T (blue squares in Fig. 2-6c), but reverses its evolution trend, *i.e.*, changes from positive to negative, for $B_y = -0.6$T (red circles in Fig. 2-6c). For this case, the small hysteresis window in R_{AHE} is clearly visible on expanded scale as shown in the inset of Fig. 2-6c. Consequently, both the (I_{dc}-fixed, $\mathbf{B}_y$-driven) and the ($\mathbf{B}_y$-fixed, I_{dc}-driven) magnetization switching behaviors clearly demonstrate that the magnetization can be effectively manipulated by the current-induced SOT in our TI/Cr-doped TI bilayer heterostructure. We summarize these switching behaviors in the phase diagram in Fig. 2-6d. For the four corner panels in Fig. 2-6d where the field value B_y and I_{dc} are large, the magnetization state is

deterministic; however, in the central panel where B_y and I_{dc} are small, both magnetization states, up and down, are possible; this behavior agrees with the hysteresis windows, as shown in Fig. 2-6b and 2-6c, where in the low B_y and small I_{dc} region the two magnetization states are both allowed. Based on this phase diagram, it can be clearly seen that the magnetization can be easily switched with only tens of μA DC current (*i.e.*, below 8.9×10^4 A/cm^2 in current density J_{dc}), suggesting that the current-induced SOT in our TI/Cr-doped TI bilayer heterostructure is quite efficient. The temperature dependence of the critical switching current density and the anisotropy field can be found in Section 2.5.

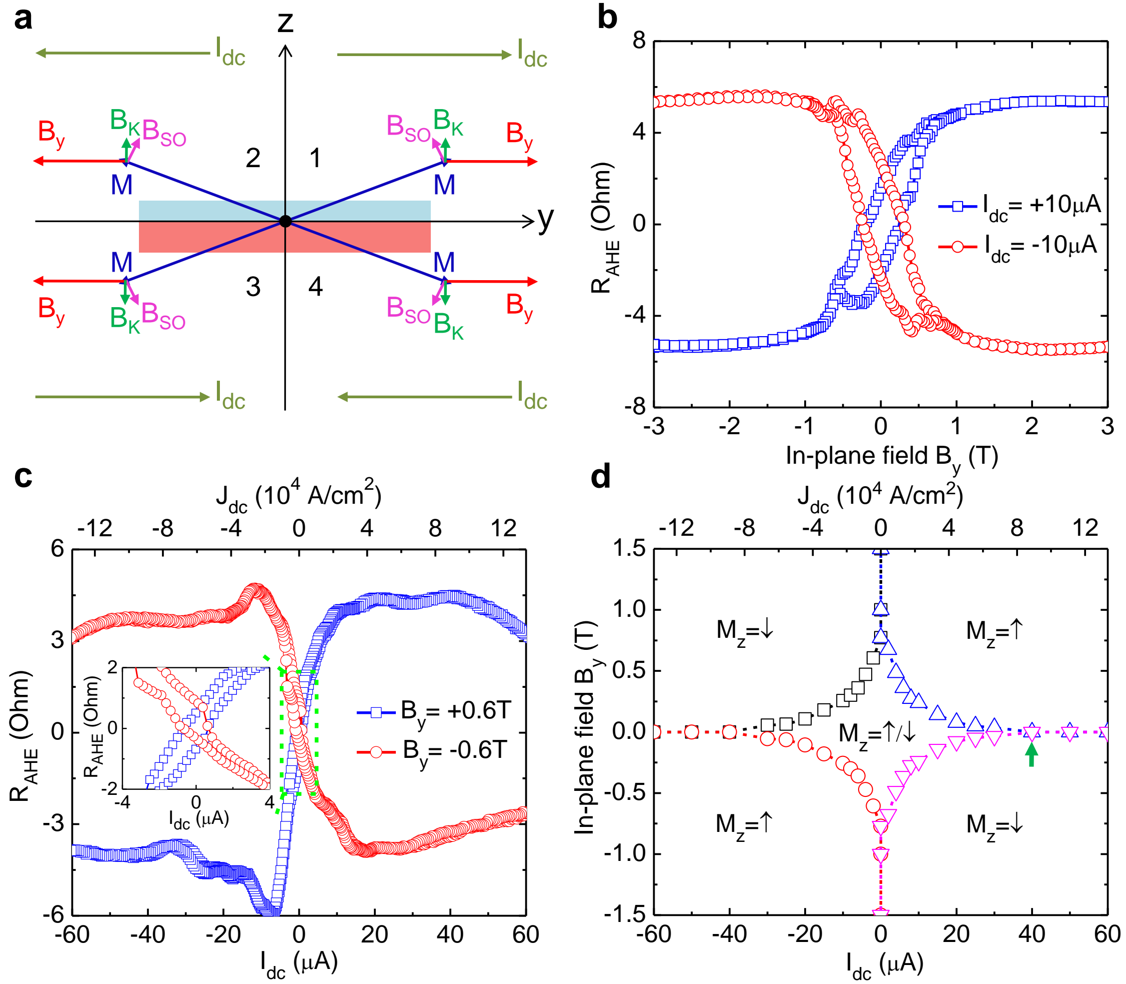

Figure 2-6. Magnetization switching due to the SOT induced by an in-plane DC current in the TI/Cr-doped TI bilayer heterostructure. **a,** Schematic of the four stable magnetization states (panels 1-4) when passing a large DC current, I_{dc}, and applying an in-plane external magnetic field, $\mathbf{B}_{\boldsymbol{y}}$, in the $\pm y$ directions. The effective spin-orbit field $\mathbf{B}_{\mathbf{SO}}$ induced by the DC current and the anisotropy field $\mathbf{B}_{\mathbf{K}}$ are both considered. **b,** The AHE resistance R_{AHE} as a function of the in-plane external magnetic field when passing a constant DC current with $I_{\mathrm{dc}} = +10\mu\mathrm{A}$ (blue squares) and $I_{\mathrm{dc}} = -10\mu\mathrm{A}$ (red circles) along the Hall bar, respectively, at 1.9K. **c,** Current-induced magnetization switching in the Hall bar device at 1.9K in the presence of a constant in-

plane magnetic field with $B_y = +0.6$T (blue squares) and $B_y = -0.6$T (red circles), respectively. Inset: expanded scale to show the hysteresis windows. **d,** Phase diagram of the magnetization state in the presence of an in-plane external magnetic field $\mathbf{B}_y$ and a DC current I_{dc}. The dashed lines and symbols (obtained from experiments) represent switching boundaries between the different states. Green arrow indicates the critical switching current density of 8.9×10^4 A/cm^2 when the required in-plane magnetic field is almost zero. In all panels, the symbol ↑ means $M_z > 0$ and ↓ means $M_z < 0$, not $M_z = \pm M_{\mathrm{S}}$. Figure is adapted with permission from ref. [57] (Y. Fan's publication).

2.4 Second Harmonic Method to Evaluate the Current-induced Spin-Orbit Torques

In order to quantitatively analyze the current-induced SOT in the TI/Cr-doped TI bilayer system, we carried out harmonic measurements of the AHE resistance to calibrate the effective spin-orbit field $\mathbf{B_{SO}}$ arising from the SOT. By sending an AC current, $I_{\mathrm{ac}}(t) = I_0 \sin(\omega t)$, into the Hall bar device, the alternating effective field, $\mathbf{B_{eff}}(t) = \mathbf{B_{SO}} \sin(\omega t)$, causes the magnetization $\mathbf{M}$ to oscillate around its equilibrium position, which gives rise to a second harmonic AHE resistance (as described in detail in the following): $R_{\mathrm{AHE}}^{2\omega} = -\frac{1}{2}\frac{dR_{\mathrm{AHE}}}{dI} I_0$. The second harmonic AHE resistance $R_{\mathrm{AHE}}^{2\omega}$ contains information of the effective field $\mathbf{B_{SO}}$ and has been utilized as an effective method to quantify it [9,116], as to be explained later. Here we introduce two different ways to measure this effective field by the second harmonic method [9], namely, one is to sweep the external magnetic field to large values, and the other one is to rotate the external magnetic field direction while keeping its magnitude fixed. Both ways give quantitatively the same effective field $\mathbf{B_{SO}}$ for a given AC current as discussed in details below.

The expression for extracting the effective spin-orbit field from the second harmonic signal is derived in refs [9,116] for the case of varying the magnitude of the external magnetic field while keeping its orientation fixed. Based on these references, we will first derive the formula for the second harmonic AHE resistance $R_{\mathrm{AHE}}^{2\omega}$ and then apply to the case of sweeping the in-plane external magnetic field for extracting the effective spin-orbit field.

For the Hall bar geometry used in this work (Fig. 2-3b), the external magnetic field is applied in the yz-plane making a polar angle θ_{B} with the z-axis (see Fig. 2-3a). For the harmonic measurements the device is excited by a small AC current, I_{ac}, flowing along the y-axis, while the Hall voltage, V_{H}, at first and second harmonics are simultaneously measured. The AC current takes the form, $I_{\mathrm{ac}} = I_0 \sin(\omega t)$, and the Hall resistance R_{H} can be Taylor expanded up to linear

order in I, $R_{\mathrm{H}}(I) = R_{\mathrm{H}}(0) + I(dR_{\mathrm{H}}/dI\,|_{I=0})$, giving rise to the Hall voltage at different harmonics:

$$V^{1\omega}(t) = V^{1\omega}\sin(\omega t)\,; V^{1\omega} = I_0 R_{\mathrm{H}}(0)$$

$$V^{2\omega}(t) = V^{2\omega}\cos(2\omega t); V^{2\omega} = -\left(\frac{I_0^2}{2}\right)\left(\frac{dR_{\mathrm{H}}}{dI}\,|_{I=0}\right). \qquad (2-2)$$

$V^{1\omega}$ and $V^{2\omega}$ can be directly measured by the standard lock-in technique [9,116]. In the yz-plane or xz-plane, as shown in Fig. 2-3a and Fig. 2-3b, the first harmonic Hall resistance is given by, $R_{\mathrm{H}}^{1\omega} = V^{1\omega}/I_0 = R_{\mathrm{H}}(0) = \beta B_{\mathrm{ext}}\cos\theta_{\mathrm{B}} + R_{\mathrm{A}}\cos\theta_{\mathrm{M}}$, where β is the ordinary Hall coefficient and R_{A} is the AHE coefficient; θ_{M} is the polar angle between the magnetization **M** and the z-axis. For clarity, we define the latter part as the first harmonic AHE resistance, $R_{\mathrm{AHE}}^{1\omega} = R_{\mathrm{A}}\cos\theta_{\mathrm{M}}$. The second harmonic Hall resistance is given by, $R_{\mathrm{H}}^{2\omega} = V^{2\omega}/I_0 = -\frac{1}{2}(dR_{\mathrm{H}}/dI\,|_{I=0})I_0$. Since the ordinary Hall coefficient β experimentally does not show any obvious dependence on the current around $I = 0$, *i.e.*, $d\beta/dI\,|_{I=0} = 0$, the second harmonic Hall resistance is therefore also referred to as the second harmonic AHE resistance, $R_{\mathrm{AHE}}^{2\omega} = V^{2\omega}/I_0 = -\frac{1}{2}(dR_{\mathrm{AHE}}/dI\,|_{I=0})I_0$. At this point we note that a full quantitative characterization of the Hall resistance would require inclusion of the planar Hall effect (PHE) resistance. However, in the yz-plane or xz-plane the PHE does not contribute to the first harmonic Hall resistance since $M_x = 0$ or $M_y = 0$, respectively. Furthermore, in Section 2.6 we will show that in the yz-plane the PHE contribution to the second harmonic Hall resistance is actually negligible for the device studied here. As a result, in the following we will focus mainly on the first and second harmonic signals from the AHE resistance.

Before introducing the low-frequency harmonic measurement, we first analyze the equilibrium orientation of the magnetization **M** in the presence of a large external magnetic field

in the yz-plane and without applying any current through the system. The equilibrium position can be obtained by balancing the torques due to the external magnetic field and the perpendicular anisotropy field, *i.e.*, the total torque $\boldsymbol{\tau}_{\mathbf{tot}} = -\gamma\mathbf{M} \times (\mathbf{B}_{\mathbf{ext}} + \mathbf{B}_{\mathbf{K}}) = 0$, which leads to the following equation (see Fig. 2-7a):

$$K\cos\theta_{\mathrm{M}}\sin\theta_{\mathrm{M}} = B_{\mathrm{ext}}(\sin\theta_{\mathrm{B}}\cos\theta_{\mathrm{M}} - \cos\theta_{\mathrm{B}}\sin\theta_{\mathrm{M}}), \qquad (2-3)$$

where K is the anisotropy coefficient. Note that the first harmonic AHE resistance reads, $R_{\mathrm{AHE}}^{1\omega} = R_{\mathrm{A}}\cos\theta_{\mathrm{M}}$. We performed the rotation experiment by fixing the external magnetic field to 2T and measured the $R_{\mathrm{AHE}}^{1\omega}$ as a function of θ_{B} in the yz-plane, as shown in Fig. 2-8. Then the numerical solution of equation (2-3) is fitted to the experimental data of $R_{\mathrm{AHE}}^{1\omega}$ to obtain the anisotropy coefficient $K = 0.9$T, as also illustrated in Fig. 2-8. Consequently, the relation between θ_{M} and θ_{B} is established. From the rotation experiment, R_{A} can also be determined to be 36 **Ω**. Note: the anisotropy field is written as $\mathbf{B}_{\mathbf{K}} = K\cos\theta_{\mathrm{M}}\hat{\boldsymbol{z}}$ because the anisotropy energy has the form $E_{anis} = -KM\cos^2\theta_{\mathrm{M}} = -\mathbf{B}_{\mathbf{K}} \cdot \mathbf{M}$. Knowing the $\mathbf{M}$ direction and that $\mathbf{B}_{\mathbf{K}}$ is out-of-plane, it is straightforward to derive the formula for $\mathbf{B}_{\mathbf{K}}$.

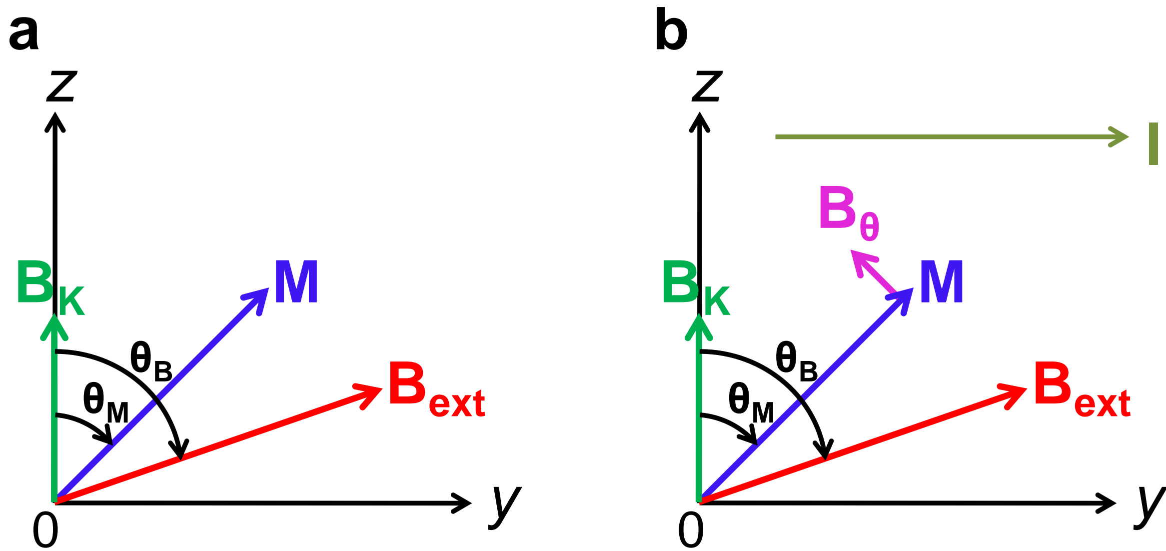

Figure 2-7. Equilibrium orientation of the magnetization in the presence of the external magnetic field and with/without the longitudinal current. **a**, The equilibrium orientation of the magnetization $\mathbf{M}$ in the presence of an external magnetic field $\mathbf{B_{ext}}$ with a constant magnitude of 2T. $\mathbf{B_K} = K\cos\theta_M\hat{\mathbf{z}}$ is the perpendicular anisotropy field. θ_M and θ_B are the polar angles of $\mathbf{M}$ and $\mathbf{B_{ext}}$ from the z-axis, respectively. **b**, The orientation of the magnetization $\mathbf{M}$ in the presence of current-induced effective spin-orbit field $\mathbf{B_\theta}$ which is transverse to the magnetization $\mathbf{M}$. Figure is adapted with permission from ref. [57] (Y. Fan's publication).

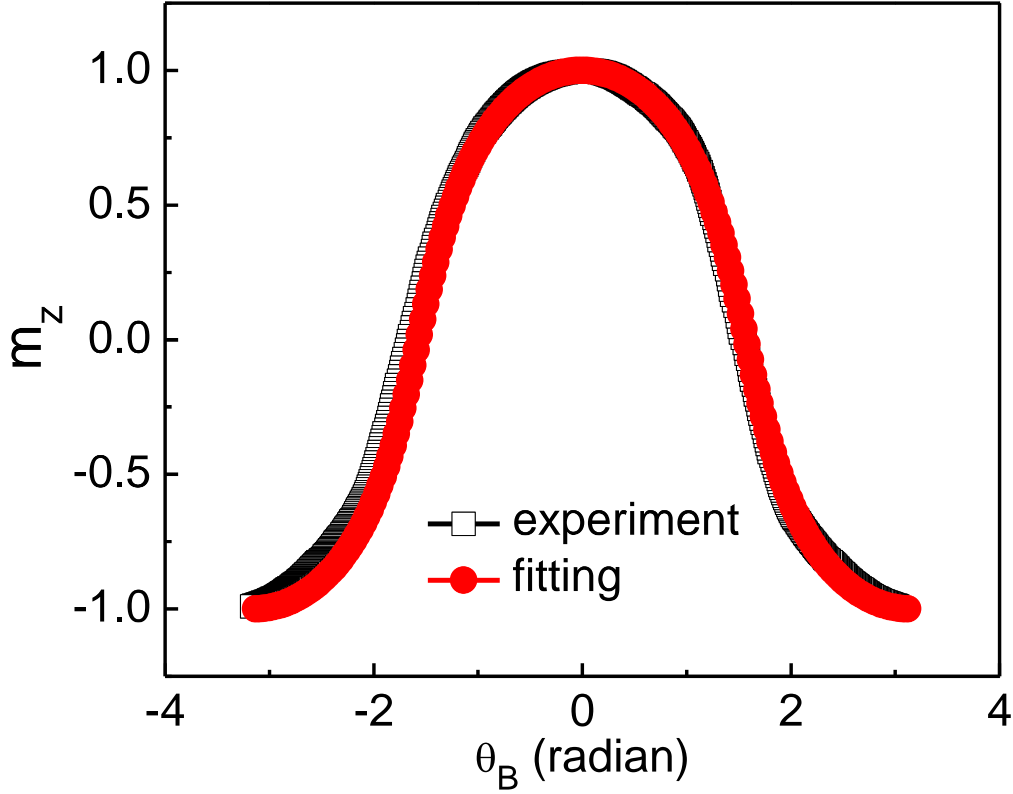

Figure 2-8. Fitting to obtain the anisotropy coefficient and the saturation AHE resistance. The normalized z-component of the magnetization, m_z (black squares), obtained from the rotation experiment ($m_z = \cos\theta_{\mathrm{M}} = R_{\mathrm{AHE}}^{1\omega}/R_{\mathrm{A}}$) and from the fitting by solving equation (2-3) (red circles), respectively, as a function of the field angle θ_{B}. In the fitting, we used $K = 0.9$T. Figure is adapted with permission from ref. [57] (Y. Fan's publication).

Now we derive, within the single domain model, the expression for the second harmonic AHE resistance for the case of varying magnitude of the external magnetic field applied along the y-axis (*i.e.*, in-plane). We are interested in the regime where the magnitude of the in-plane

external magnetic field, $|\mathbf{B}_y|$, is larger than K (so the magnetization is in a single domain state). In this case, the equilibrium condition of the magnetization, equation (2-3), gives $\theta_M = \pi/2$, *i.e.*, the equilibrium magnetization in the absence of current-induced effective spin-orbit field is pointing along the y-axis. However, when an AC current, $I_{\mathrm{ac}} = I_0 \sin(\omega t)$, is applied, the corresponding effective spin-orbit field, $\mathbf{B_{SO}} = I_{\mathrm{ac}} \lambda_{\mathrm{SO}} \hat{\boldsymbol{x}} \times \mathbf{m}$, transverse to the magnetization, as shown in Fig. 2-9, will cause the orientation of the magnetization to oscillate with an amplitude $\delta\theta_{\mathrm{M}}$, whose magnitude depends on the strength of the external magnetic field. This $\delta\theta_{\mathrm{M}}$ gives rise to a second harmonic AHE resistance as explained in ref. [9]. The amplitude $\delta\theta_M$, for the given I_0 and $\mathbf{B_y}$, can be obtained by balancing the torques due to the external magnetic field, the anisotropy field and the current-induced effective spin-orbit field (see Fig. 2-9), resulting in the following equation:

$$B_{\mathrm{SO}} - K\sin(\delta\theta_{\mathrm{M}})\cos(\delta\theta_{\mathrm{M}}) = -\left|B_y\right|\sin(\delta\theta_{\mathrm{M}}). \qquad (2-4)$$

We are interested in the case when the transverse fluctuation $\delta\theta_{\mathrm{M}} \ll 1$. To this end, expanding equation (2-4) up to first order in $\delta\theta_{\mathrm{M}}$ gives the solution, $\delta\theta_{\mathrm{M}} = -B_{\mathrm{SO}}/(\left|B_y\right| - K)$. Using this solution in conjunction with equation (2-2) gives the following equation for the second harmonic AHE resistance:

$$R_{\mathrm{AHE}}^{2\omega} = -\frac{1}{2}\frac{R_{\mathrm{A}} B_{\mathrm{SO}}}{\left(\left|B_y\right| - K\right)}. \qquad (2-5)$$

As we will show below, within the current-induced SOT model we can well obtain and verify the $1/(\left|B_y\right| - K)$ dependence of the second harmonic AHE signal.

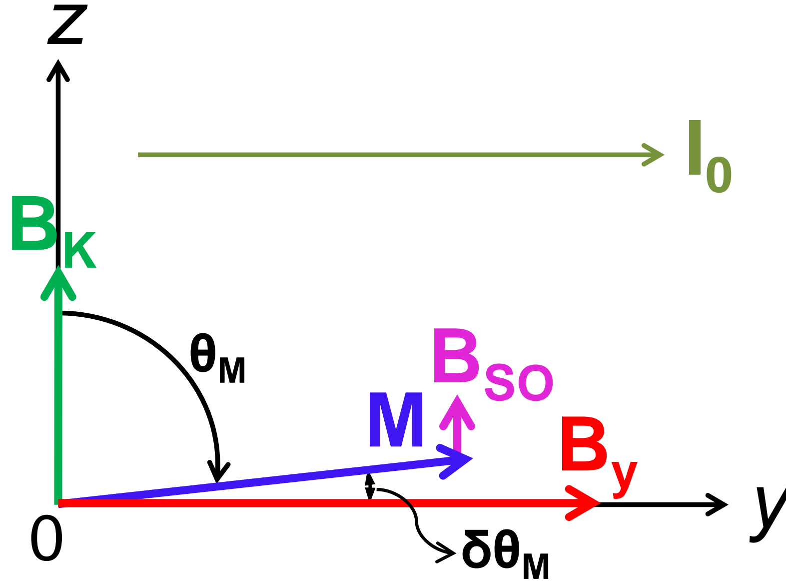

Figure 2-9. The orientation of the magnetization in the presence of a large in-plane external magnetic field $\mathbf{B_y}$ along the y-axis and an AC current, $I_{ac} = I_0 \sin(\omega t)$. $\mathbf{B_{SO}}$ is the current-induced effective spin-orbit field; $\delta\theta_M$ is the small transverse deflection caused by $\mathbf{B_{SO}}$. $\mathbf{B_K} = K\cos\theta_M \hat{\boldsymbol{z}}$ is the perpendicular anisotropy field. $\theta_M \approx \pi/2$. Figure is adapted with permission from ref. [57] (Y. Fan's publication).

In Fig. 2-10, we show the measured second harmonic AHE resistance $R_{AHE}^{2\omega}$ as a function of the in-plane external magnetic field when the input AC current is, $I_{ac}(t) = I_0 \sin(\omega t)$, where $I_0 = 2\mu A$ and $\omega = 15.8Hz$. Indeed, when the in-plane external magnetic field is larger than the saturation field (*i.e.*, $|B_y| > K$ and hence the magnetization is in a single domain state), the measured $R_{AHE}^{2\omega}$ value decreases when $|B_y|$ increases, as illustrated in regions I and III in Fig. 2-10. The $R_{AHE}^{2\omega}$ versus B_y curve in the large field region can be well fitted with equation (2-5), as also depicted in Fig. 2-10, and the effective spin-orbit field value is evaluated to be, $B_{SO} \approx$

± 26.2 mT, pointing along $+z$ or $-z$ depending on the direction of $\mathbf{B_y}$, which is consistent with the definition of $\mathbf{B_{SO}}$ in equation (2-1). Consequently, the $1/(|B_y| - K)$ scaling behavior of $R_{\mathrm{AHE}}^{2\omega}$ in the large field region confirms that the measured second harmonic signal indeed comes from the SOT-induced magnetization oscillation around its equilibrium position.

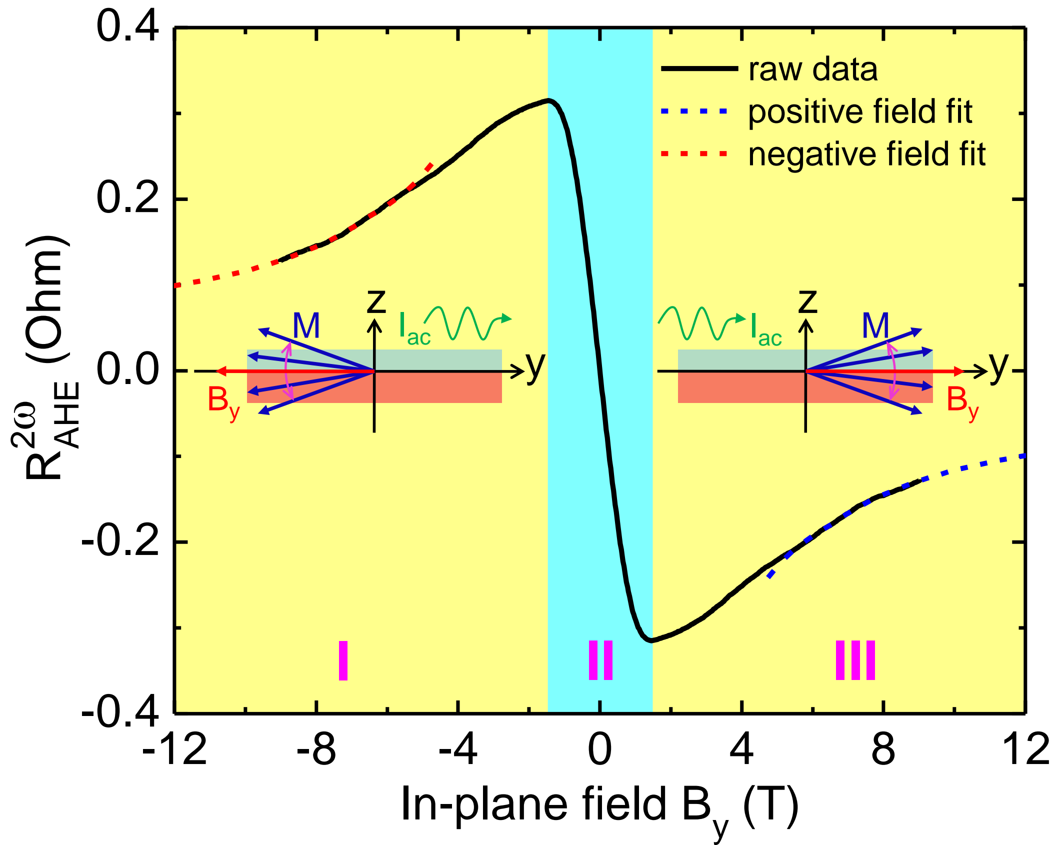

Figure 2-10. Second harmonic AHE resistance as a function of the in-plane external magnetic field. The shaded regions I, II, and III represent a single domain state pointing in the $-y$ direction, magnetization reversal, and a single domain state pointing in the y direction, respectively. The solid black line is the experimental raw data. The dashed lines denote the fitting proportional to $1/(|B_y| - K)$ in the negative field region (red dashed line) and in the

positive field region (blue dashed line), respectively. Inset figures in regions I and III show the magnetization oscillation around its equilibrium position when passing an AC current. The AC current amplitude is 2 μA and the frequency is 15.8Hz. Figure is adapted with permission from ref. [57] (Y. Fan's publication).

Besides second harmonic measurement by sweeping the in-plane external magnetic field, we also carried out the rotation experiment to find the angle dependence of the effective spin-orbit field. During the rotation experiment, we apply a large external magnetic field of constant magnitude, $B_{\text{ext}} = |\mathbf{B_{ext}}| = 2\text{T}$, to ensure single domain behavior, and extract the effective spin-orbit field by varying the orientation of $\mathbf{B_{ext}}$. Here, following ref. [9], we first derive the modified expression employed to extract the effective spin-orbit field.

In the rotation experiment the external magnetic field, $\mathbf{B_{ext}}$, can rotate continuously in the yz-plane, which allows us to probe the effective spin-orbit field, $\mathbf{B_{SO}}$, which is also lying in the yz-plane, as shown in Fig. 2-3a and Fig. 2-5. $\mathbf{B_{SO}}$ arises from the antidamping-like SOT [9]. We want to mention that the equally important field-like SOT term is shown to be an order of magnitude smaller, and its contribution to the second harmonic signal is negligible (see Section 2.6) when we do the rotation experiment in the yz-plane. With such a consideration in mind, using the form of the AHE resistance $R_{\text{AHE}} = R_{\text{A}}\cos\theta_{\text{M}}$ we get:

$$\frac{dR_{\text{AHE}}}{dI} = R_{\text{A}}\frac{d\cos\theta_{\text{M}}}{dI} = R_{\text{A}}\frac{d\cos\theta_{\text{M}}}{dB_{\theta}}b_{\theta}. \qquad (2-6)$$

Here, $\mathbf{B_{SO}} = B_{\theta}\hat{\boldsymbol{\theta}} = b_{\theta}I\hat{\boldsymbol{\theta}}$ represents the current-induced effective spin-orbit field, expanded up to first order in I, with its orientation shown in Fig. 2-7b. We define the clockwise-direction as the positive rotation direction and $\hat{\boldsymbol{\theta}}$ is the unit polar angle tangential vector. Next, similar to ref.

[9], noting that the change in θ_{M} caused by $\mathbf{B_{SO}}$ can be replaced by that due to the change in the component of the external magnetic field transverse to the magnetization, we write:

$$\frac{d\cos\theta_{\mathrm{M}}}{dB_{\theta}} = \frac{d\cos\theta_{\mathrm{M}}}{d(B_{\mathrm{ext}}\sin(\theta_{\mathrm{B}} - \theta_{\mathrm{M}}))} = \frac{1}{B_{\mathrm{ext}}\cos(\theta_{\mathrm{B}} - \theta_{\mathrm{M}})}\frac{d\cos\theta_{\mathrm{M}}}{d\theta_{\mathrm{B}}}. \quad (2-7)$$

Here, the essential difference from ref. [9] is that instead of the magnitude, B_{ext}, the orientation, θ_{B}, is varied. Using equations (2-2), (2-6) and (2-7), we immediately arrive at the formula for extracting B_{θ}:

$$R_{\mathrm{AHE}}^{2\omega} = -\frac{R_{\mathrm{A}}}{2B_{\mathrm{ext}}\cos(\theta_{\mathrm{B}} - \theta_{\mathrm{M}})}\frac{d(\cos\theta_{\mathrm{M}})}{d\theta_{\mathrm{B}}}B_{\theta} \quad (2-8)$$

i.e.,

$$B_{\theta} = -2B_{\mathrm{ext}}\cos(\theta_{\mathrm{B}} - \theta_{\mathrm{M}})\frac{R_{\mathrm{AHE}}^{2\omega}}{(dR_{\mathrm{AHE}}^{1\omega}/d\theta_{\mathrm{B}})}. \quad (2-9)$$

Following the above scenario, we performed the rotation experiment and the first and second harmonic AHE resistances, $R_{\mathrm{AHE}}^{1\omega}$ and $R_{\mathrm{AHE}}^{2\omega}$, were measured simultaneously [9,116], as a function of the field angle θ_{B} from $-\pi$ to π in the yz-plane. The results are displayed in Fig. 2-11a and Fig. 2-11b, respectively (in order to get the correct $R_{\mathrm{AHE}}^{1\omega}$, the ordinary Hall resistance component has been subtracted from the total first harmonic Hall resistance). As we know, the relation between θ_{M} and θ_{B} can be established by solving equation (2-3). Applying formula (2-9) to the measured $R_{\mathrm{AHE}}^{1\omega}$ and $R_{\mathrm{AHE}}^{2\omega}$, we immediately get the effective spin-orbit field B_{θ}. Shown in Fig. 2-11c is the obtained effective field value B_{θ} as a function of the rotation angle θ_{B} for different amplitudes of the AC current, I_{ac}, ranging from $1\mu\mathrm{A}$ to $5\mu\mathrm{A}$. Note that we get strictly negative values for B_{θ}, which means the effective field $\mathbf{B_{SO}}$ is pointing towards the $-\hat{\boldsymbol{\theta}}$ tangential direction (*i.e.*, counterclockwise). This is consistent with the magnetic field sweeping experiments displayed in Fig. 2-10 and the current-induced switching data in Fig. 2-6c. Equally important, we observe that the effective field B_{θ} is highly anisotropic, reaching the highest value

at $\theta_B = 0, \pm\pi$ (out-of-plane) and lowest at $\theta_B = \pm\frac{\pi}{2}$ (in-plane). The θ_B dependence of the effective spin-orbit field reveals that the SOT anisotropy is stronger than those reported for the AlO_x/Co/Pt and MgO/CoFeB/Ta systems [9], possibly due to the emergence of higher order terms in the SOT expression [9] when considering the strong SOC in TIs.

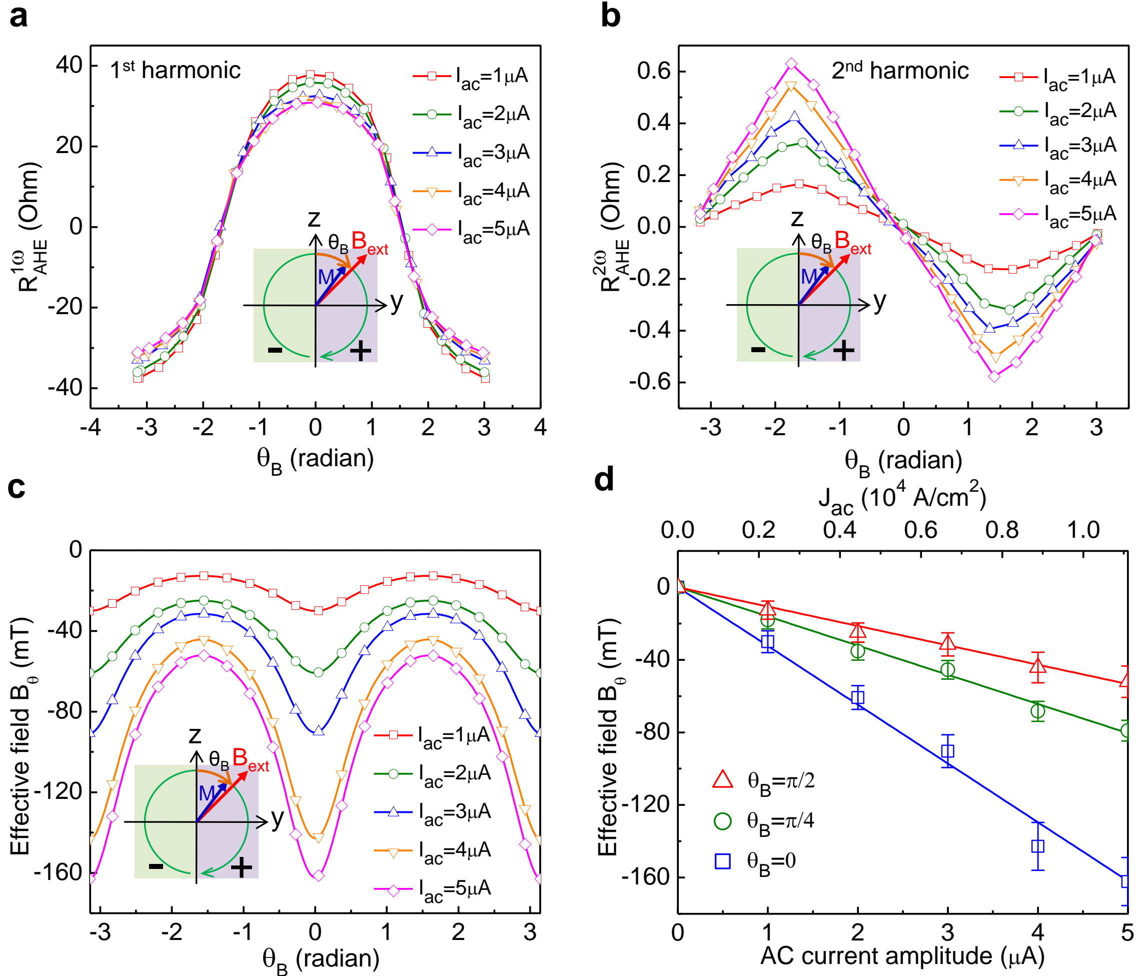

Figure 2-11. Harmonic signals and effective spin-orbit fields obtained from the rotation experiment. **a-b,** First and second harmonic AHE resistances, $R^{1\omega}_{AHE}$ and $R^{2\omega}_{AHE}$, as a function of the field angle θ_B for the applied AC current I_{ac} with different amplitudes ranging from 1 μA to 5 μA, when θ_B varies from $-\pi$ to π in the yz-plane as shown in the inset figures. **c,** The effective spin-orbit field as a function of θ_B for the applied AC current I_{ac} with different amplitudes

ranging from 1 μA to 5 μA. **d,** The effective spin-orbit field as a function of the AC current amplitude I_{ac} for three different θ_{B} angles, $\theta_{\mathrm{B}} = 0,\ \pi/4$ and $\pi/2$, respectively. Straight lines are the linear fittings. Error bars represent standard errors. In all the rotation experiments, the $\mathbf{B}_{\mathbf{ext}}$ field magnitude is fixed at 2 T and the temperature is kept at 1.9 K. Figure is adapted with permission from ref. [57] (Y. Fan's publication).

Furthermore, we also plot the effective field value B_{θ} as a function of the AC current amplitude for three different θ_{B} angles, $\theta_{\mathrm{B}} = 0, \pi/4$ and $\pi/2$, in Fig. 2-11d, respectively. The effective field B_{θ} has a linear dependence on the AC current amplitude (or AC current density amplitude J_{ac}), and the $|B_{\theta}|/J_{\mathrm{ac}}$ ratio ranges from 0.0048 mT/(A/cm^2) to 0.0146 mT/(A/cm^2), which is nearly three orders of magnitude larger than those reported in HMFHs [9,116]. Using the spin-torque ratio (in heavy metals, it evolves to the spin-Hall angle) [9,38], defined as $\vartheta_{\mathrm{ST}} = \frac{2eM_{\mathrm{S}}B_{\theta}t_{\mathrm{Cr-TI}}}{\hbar J_{\mathrm{ac}}}$, where e is the electron charge, $\hbar$ is the Planck's constant divided by 2π and $t_{\mathrm{Cr-TI}}$ is the Cr-doped TI layer thickness, to quantify the antidumping-like SOT, we find ϑ_{ST} value ranges from 140 to 425, depending on θ_{B}, which is almost three orders of magnitude larger than those reported in HMFHs. Here, ϑ_{ST} has the same sign with the one revealed in Pt [42]. The sign of the current-induced SOT agrees with the spin-momentum locking induced surface spin polarization in TIs, which suggests that the topological surface states can provide a much more efficient way to generate SOT compared with heavy metals [127]. Besides the topological surface states, the possible contribution from the bulk of TI and the interfacial Rashba-type SOC interaction as discussed in refs. [127,129,137,138] warrant further theoretical and experimental work.

Now we turn to the field-like SOT and see how much it contributes to the second harmonic signal. As described in equation (2-1), the field-like SOT reads, $\boldsymbol{\tau}_{\mathbf{F}} = -\gamma \mathbf{M} \times \mathbf{B}_{\mathbf{F}}$, where the effective spin-orbit field is, $\mathbf{B}_{\mathbf{F}} = I\lambda_{\mathrm{F}}\hat{\boldsymbol{x}}$. This effective field is pointing along x (or $-x$) direction (*i.e.*, transverse to the Hall bar structure). In order to measure this effective field by the second harmonic method, the external magnetic field $\mathbf{B}_{\mathbf{ext}}$ needs to rotate in the xz-plane (detailed explanation can be found in ref. [9]). We managed to reconstruct our measurement setup such that $\mathbf{B}_{\mathbf{ext}}$ can rotate locally in the xz-plane near the $\theta_{\mathrm{B}} = 0$ and $\theta_{\mathrm{B}} = \pi$ points, as shown in the insets of Fig. 2-12a-b. Similar to the rotation experiment we already discussed before, now we rotate $\mathbf{B}_{\mathbf{ext}}$ near the $\theta_{\mathrm{B}} = 0$ and $\theta_{\mathrm{B}} = \pi$ points in the xz-plane while keeping its magnitude fixed at 2T. Meanwhile an in-plane AC current is sent in the Hall bar device along the y-direction. The first and second harmonic AHE resistances, $R_{\mathrm{AHE}}^{1\omega}$ and $R_{\mathrm{AHE}}^{2\omega}$, are measured simultaneously. The first harmonic AHE resistance is similar to the one as shown in Fig. 2-11a. The second harmonic AHE resistance, $R_{\mathrm{AHE}}^{2\omega}$, which is caused by the alternating effective field arising from the field-like SOT, is displayed in Fig. 2-12a-b, for near the $\theta_{\mathrm{B}} = 0$ and $\theta_{\mathrm{B}} = \pi$ regions, respectively. Since at the $\theta_{\mathrm{B}} = 0$ and $\theta_{\mathrm{B}} = \pi$ points, $R_{\mathrm{AHE}}^{2\omega}$ and $dR_{\mathrm{AHE}}^{1\omega}/d\theta_{\mathrm{B}}$ all approach zero, using the L'Hopital's rule, the formula employed to extract the effective spin-orbit field can be modified as, $B_{\theta} = -2B_{\mathrm{ext}}\cos(\theta_{\mathrm{B}} - \theta_{\mathrm{M}})\,(\frac{dR_{\mathrm{AHE}}^{2\omega}}{d\theta_{\mathrm{B}}})/(d^2\,R_{\mathrm{AHE}}^{1\omega}/d\theta_{\mathrm{B}}{}^2)$. The obtained results are plotted in Fig. 2-12c. It can be seen that the effective field, $B_{\mathrm{F}} = B_{\theta}$, is negative at $\theta_{\mathrm{B}} = 0$ and changes to positive at $\theta_{\mathrm{B}} = \pi$, which means the effective field is pointing along the $-x$ direction for both cases. From Fig. 2-12c we can get the effective field versus current density ratio is $\frac{|B_{\mathrm{F}}|}{J_{\mathrm{ac}}} = 5 \times 10^{-4}$ mT/(A/cm^2), which is 30 times smaller than the one revealed from the antidamping-like SOT (1.46×10^{-2} mT/(A/cm^2)) at $\theta_{\mathrm{B}} = 0$ as discussed before.

The above analysis is valid if we assume the PHE coefficient is zero. If we don't neglect the PHE contribution (the PHE coefficient is measured to be around -3Ω), by combining the second harmonic measurements in the yz-plane and xz-plane and using the iteration method as introduced in ref. [9], we can get the corrected effective field vs. current density ratio is 9×10^{-4} mT/(A/cm^2) for the field-like SOT and 1.47×10^{-2} mT/(A/cm^2) for the antidamping-like SOT at $\theta_\mathrm{B} = 0$. The field-like SOT is thus still much smaller than the antidamping-like SOT.

When we carry out the second harmonic measurement by rotating the $\mathbf{B_{ext}}$ field in the yz-plane, the effective spin-orbit field from the field-like SOT mainly affects the second harmonic signal through the modulation of the PHE resistance [9]. Since the PHE resistance is very small compared with the AHE resistance (Section 2.6), the total effect from the field-like SOT to the second harmonic signal is almost negligible when we do the rotation experiment in the yz-plane, and the major contribution to the second harmonic signal (Fig. 2-11b) is thus from the antidamping-like SOT.

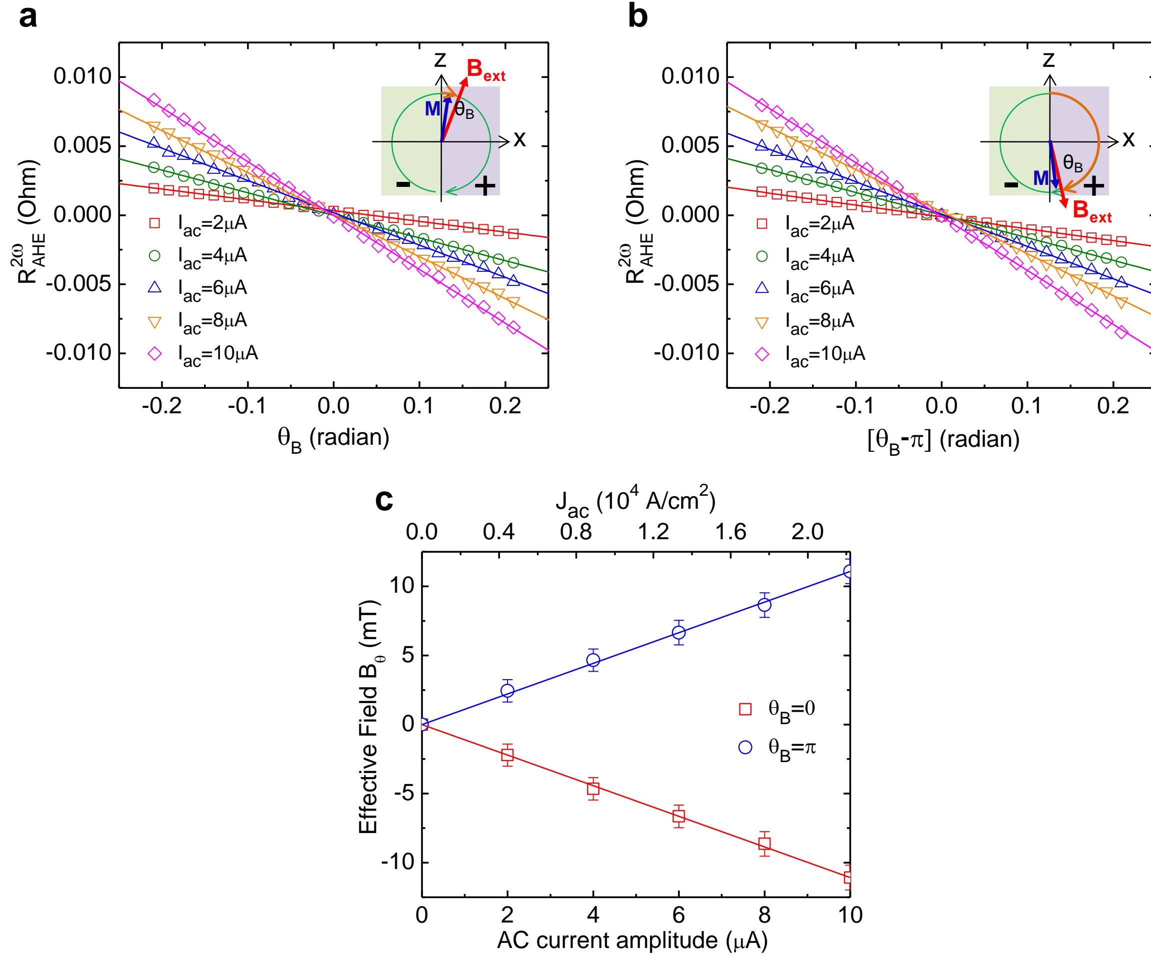

Figure 2-12. Second harmonic measurement to evaluate the field-like SOT. **a-b**, Second harmonic AHE resistance, $R^{2\omega}_{\mathrm{AHE}}$, as a function of the field angle θ_{B} for the applied AC current I_{ac} with different amplitudes ranging from 2 μA to 10 μA, when θ_{B} varies locally near $\theta_{\mathrm{B}} = 0$ and π in the xz-plane, respectively. **c**, The transverse effective spin-orbit field as a function of the AC current amplitude I_{ac} for two different θ_{B} angles, $\theta_{\mathrm{B}} = 0$ and π, respectively. In the experiments, the $\mathbf{B}_{\mathbf{ext}}$ field magnitude is fixed at 2 T and the temperature is kept at 1.9 K. Straight lines in the figures are linear fittings. Figure is adapted with permission from ref. [57] (Y. Fan's publication).

We conclude this section by comparing the revealed antidamping-like SOT in the TI/Cr-doped TI bilayer heterostructure with the one reported in the HMFHs (*e.g.*, MgO/CoFeB/Ta heterostructure). In the TI/Cr-doped TI bilayer heterostructure, we demonstrated the magnetization switching by the (I_{dc}-fixed, $\mathbf{B}_y$-driven) and the ($\mathbf{B}_y$-fixed, I_{dc}-driven) experiments which reveal that the SOT induced by the in-plane current is very large. The critical switching current density is below 8.9×10^4 A/cm^2 at 1.9K, which is almost two orders of magnitude smaller than the one required in HMFHs. Then we analyzed the current-induced SOT by extracting the effective spin-orbit field using second harmonic measurement of the AHE resistance. We found the $|B_{\mathrm{SO}}|/J_{\mathrm{ac}}$ ratio, as well as the spin-torque ratio ϑ_{ST} , is nearly three orders of magnitude larger than the ones reported in HMFMs. The comparison of these quantities is summarized in Table 2-2. Our measured results in the TI/Cr-doped TI bilayer heterostructure suggest that TIs are potentially much more efficient materials for generating SOT than heavy metals, and when integrated with magnetic materials, the TI-based magnetic structures may lead to the innovation of new SOT memory and logic devices with much lower power consumption.

Table 2-2. Comparison of the SOTs generated by TIs and heavy metals

Structures	**TI/Cr-doped TI,** ref.[57]	**Ta/CoFeB/MgO stack,** ref.[9,59]
Switching current density	~10^4 (A/cm^2)	~10^6 (A/cm^2)
B_{SO} vs. current density ratio	~10^{-3} mT/(A/cm^2)	~10^{-6} mT/(A/cm^2)
M_{S}	M_{S} (Cr-(Bi, Sb)$_2$Te$_3$) : M_{S} (CoFeB) ≈ 1:100	
Spin-torque ratio ϑ_{ST}	140~425 (at 1.9K)	~0.15 (at 300K)

2.5 Thermal Effect and Temperature Dependence of the Switching Current Density

In this section, we analyze the thermal effect and the temperature dependence of the switching behavior in the TI/Cr-doped TI bilayer heterostructure, which are important for practical applications. First, we will determine the Curie temperature in the TI/Cr-doped TI bilayer heterostructure. In order to do that, we carried out the out-of-plane Hall measurement at different temperatures to determine the trend in the coercivity field, B_C, as a function of the temperature. The result is shown in Fig. 2-13. We observe that the B_C changes dramatically as the temperature increases, indicating a decrease in the magnetization magnitude. The B_C approaches zero when the temperature is around 8.5K, and consequently we can estimate the Curie temperature is about 8.5K in the Cr-doped TI layer. From the trend in B_C we may underestimate the Curie temperature and a more accurate estimation can be provided by the Arrott-Noakes method [107]. Nevertheless, our estimation here is good enough to demonstrate the pronounced ferromagnetic ordering in the TI/Cr-doped TI bilayer heterostructure in the SOT experiments performed before.

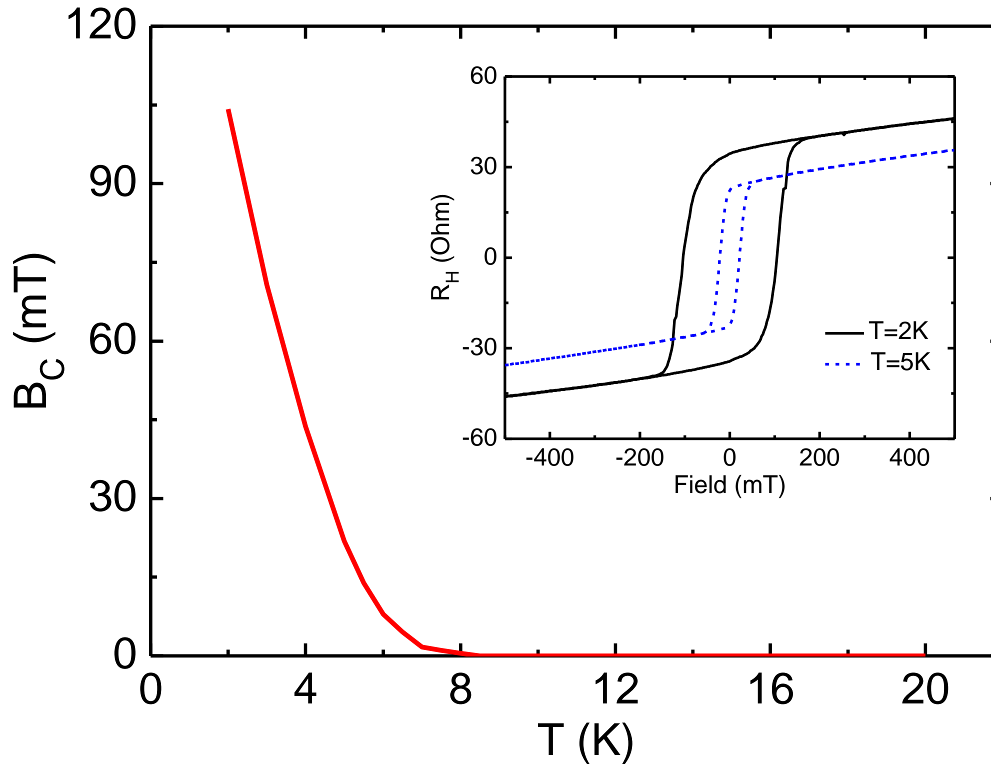

Figure 2-13. The coercivity field B_C as a function of the temperature. B_C approaches zero at around 8.5K. Inset: the out-of-plane Hall resistance hysteresis loops for two different temperatures, $T = 2\text{K}$ and $T = 5\text{K}$. Figure is adapted with permission from ref. [57] (Y. Fan's publication).

Now we examine the temperature dependence of the critical switching current density in the bilayer heterostructure. Experiments on the in-plane DC current induced magnetization switching in the presence of an in-plane external magnetic field are carried out at different temperatures and the corresponding phase diagrams at different temperatures are obtained, similar to Fig. 2-6d. The critical switching current density, defined as the current density needed to switch the magnetization when the in-plane external magnetic field approaches zero, can be

obtained from the phase diagram. The anisotropy field coefficient, which is also a function of temperature, can be obtained using the method introduced in Section 2.4. In Fig. 2-14, we plot both the critical switching current density J_{switch} and the anisotropy field coefficient K as a function of temperature. We can observe that both J_{switch} and K decrease as the temperature increases. Interestingly, the critical switching current density approaches zero at around 8K, while the anisotropy field coefficient still displays some remnant value even at 9K, possibly due to the fact that the in-plane DC current induced magnetization switching is likely multi-domain switching while the anisotropy field coefficient obtained here is for the single domain case.

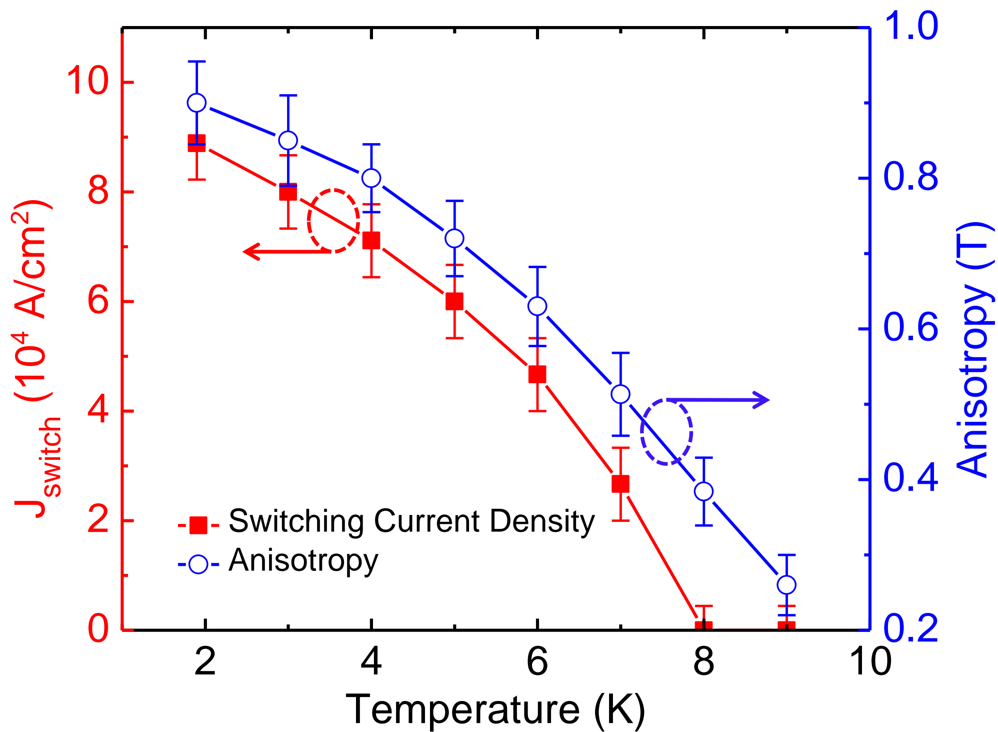

Figure 2-14. The critical switching current density and the anisotropy field coefficient as a function of temperature. The anisotropy field coefficient is determined using the method introduced in Section 2.4. Figure is adapted with permission from ref. [57] (Y. Fan's publication).

The temperature dependence of the critical switching current density indicates that the thermal effect is very crucial when determining the strength of the current-induced SOT in the bilayer heterostructure. Therefore, it is important to estimate the temperature change on the device due to the Joule heating. This is done by measuring the longitudinal resistance R_{xx}, as a function of temperature (T) and comparing it with the measurement of R_{xx} as a function of current (I). First, the longitudinal resistance R_{xx} was measured as a function of temperature T in the presence of a constant out-of-plane external magnetic field of 2T. The corresponding percentage change in R_{xx}, defined as $\Delta R_{xx}\% = 100 \times [R_{xx}(T) - R_{xx}(1.9\text{K})]/R_{xx}(1.9\text{K})$, is plotted in Fig. 2-15 (black solid circles). Next, R_{xx} was measured at $T = 1.9\text{K}$ (the temperature provided surrounding the device) as a function of the current in the presence of the same out-of-plane external magnetic field of 2T (this field is large enough so that the current induced SOT cannot tilt the magnetization too much). The measured percentage change in R_{xx} for this case, defined as $\Delta R_{xx}\% = 100 \times [R_{xx}(I) - R_{xx}(I = 0)]/R_{xx}(I = 0)$, is also plotted in Fig. 2-15 (blue open circles). Comparing the two cases we can see that for a current of $I = 15\mu\text{A}$, the temperature rises by ~ 2.5 K. In the current-induced magnetization switching experiments (Fig. 2-6b and Fig. 2-6c), this is in agreement with the fact that for this range of currents the sample is still below the Curie temperature $T_{\text{C}} = 8.5\text{K}$ and shows hysteretic switching (see Fig. 2-6b and Fig. 2-6c inset). However, this Joule heating might assist the current-induced magnetization switching by lowering the anisotropy field (Fig. 2-14). On the other hand, for the maximum AC current amplitude of $I_0 = 5\mu\text{A}$ (root mean square value is $3.54\,\mu\text{A}$) in the second harmonic experiments (Fig. 2-11), the corresponding rise in temperature is ~ 1 K and thus is not expected to affect the strength of the extracted effective spin-orbit field. We also note that the modulation of the Hall resistance due to a modulating temperature via Joule heating will lead to the

generation of only a third harmonic Hall voltage signal [9] and thus will not affect the second harmonic measurements.

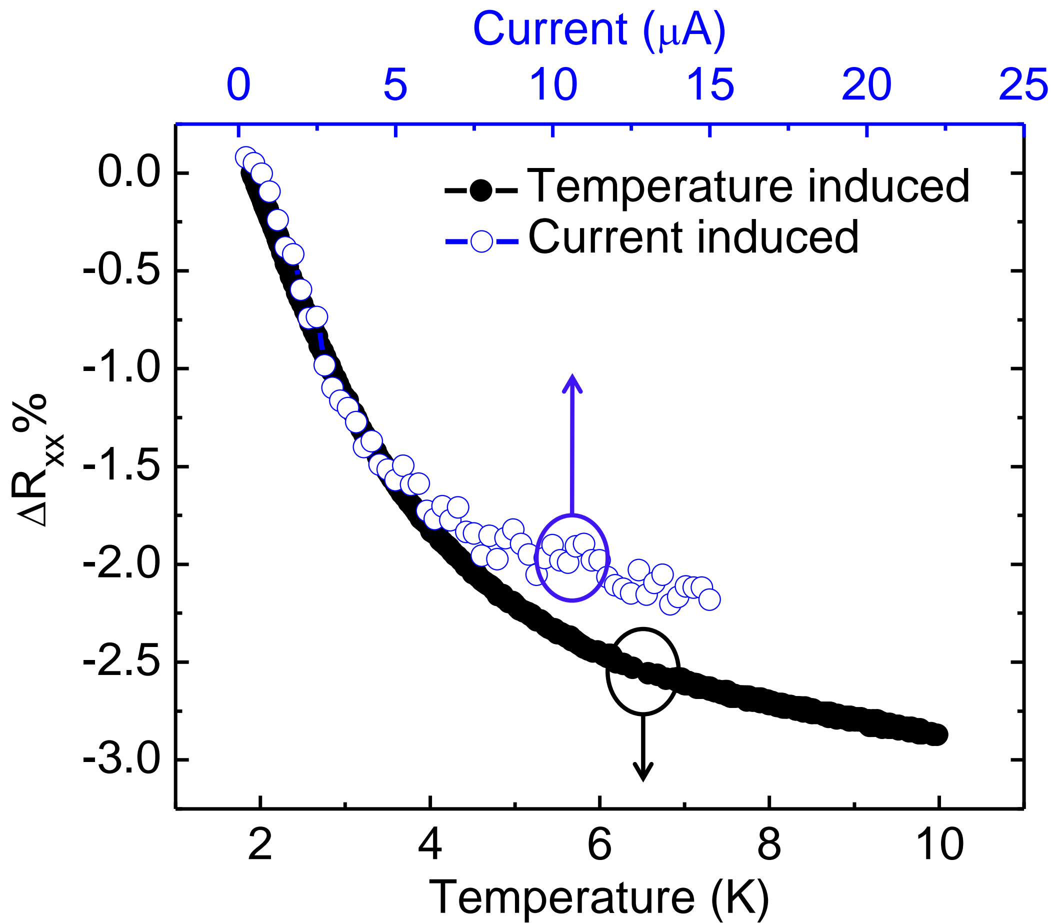

Figure 2-15. The percentage change in R_{xx} as a function of the temperature (bottom abscissa) and the current (upper abscissa), respectively. The corresponding rise in temperature due to current-induced Joule heating can be obtained by comparison. For example, when the current is 15 μA, the corresponding $\Delta R_{xx}\%$ is ~ -2.2, and the corresponding temperature is ~4.4 K, meaning the rise in temperature is around 2.5 K. A constant out-of-plane external magnetic field of 2T is applied in the measurements. Figure is adapted with permission from ref. [57] (Y. Fan's publication).

2.6 Discussion on the Switching Process, the Anisotropic Magneto-Resistance (AMR) Effect and the Planar Hall Effect (PHE) in the Bilayer Heterostructure

In this section, we analyze the current-induced switching process in the bilayer heterostructure and reveal that the switching is most likely multi-domain switching. The multi-domain switching process is partially the reason why the critical switching current density is so small (~10^4 (A/cm^2)) in this bilayer. In order to do that, we compare the switching phase diagram revealed in the experiments (Fig. 2-6d) with the one obtained from the single domain simulations. We find that the switching current density exhibited in the experiment is nearly one order of magnitude smaller than the one required for single domain switching. As a result, the current-induced magnetization switching in our experiment occurs most likely via a multi-domain switching process (Fig. 2-6c). The single domain simulations were performed by solving the extended LLG equation, where we only added the antidamping-like SOT since it is much larger than the field-like SOT in our device:

$$\frac{\partial \mathbf{M}}{\partial t} = -\gamma \mathbf{M} \times \mathbf{B_{eff}} + \frac{\alpha}{M_S} \mathbf{M} \times \frac{\partial \mathbf{M}}{\partial t} - \gamma \mathbf{M} \times \mathbf{B_{SO}} \qquad (2-10)$$

Here, $\mathbf{B_{eff}} = \mathbf{B_{ext}} + K\cos\theta_M \hat{\mathbf{z}}$ stands for the sum of the external magnetic field and the anisotropy field; $\boldsymbol{\tau}_{\mathbf{SO}} = -\gamma \mathbf{M} \times \mathbf{B_{SO}}$ is the antidamping-like SOT induced by the in-plane current I_{dc}; the corresponding effective spin-orbit field is $\mathbf{B_{SO}} = I_{dc}\lambda_{SO}\hat{\mathbf{x}} \times \mathbf{m}$, as described in detail in Section 2.3. For a certain in-plane current density J_{dc}, $\mathbf{B_{SO}}$ can be obtained via the second harmonic measurements (Fig. 2-11d), from which the $|B_{SO}|/J_{dc}$ ratio is known to be between 0.0048 mT/(A/cm^2) and 0.0146 mT/(A/cm^2). For simplicity, using the parameters, $\gamma = 1.8 \times 10^{11}\ \mathrm{rad \cdot s^{-1} \cdot T^{-1}}$, $\alpha = 0.1$ (it turns out that the choices of γ and α do not affect the simulation results of the phase diagram), $M_S = 16\ \mathrm{emu/cm^3}$ and $|B_{SO}|/J_{dc}$ =0.0146

mT/(A/cm^2), the phase diagram can be readily obtained by initializing the magnetization to point both up ($+z$ direction) and down ($-z$ direction) and allowing it to relax to the equilibrium positions according to equation (2-10). The resulting phase diagram for the case of positive in-plane current I_{dc} and positive in-plane external magnetic field in the y-direction is shown in Fig. 2-16. For comparison with the experiments, the corresponding phase diagram measured experimentally, namely Fig. 2-6d, is superimposed in Fig. 2-16. As can be seen, the critical current for magnetization switching within the single domain model is approximately one order of magnitude larger than the one we measured experimentally. This one order of magnitude difference could be attributed to multi-domain switching, possibly in conjunction with current-induced heating effect, as has also been seen for HMFHs [42].

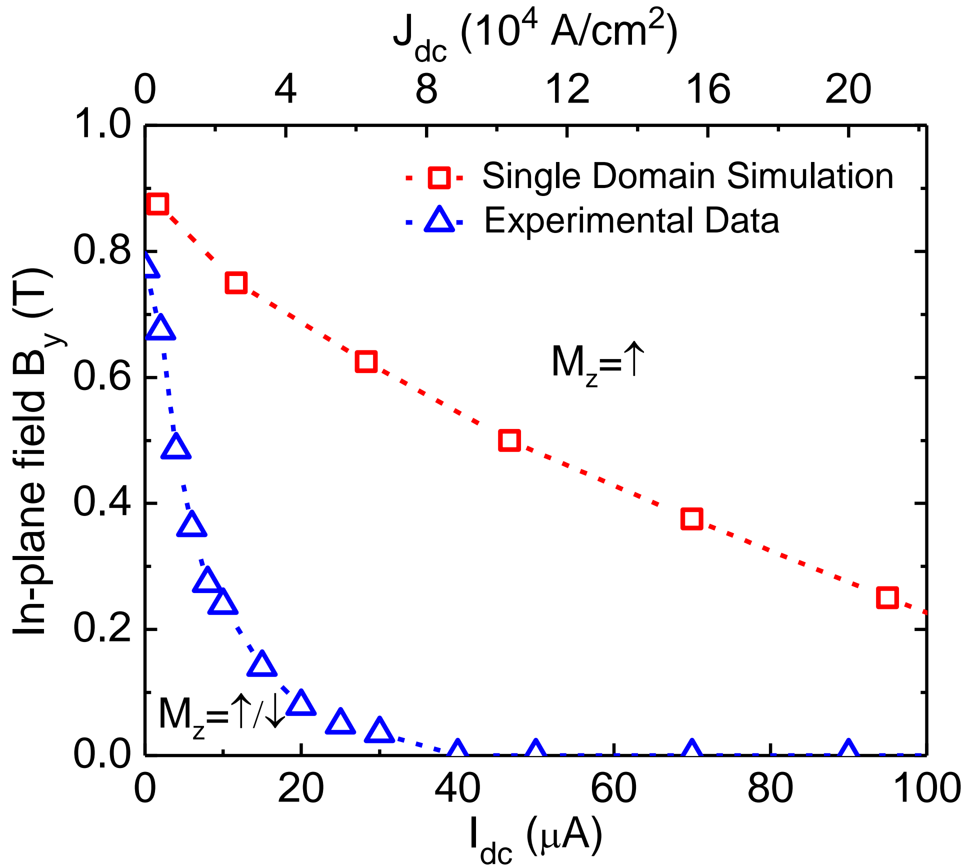

Figure 2-16. Comparison of the phase diagrams obtained from the experiments (blue triangles) and from the single domain simulations (red squares), for the case of positive in-plane current I_{dc} and positive in-plane external magnetic field applied in the y-direction. The symbol ↑ means $M_z > 0$ and ↓ means $M_z < 0$, not $M_z = \pm M_S$. Figure is adapted with permission from ref. [57] (Y. Fan's publication).

In addition, it is worth mentioning that in the perpendicular external magnetic field induced switching hysteresis in the absence of the in-plane DC current, as shown in Fig. 2-3c, the measured coercivity field (around 0.1T) is about one order of magnitude smaller than the perpendicular anisotropy field coefficient (0.9T as measured for the single domain case, see

Section 2.4), which suggests that the magnetization switching in our micrometer scale Hall bar device most likely favors multi-domain switching in the low field region.

Besides the detailed switching process, the anisotropic magneto-resistance (AMR) effect and the planar Hall effect (PHE) in the bilayer heterostructure are also very important for determining the current-induced SOT. AMR effect depends on the angle between the magnetization **M** and the electric current direction (*i.e.*, y-direction). In order to measure the AMR effect and the associated PHE in our Hall bar device, we reconstruct our experiment setup such that the external magnetic field $\mathbf{B_{ext}}$ with constant magnitude (2T) can rotate in the xy-plane, as illustrated in the insets of Fig. 2-17a-b. A small probing AC current (1μA) is applied along the y-direction. The external magnetic field $\mathbf{B_{ext}}$ is large enough to ensure single domain state of the magnetization and when we rotate $\mathbf{B_{ext}}$, the magnetization **M** follows $\mathbf{B_{ext}}$. Both the longitudinal sheet resistance and the transverse Hall resistance are measured simultaneously. The results are shown in Fig. 2-17a and Fig. 2-17b, respectively. In Fig. 2-17a, we plot the percentage change in the sheet resistance, $\Delta R_{\mathrm{sheet}}\%$, as a function of the azimuthal angle φ. $\Delta R_{\mathrm{sheet}}\%$ is defined as $\Delta R_{\mathrm{sheet}}\% = 100 \times (R_{\mathrm{sheet}} - R_{\perp})/R_{\perp}$, where $R_{\perp}$ is the sheet resistance when **M** is perpendicular to the current direction. From Fig. 2-17a we can observe that the sheet resistance has a maximum value when **M** is parallel to the current direction and approaches the minimum value when **M** is perpendicular to the current direction. This agrees with the general formula for the AMR effect, $R_{sheet}(\varphi) = R_{\perp} + \left(R_{\parallel} - R_{\perp}\right)\cos^2(\pi/2 - \varphi)$, where $\pi/2 - \varphi$ is the angle between **M** and the current direction (y-axis) and $R_{\parallel}$ is the sheet resistance in the special case when **M** is parallel to the current direction. In Fig. 2-17a we can see that $\Delta R_{\mathrm{sheet}}\%$ is very small in the whole range of φ, indicating that $R_{\parallel}$ does not differ from $R_{\perp}$ too much.

The transverse PHE resistance, R_{PHE}, is plotted in Fig. 2-17b as a function of the azimuthal angle φ. The PHE resistance depends on the product $M_x M_y$ where M_x and M_y are the magnetization components along the x and y axes [9], respectively. As a result, the PHE resistance is simply zero in the yz-plane or xz-plane. In the xy-plane, the PHE resistance has a simple formula [9], $R_{\mathrm{PHE}} = R_{\mathrm{P}} s\mathrm{in}(2\varphi)$, where R_{P} is the PHE coefficient. In Fig. 2-17b we can clearly see the double periods for φ from 0 to 2π, and the coefficient R_{P} can be obtained as $R_{\mathrm{P}} \cong -3\Omega$, which is much smaller than the AHE coefficient, $R_{\mathrm{A}} = 36\Omega$. Next, we will estimate how much the PHE resistance affects the determination of the effective spin-orbit field when we perform the second harmonic measurements in the yz-plane. In the yz-plane, the general formula for the second harmonic Hall resistance is (see ref. [9]),

$$R_{\mathrm{H}}^{2\omega} = -\frac{R_{\mathrm{A}}}{2B_{\mathrm{ext}}\cos(\theta_{\mathrm{B}} - \theta_{\mathrm{M}})}\frac{d(\cos\theta_{\mathrm{M}})}{d\theta_{\mathrm{B}}}B_{\theta} + \frac{R_{\mathrm{P}}\sin^2\theta_{\mathrm{M}}}{B_{\mathrm{ext}}\sin\theta_{\mathrm{B}}}B_{\varphi}\,, \qquad (2-11)$$

where B_{θ} is the effective field along the polar angle direction and B_{φ} is the effective field along the azimuthal angle direction. When we perform the rotation experiments in the yz-plane, B_{θ} stands for the effective field arising from the antidamping-like SOT and B_{φ} the effective field from the field-like SOT. Now let us show that in the yz-plane, the PHE contribution to the second harmonic signal is indeed negligible. Suppose we use an AC current with amplitude of 1 μA, so $B_{\varphi} \approx 2\mathrm{mT}$ and $B_{\theta} = -32.67\mathrm{mT}$ (see Section 2.4). In the $\theta_{\mathrm{B}} \approx 0$ region, the latter part in equation (2-11) stands for $\sim R_{\mathrm{P}}B_{\varphi}/(\frac{R_{\mathrm{A}}B_{\theta}}{2} + R_{\mathrm{P}}B_{\varphi}) \approx 1\%$ of the total signal; when $\theta_{\mathrm{B}} \neq 0$, *e.g.*, at $\theta_{\mathrm{B}} = \pi/2$, the latter part in equation (2-11) can be estimated to be -0.003 Ω, while the total measured second harmonic resistance is -0.167 Ω at $\theta_{\mathrm{B}} = \pi/2$ (see Fig. 2-11b). In other words, the latter part in equation (2-11) only accounts for 1.8% of the total signal. In conclusion, the field-like SOT induced second harmonic resistance is indeed negligible when we perform the

rotation experiments in the yz-plane, and to a good approximation, we have attributed all of the measured second harmonic signals to the antidamping-like SOT induced signal in the experiments.

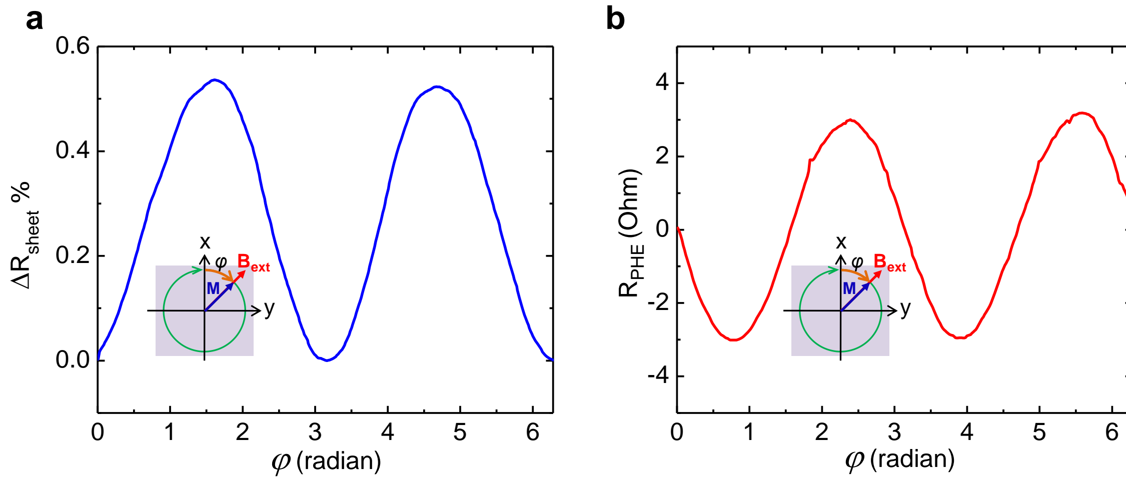

Figure 2-17. Rotation experiment to obtain the AMR and PHE resistances. **a**, The percentage change in the sheet resistance (see the text), $\Delta R_{\text{sheet}}\%$, as a function of the field azimuthal angle φ when the external magnetic field $\mathbf{B}_{\mathbf{ext}}$ rotates in the xy-plane, as shown in the inset. **b**, The transverse PHE resistance, R_{PHE}, as a function of the field azimuthal angle φ when the external magnetic field $\mathbf{B}_{\mathbf{ext}}$ rotates in the xy-plane, as shown in the inset. In the experiments, the $\mathbf{B}_{\mathbf{ext}}$ field magnitude is fixed at 2 T and the temperature is kept at 1.9 K. Figure is adapted with permission from ref. [57] (Y. Fan's publication).

Chapter 3

Electric-Field Control of Spin-Orbit Torque in a Magnetically Doped Topological Insulator

3.1 Overview

Electric-field control of magnetization dynamics is essential for realizing high-performance, low-power spintronic memory and logic devices. During recent years, enormous progress has been made in this regard. As listed in Fig. 3-1, the notable achievements are the electric-field control of ferromagnetism in magnetic semiconductors (*e.g.*, Mn-doped InAs, GaAs) through modulation of the carrier (hole) concentration [139-141], electric-field control of magnetization vector orientation through manipulation of the in-plane magnetic anisotropy [142], electric-field manipulation of magnetization direction and/or reversal by use of multiferroics [143-145], and significant voltage-controlled magnetic anisotropy change in ultrathin ferromagnet/oxide junctions (*e.g.*, Fe/MgO) [146,147]. On the other hand, for another method of manipulating magnetic moment---current-induced SOT [8,9,27], which is important in practical devices, the electric gate control is just beginning to be probed [148,149]. Thus, it becomes highly desirable to study the efficient electric-field control of SOT in novel magnetic structures, which may allow for the manipulation of magnetization in a fashion compatible with modern field-effect semiconductor devices. As elaborated in the last chapter, TI [54-56] -based magnetic structures have drawn much attention due to the giant spin-torque efficiency potentially applicable for spintronic devices [57,59,60]. Compared with conventional HMFHs where the SHE in the heavy metals and/or the Rashba-Edelstein effect at the interface are crucial for generating the spin torque [38,41,42,45,118], TIs

exhibit surface spin-momentum locked Dirac fermions [66,69,82,90,91,94-96] which are expected to be more efficient [127,150]. Indeed, as we have shown in the last chapter, the TI/Cr-doped TI bilayer heterostructure can produce a giant SOT which is almost three orders of magnitude larger than those reported in HMFHs [57]. Besides our work, current-induced SOT in TI/ferromagnet metal heterostructures has also been studied in several recent experiments [59,60]. Furthermore, related spin pumping/ISHE [61-65] and the spin-polarized tunneling spectroscopy [66] were also investigated in these structures.

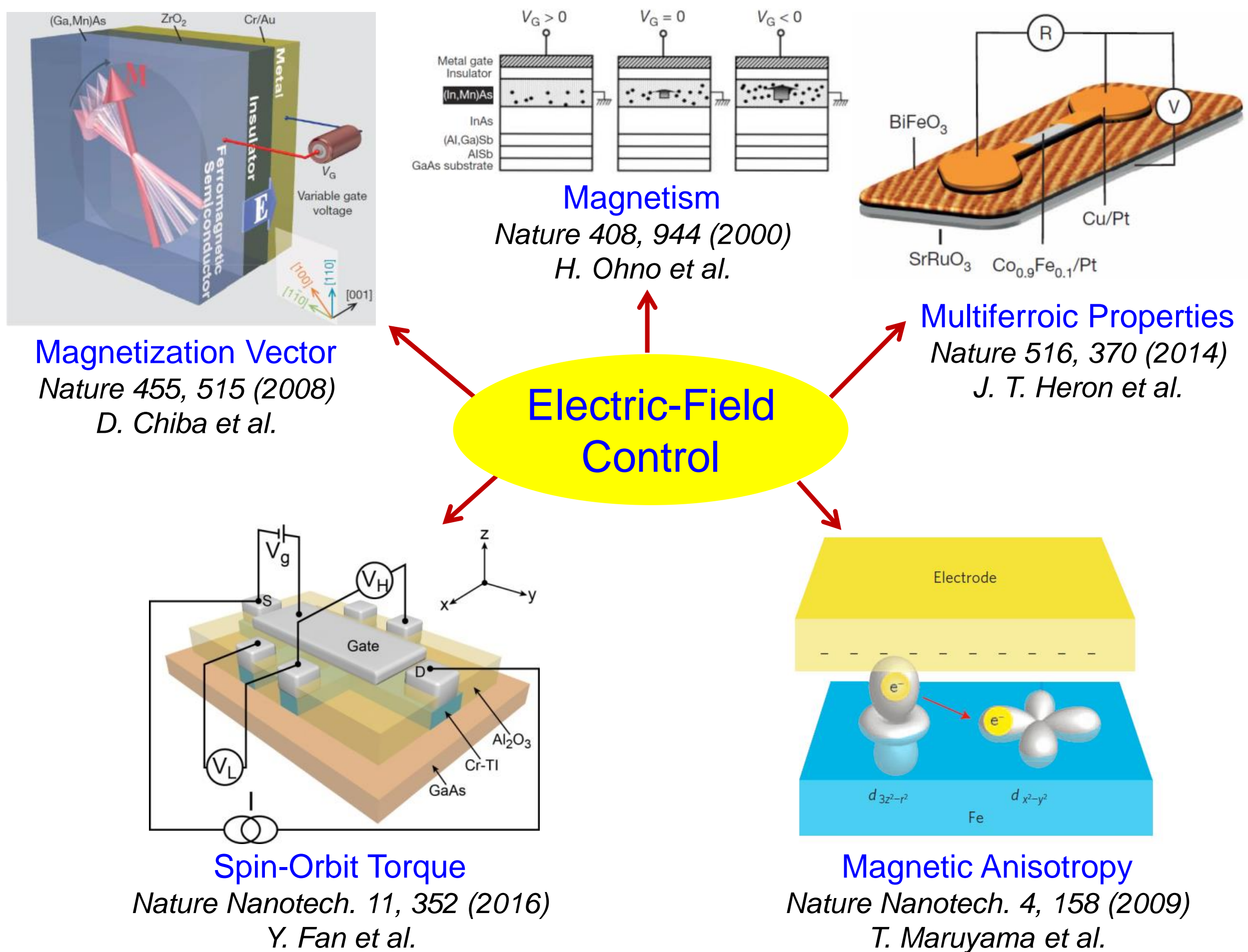

Figure 3-1. Various research topics in the field of electric-field control of magnetic properties in spintronics, including electric-field control of ferromagnetism, electric-field control of

magnetization vector orientation, electric-field control of multiferroic material properties, voltage-controlled interfacial magnetic anisotropy and electric-field control of spin-orbit torque.

Another important feature of TI is its bulk behavior as a semiconductor which allows effective electric-field manipulation of the surface carrier density and type [108,109,151], as opposed to heavy metals. Thus, the long-sought-after electric-field control of SOT may be potentially realized in TI-based magnetic structures. In this chapter, we will explore the gate electric-field control of SOT in the nominally uniformly Cr-doped TI (Cr-TI, for short) thin film in the Au(electrode)/Al_2O_3/Cr-TI/GaAs(substrate) structure [58]. Using the low-frequency harmonic method [9,57,116], we show that the SOT strength can be modulated by a factor of 4 by gate tuning within the accessible voltage range, which is almost two orders of magnitude larger than that reported in HMFHs [148]. The effective gate control, as discussed later in this chapter, also shows strong correlation with the net spin-polarized surface current originating from the topological surface states in the film. Furthermore, we demonstrate that the magnetization can be switched by scanning gate voltage with a constant current and an in-plane magnetic field applied in the Cr-doped TI film, pointing towards device applications such as electric-field controlled magnetic memory switch compatible with modern field-effect semiconductor technologies. Thus, the electric-field control is promising as another approach besides the lateral current to harness the giant SOT in the TI-based magnetic structures, which can potentially add new functionalities to spin-torque devices such as simultaneous memory and logic functions, and lead to ultralow power dissipation nonvolatile green electronics.

3.2 Magnetization Switching through Current-induced Spin-Orbit Torque in the Al_2O_3/Cr-doped TI/GaAs (substrate) Structure

Before introducing the top gate, we first briefly examine an Al_2O_3/Cr-TI/GaAs(substrate) structure to investigate the basic material properties and the intrinsic current-induced SOT. As shown in Fig. 3-2a, a 7 QL uniformly Cr-doped $Cr_{0.16}(Bi_{0.50}Sb_{0.42})_2Te_3$ thin film was epitaxially grown on an insulating GaAs (111)B substrate using MBE [109]. The blue arrows in Fig. 3-2a indicate the Cr dopant elements inside the TI matrix; the right panel of Fig. 3-2a shows the HRSTEM image of the Cr-doped TI film and the EDX mapping of the Cr dopant elements in the Cr-doped TI layer which are uniformly distributed [108,109]. The HRSTEM image demonstrates the nice crystallinity of the film and the atomically sharp interface between the Cr-doped TI layer and the substrate. As for the MBE growth, the semi-insulating ($\rho > 10^6$ Ω·cm) GaAs (111)B substrate has been cleaned by acetone with ultrasonic for 10 minutes before loaded to the MBE chamber. Then the atomically flat substrate was annealed to 580˚C and cooled down to growth temperature, under Se rich environment. After that, the Cr-doped TI film was grown using the similar procedure as employed in the Cr-doped TI layer preparation in the TI/Cr-doped TI bilayer heterostructure (see Chapter 2). The 2D growth mode was confirmed by the streaky RHEED patterns. After the Cr-doped TI film growth, a 1nm thick Al_2O_3 capping layer was immediately grown *in-situ* on top to protect the film [134]. Another layer of 19 nm thick high-k Al_2O_3 was deposited *ex-situ* on top by ALD at 200°C, which will serve as the dielectric layer in the afterward top-gate device (see Section 3.3). The thin film was patterned into micrometer scale Hall bar structures [134,151], as shown in Fig. 3-2b with illustrations of the Hall measurement set-up. In this Hall bar configuration, we define the current flowing from the left to the right (*i.e.*, along y–direction) as the positive current.

To examine the quality of the Cr-doped TI thin film, temperature-dependent longitudinal resistance R_{L} at zero magnetic field was measured and it shows monotonic decrease when increasing temperature from 1.9K to 300K, as plotted in Fig. 3-2c, which indicates the semiconducting feature of the film and suggests the Fermi level is located inside the bulk band gap [132]. Also shown in Fig. 3-2c is the coercive field B_{C} versus temperature, from which the Curie temperature T_{C} of the film is estimated to be around 11K where B_{C} almost vanishes.

It is known that in the uniformly Cr-doped TI film, ferromagnetism can be developed through bulk van-Vleck mechanism [108] and/or surface carrier mediated magnetism [108,109,130] at low temperature. To probe the magnetic properties, both the out-of-plane Hall resistance R_{H} and the longitudinal magneto-resistance R_{L} measured at 1.9K are plotted in Fig. 3-2d, as functions of the out-of-plane magnetic field. The nearly square-shape R_{H} hysteresis loop together with the butterfly-shape R_{L} demonstrate the pronounced magnetism [108,109] in the Cr-doped TI film with a magnetic easy axis along the out-of-plane direction (*i.e.*, along z-axis). Given the low Curie temperature of the film ($T_{\mathrm{C}} = 11\mathrm{K}$), in the following, all the transport experiments are performed at 1.9K unless otherwise stated.

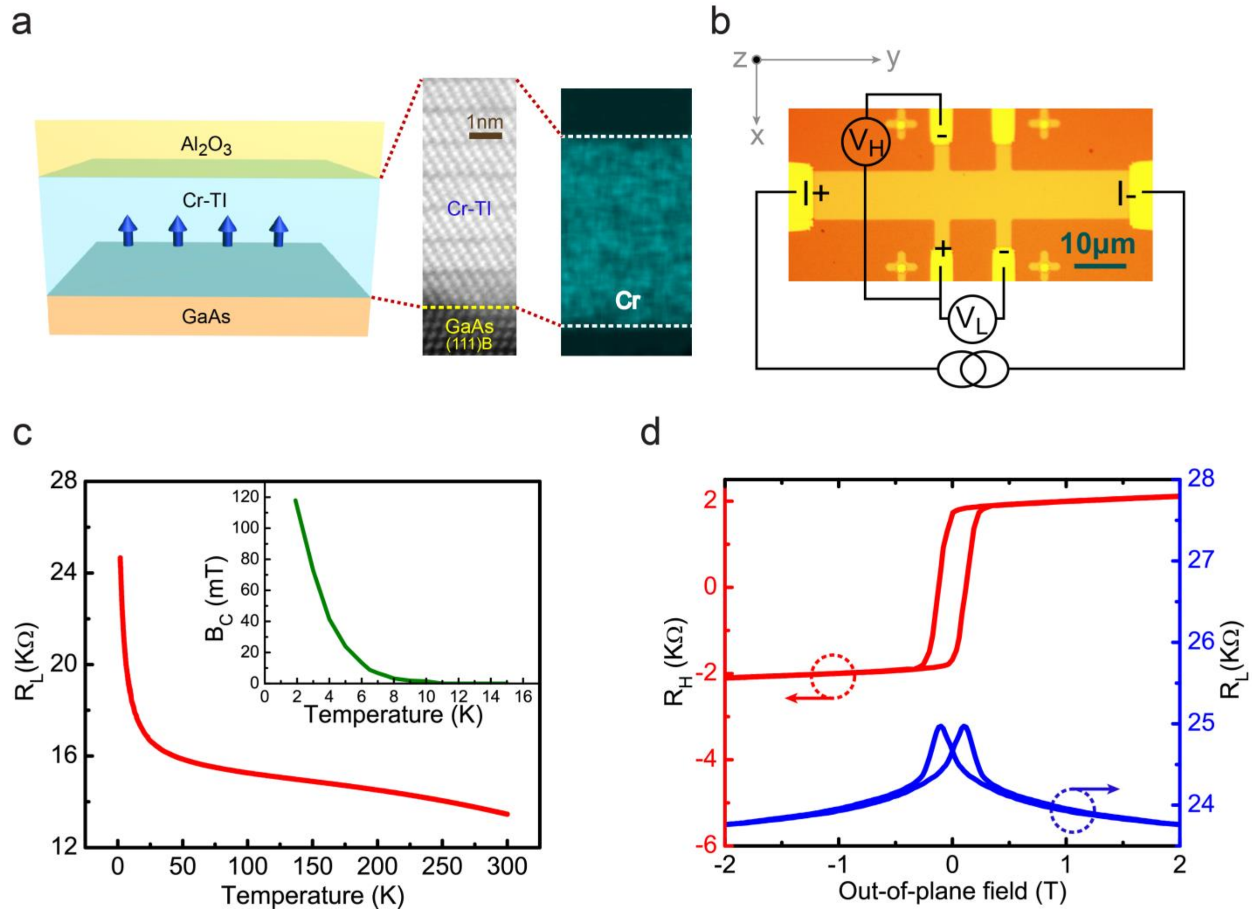

Figure 3-2. Material properties and measurement set-up of the Al_2O_3(20nm)/Cr-TI(7nm)/GaAs(substrate) structure device. **a**, 3D schematic of the Al_2O_3/Cr-TI/GaAs structure. The blue arrows denote the Cr dopants. Right: HRSTEM image of the Cr-doped TI film and EDX mapping of the Cr dopant elements inside the Cr-doped TI layer. **b**, microscopic image of the Hall bar device with illustrations of the Hall measurement set-up: current flowing from the left to the right (along y-direction) is defined as the positive current; V_{H} measures the Hall voltage and V_{L} measures the longitudinal voltage. The width of the Hall bar and the length between two neighboring Hall contacts are both 10 μm. **c**, Longitudinal resistance R_{L} versus temperature when the external magnetic field is set to 0T. Inset: the coercive field B_{C} as a function of temperature. **d**, Transverse Hall resistance R_{H} and longitudinal magneto-resistance

R_L as functions of the out-of-plane magnetic field measured at 1.9 K. Figures are adapted with permission from ref. [58] (Y. Fan's publication).

In this Al_2O_3/Cr-TI/GaAs structure, even though the uniform doping inside the Cr-doped TI layer respects the inversion symmetry along the z-direction, the structural asymmetry due to Al_2O_3 and GaAs can induce different interfacial properties with the Cr-doped TI layer, as illustrated in Fig. 3-4a, where the bottom surface states carrier density is estimated to be higher than that of the top surface states (more evidences are provided in Section 3.4 and Section 3.6). By passing a charge current through the Cr-doped TI layer, the spin-momentum locked surface states carriers on the two interfaces can produce non-equal amount of torques to the Cr dopant magnetization, and thus a non-zero net SOT is expected. In Fig. 3-4a, on top of the Al_2O_3/Cr-TI/GaAs structure we depict the total magnetization $\mathbf{M}$, the external magnetic field $\mathbf{B_{ext}}$ and various torques: $\boldsymbol{\tau}_{\mathbf{ext}}$ exerted by $\mathbf{B_{ext}}$, $\boldsymbol{\tau}_{\mathbf{K}}$ exerted by the perpendicular anisotropy field $\mathbf{B_K}$, and the net current-induced SOT, $\boldsymbol{\tau}_{\mathbf{SO}}$, for a DC current I_{dc} flowing along the $-y$ direction in the film. Here, $\mathbf{M}$ and $\mathbf{B_{ext}}$ are both in the yz-plane, with θ_{M} and θ_{B} being the respective polar angles relative to the z-axis; $\mathbf{B_K} = K\cos\theta_{\mathrm{M}}\hat{\mathbf{z}}$, and K is the out-of-plane anisotropy coefficient ($K = 0.6\mathrm{T}$ as determined from the fitting, see Fig. 3-3); $\boldsymbol{\tau}_{\mathbf{SO}} = -\gamma\mathbf{M} \times \mathbf{B_{SO}}$, where γ is the gyromagnetic ratio and $\mathbf{B_{SO}} = I_{\mathrm{dc}}\lambda_{\mathrm{SO}}\hat{\mathbf{x}} \times \mathbf{m}$ is the current-induced effective spin-orbit field [57]; λ_{SO} is the coefficient characterizing the SOC strength in the system and $\mathbf{m}$ is the unit vector denoting the magnetization direction. In this structure, $\boldsymbol{\tau}_{\mathbf{SO}}$ is the antidamping-like SOT which is the dominant term [57] and consistent with the bottom surface states spin-polarized current [66,69,82,90,91,94-96]. Thus, the equilibrium state of $\mathbf{M}$ can be achieved by balancing the torques: $\boldsymbol{\tau}_{\mathbf{ext}} + \boldsymbol{\tau}_{\mathbf{K}} + \boldsymbol{\tau}_{\mathbf{SO}} = 0$. In order to demonstrate the current-induced $\boldsymbol{\tau}_{\mathbf{SO}}$ in the structure, we carried

out the (B_y-fixed, I_{dc}-dependent) magnetization switching experiment. Indeed, the out-of-plane component of the magnetization, M_z (manifested by the AHE resistance R_{AHE}), can be successfully switched by scanning the DC current in the presence of the fixed in-plane magnetic fields $\mathbf{B}_y = B_y\hat{\mathbf{y}}$ with $B_y = \pm 2\text{T}$, as shown in Fig. 3-4c. The switching is hysteretic and agrees with the definitions of $\boldsymbol{\tau}_{\mathbf{SO}}$ and $\mathbf{B}_{\mathbf{SO}}$ in Fig. 3-4a. Furthermore, we also carried out the (I_{dc}-fixed, B_y-dependent) magnetization switching experiment. As shown in Fig. 3-4b, M_z can be successfully switched by sweeping the in-plane magnetic field in the presence of the fixed DC currents $I_{dc} = \pm 20\mu\text{A}$. The switching is also hysteretic and agrees with the definitions of $\boldsymbol{\tau}_{\mathbf{SO}}$ and $\mathbf{B}_{\mathbf{SO}}$. We summarize the switching behaviors as a phase diagram in Fig. 3-4d, from which we see that M_z can be switched using only tens of micro-amperes of DC current, indicating that even in this uniformly doped Al_2O_3/Cr-TI/GaAs structure, the current-induced SOT can be significant.

We furthermore carried out the low-frequency second harmonic experiment [9,57,116] to quantitatively measure the current-induced SOT. By sending an AC current into the Cr-TI layer, the current-induced alternating $\mathbf{B}_{\mathbf{SO}}$ field causes $\mathbf{M}$ to oscillate around its equilibrium position, which gives rise to the second harmonic AHE resistance, $R_{AHE}^{2\omega}$. In Fig. 3-4e, we plot the measured $R_{AHE}^{2\omega}$ as a function of the in-plane field B_y for input AC current with different root-mean-square (*rms*) values. The low frequency ω utilized is 15.8 Hz. In this case, the effective $\mathbf{B}_{\mathbf{SO}}$ field is pointing along $\hat{\mathbf{z}}$ or $-\hat{\mathbf{z}}$ direction, and for convenience we label it as $\mathbf{B}_{\mathbf{SO}} = B_{SO}\sin(\omega t)\,\hat{\mathbf{z}}$. In the large field region ($|B_y| \gg K$), as shown in Fig. 3-4e, $R_{AHE}^{2\omega}$ can be fitted using equation (2-5) [57], where the out-of-plane saturation AHE resistance R_A is determined to be 2.4 KΩ (see Section 3.3). In Fig. 3-4f, we plot the obtained effective spin-orbit field B_{SO} as a function of I_{ac} (*rms* value) for both the $B_y > 0$ and the $B_y < 0$ cases. The directions of the

obtained $\mathbf{B_{SO}}$ are consistent with the switching experiments and the effective field versus current ratio is $\frac{|B_{SO}|}{I_{ac}^{peak}} = 6.7$ mT/μA by linear fitting. If we tentatively assume the current distribution inside the Cr-doped TI layer is uniform, then the corresponding spin-torque ratio [9,38,57,59] can be estimated as, $\vartheta_{ST} = \frac{2eM_S B_{SO} w t_{Cr-TI}^2}{\hbar I_{ac}^{peak}} = 81$ (e is the electron charge, $\hbar$ is the reduced Planck constant, $M_S = 8.5\ \mathrm{emu/cm^3}$ is the magnetization magnitude, w and t_{Cr-TI} are the width and thickness of the Cr-doped TI layer), which again demonstrates that even in the uniformly doped Al_2O_3/Cr-TI/GaAs structure, due to the two non-balanced interfaces, the current-induced SOT can be large with the corresponding spin-torque efficiency much higher than that observed in HMFHs [9,116] (Note: a more accurate ϑ_{ST} will be provided by considering the more realistic current distribution inside the Cr-doped TI layer in Section 3.6). We summarize the SOTs evaluated from the TI/Cr-doped TI bilayer heterostructure (Chapter 2) [57] and the uniformly doped Al_2O_3/Cr-TI/GaAs structure [58] in Table 3-1. In the uniformly doped Al_2O_3/Cr-TI/GaAs structure, since the top surface spin-polarized current will compensate the bottom surface spin-polarized current when generating the SOT, the measured spin-torque ratio ϑ_{ST} is smaller than the one revealed in the TI/Cr-doped TI bilayer heterostructure [57].

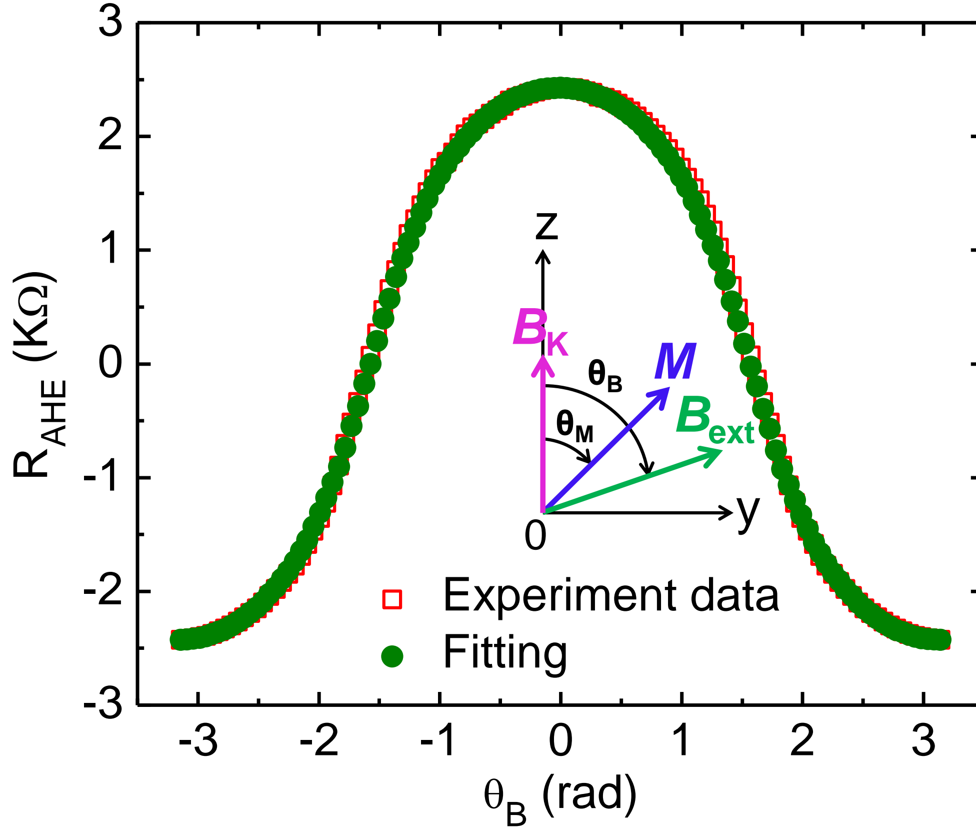

Figure 3-3. Determination of the out-of-plane anisotropy coefficient K and the saturation AHE resistance R_{AHE}. R_{AHE}, obtained from the rotation experiment (open squares) in the yz-plane and from the numerical fitting by solving equation (2-3) (solid circles), as functions of the field angle θ_{B}, respectively. In the fitting, we used $K = 0.6$T. Inset: the equilibrium orientation of the magnetization **M** in the presence of an external magnetic field $\mathbf{B_{ext}}$ with a constant magnitude of 2T. $\mathbf{B_K} = K\cos\theta_{\mathrm{M}}\hat{\boldsymbol{z}}$ is the perpendicular anisotropy field. θ_{M} and θ_{B} are the polar angles of **M** and $\mathbf{B_{ext}}$ from the z-axis, respectively. This experiment is performed at 1.9 K. Figure is adapted with permission from ref. [58] (Y. Fan's publication).

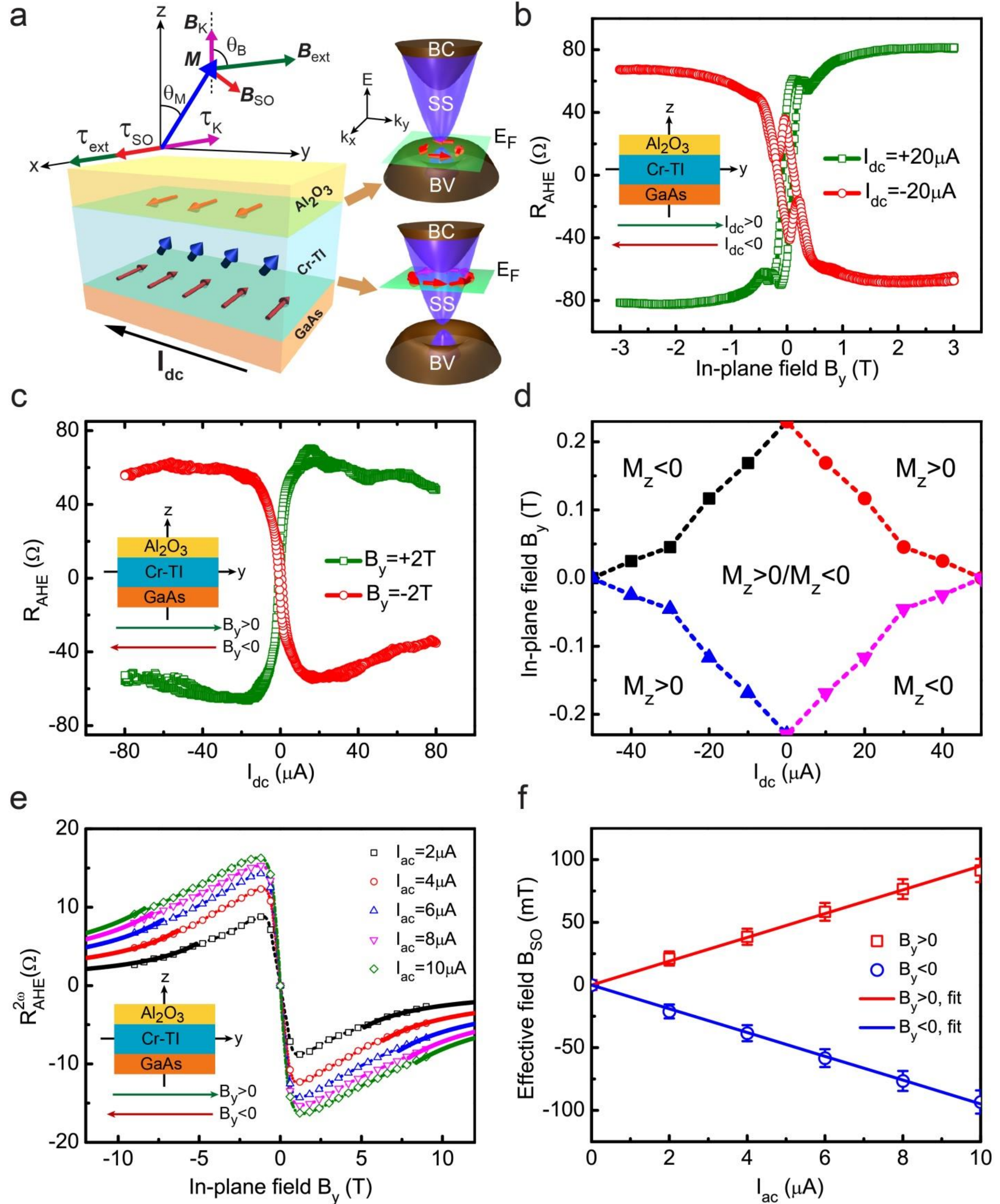

Figure 3-4. Current-induced magnetization switching and second harmonic measurements in the Al_2O_3(20nm)/Cr-TI(7nm)/GaAs(substrate) structure device. **a**, 3D schematic of the Al_2O_3/Cr-

TI/GaAs structure. Inside the Cr-doped TI layer, the blue arrows denote the Cr dopants and the red arrows indicate the spin directions of the conducting surface states (SS) carriers at the two interfaces when passing a negative DC current (*i.e.,* along $-y$ direction) through the film. Shown on top of the structure are the torques exerted by the external magnetic field $\mathbf{B_{ext}}$, the anisotropy field $\mathbf{B_K}$, and the net current-induced SOT $\boldsymbol{\tau_{SO}}$. $\mathbf{B_{ext}}$ and magnetization $\mathbf{M}$ are both in the yz-plane. Right: the top and bottom surface band structures. "BC", "BV" and "SS" stand for bulk conduction band, bulk valence band and surface states, respectively. E_F is the Fermi level. **b**, (I_{dc}-fixed, B_y-dependent) magnetization switching experiment. The AHE resistance is measured while sweeping B_y in the presence of a constant DC current with $I_{dc} = +20\mu A$ and $I_{dc} = -20\mu A$ along the Hall bar, respectively. **c**, (B_y-fixed, I_{dc}-dependent) magnetization switching experiment. The current-induced magnetization switching is measured in the presence of a constant in-plane magnetic field with $B_y = +2$ T and $B_y = -2$ T, respectively. **d**, Switching phase diagram of the magnetization in the presence of both B_y and I_{dc}. The dashed lines and symbols (extracted from experiments) denote the boundaries between different states. **e**, Second harmonic AHE resistance as a function of the in-plane magnetic field for AC current with different *rms* values. The frequency used is 15.8 Hz. Solid lines indicate the fittings proportional to $1/(|B_y| - K)$ in the large field regions. **f**, Effective spin-orbit field B_{SO} as a function of the AC current I_{ac} (*rms* value) for both the $B_y > 0$ and $B_y < 0$ cases as extracted from **e**. Straight lines are the linear fittings. Error bars represent standard errors. All the measurements are performed at 1.9K. Figures are adapted with permission from ref. [58] (Y. Fan's publication).

Table 3-1. Comparison of the SOTs in TI/Cr-doped TI bilayer and uniformly Cr-doped TI

Structures	**TI/Cr-doped TI,** ref. [57]	**Al_2O_3/Cr-doped TI/GaAs,** ref. [58]
Surface contribution to SOT	Bottom surface	Both top and bottom surfaces
Spin-torque ratio ϑ_{ST}	140~425 (at 1.9K)	81 (at 1.9K)

3.3 Electric-Field Effect on Material Properties of the Cr-doped Topological Insulator

The current-induced SOT arising from the non-balanced surface states carrier distributions at the two interfaces in the Al_2O_3/Cr-TI/GaAs structure inspires us to pursue the gate electric-field control of SOT since the gate can effectively tune the surface carrier density and type in the Cr-doped TI layer [108,109]. Following this idea, we deposited an Au electrode as a top gate on the Al_2O_3/Cr-TI/GaAs structure to form a gate controllable Hall bar device, as shown in Fig. 3-5a. A gate voltage of V_g can be applied between the top gate and the source contact. Before measuring the SOT under different V_g, we first examine the gate electric-field effect on the characteristics of the Cr-doped TI film. Figure 3-5b shows the longitudinal resistance R_{L} (at $B_{\mathrm{ext}} = 0\mathrm{T}$) and the effective Hall carrier density (sheet density, see Section 3.4), $c_{\mathrm{eff}} = 1/(e\alpha)$, as functions of V_g from -10V to +10V. Here, α is the out-of-plane ordinary Hall slope. Remarkably, the overall carrier type can be tuned from *p*-type to *n*-type, with c_{eff} changing from 6.2×10^{12} cm^{-2} to -3.5×10^{12} cm^{-2} ($-$ sign means *n*-type) when V_g scans from -10V to +10V, and near $V_g = +3\mathrm{V}$, R_{L} develops a peak while c_{eff} diverges. In the following, we analyze the carrier distributions and the transport process in more detail.

First, the ambipolar field effect (Fig. 3-5b) and R_{L} versus temperature behavior (Fig. 3-2c) observed in our Cr-doped TI film suggest that the Fermi level is located inside the bulk band gap. However, due to the Cr-doping [108,109], along with the presence of defects and random potential fluctuations [152] in the film, there are a considerable amount of hole carriers in the bulk, which makes the transport analysis quite difficult. Nevertheless, from the gate-controlled two surface Shubnikov-de Haas (SdH) quantum oscillations observed in a non-doped control sample (see Section 3.4), we learn that the top gate can majorly control the top surface carrier density in the Cr-doped TI film [108,109,153], while the bottom surface carrier density remains almost unchanged

through the whole voltage range with the Fermi level located in the surface states conduction band [153]. For convenience, in Fig. 3-5b we divide V_g from -10V to +10V into three regions: I, II and III. In region I, the top surface is biased to the *p*-type regime with c_{eff} changes by a rate of 9×10^{10}cm^{-2}/V and meanwhile R_{L} changes monotonically. The top surface accumulated hole mobility is $\mu_{\mathrm{h}} = 85$ cm^2/(V S) (see Section 3.4), and since the surface states Dirac point is located close to the bulk valence (BV) band edge [102,153,154] in the band structure, a large amount of these holes are ordinary. In region III, the top surface is biased to the surface states *n*-type regime and since c_{eff} almost reaches the linear region, the overall surface states electrons (from both top and bottom surfaces) dominate the transport. Considering both c_{eff} and R_{L}, the surface states Dirac electron mobility can be estimated as $\mu_{\mathrm{D}} = 100$ cm^2/(V S). In the intriguing region II, R_{L} reaches a peak at around $V_g = +3$V which means the top surface carriers are mostly depleted, and at the same time c_{eff} diverges. Solving the equations set by the divergence of c_{eff} and the maximum of R_{L} (see Section 3.4), we find that the bottom surface states electron density is $n_{\mathrm{SS,b}} = 1.02 \times 10^{12}$cm^{-2} and the bulk hole density (sheet density) is $p_{\mathrm{bulk}} = 1.4 \times 10^{12}$ cm^{-2} at $V_g = +3$V.

Due to the randomness of defects and potential fluctuations in the Cr-doped TI film [152], the bulk carriers are assumed to be uniformly distributed inside the bulk and consequently cannot produce much SOT when passing a charge current through the film. As a result, we will focus mainly on the carriers at the two surfaces which are the dominant origins of the current-induced SOT. In Fig. 3-5c, we depict both the top and bottom surface band structures for the corresponding three regions: I, II and III. While the bottom surface Fermi level E_F always remains inside the surface states conduction band, the top surface Fermi level E_F can be tuned near the bulk valence band edge (region I), across the surface gap near the Dirac point (region II),

and into the surface states conduction band (region III). In region III, the top surface states electron density $n_{\mathrm{SS,t}}$ is estimated to be smaller than the bottom surface states electron density $n_{\mathrm{SS,b}}$ (more evidences can be found in Section 3.6).

In addition, the out-of-plane anisotropy coefficient K and the saturation AHE resistance R_{A} of the Cr-doped TI film can also be significantly modified by V_g. Figure 3-5d shows K and R_{A} as functions of V_g from -10V to +10V. It should be noted that the R_{A} versus V_g curve shows a similar shape to the R_{L} versus V_g curve as displayed in Fig. 3-5b, which is in accordance with the intrinsic correlation between R_{A} and R_{L} due to different scattering mechanisms [34]. Equally important, the anisotropy coefficient K shows almost a monotonic decrease as V_g tunes the top surface carriers from holes to electrons, and the K value is modulated from 719.5 mT ($V_g = -10$V) to 471.2 mT ($V_g = +6$V), which has changed by 35% and suggests that electric field can have a crucial modulation of the magnetism in the Cr-doped TI film [108,109,130,155].

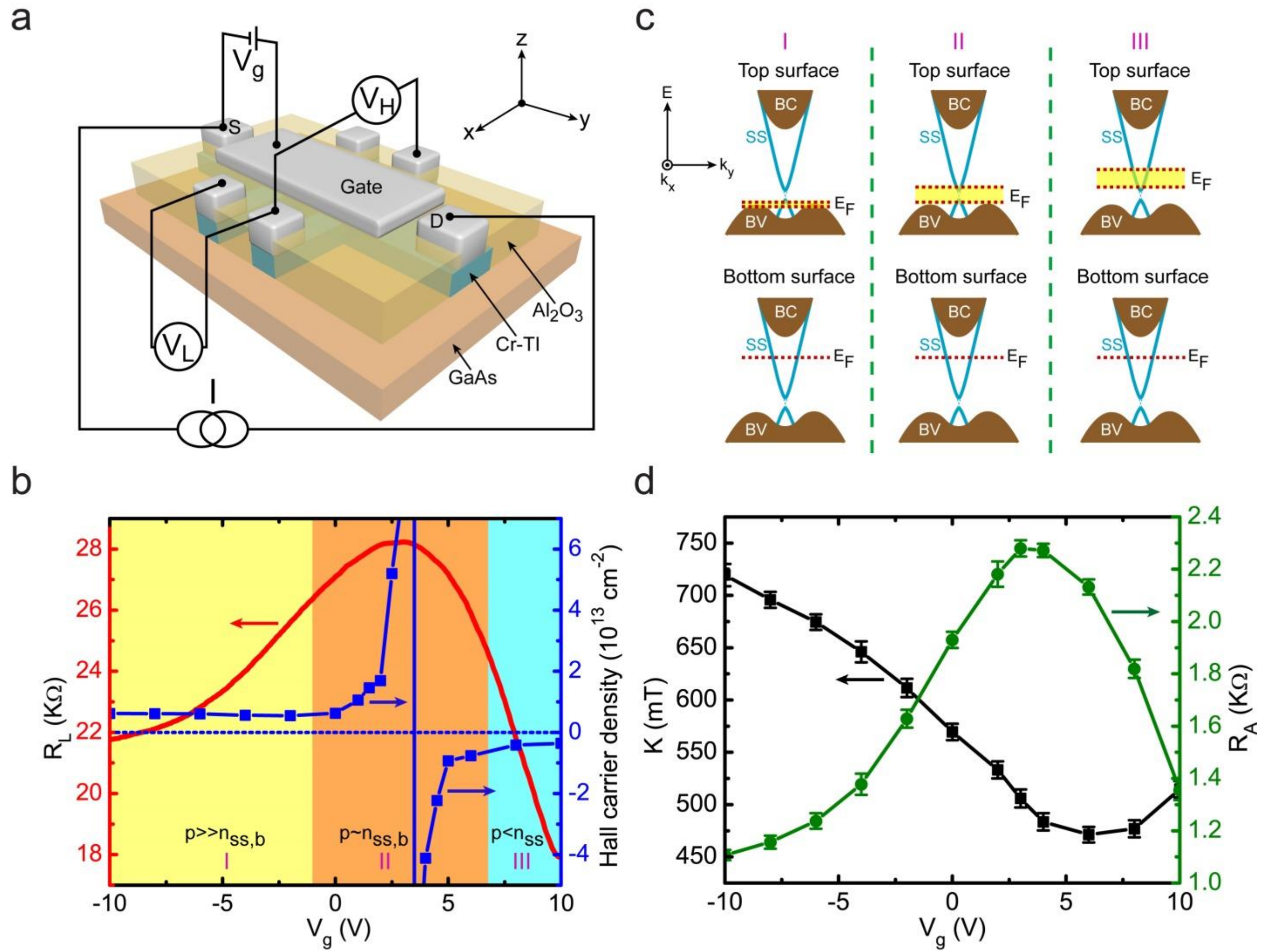

Figure 3-5. Top-gate Hall bar configuration and gate electric-field effect on material properties in the Au(electrode)/Al_2O_3(20nm)/Cr-TI(7nm)/GaAs(substrate) structure device. **a**, 3D schematic of the Hall bar structure made from the Al_2O_3(20nm)/Cr-TI(7nm)/GaAs(substrate) stack with a top Au gate electrode (light gray). Standard four-point measurement setup is displayed. A gate voltage of V_g can be applied between the top gate and the source contact. **b**, Longitudinal resistance R_{L} and effective Hall carrier density (sheet density) as functions of V_g. Colored area I, II and III show the different gate voltage regions. $p,\ n_{\mathrm{SS}}$ and $n_{\mathrm{SS,b}}$ represent the overall hole density, the overall surface states electron density and the bottom surface states

electron density in the film, respectively. **c**, The top and bottom surface band structure configurations for the three gate voltage regions shown in **b**. Yellow colored area in the top surface band structure shows the tune range of the top surface Fermi level E_F within the corresponding gate voltage region. **d**, Out-of-plane anisotropy coefficient K and out-of-plane saturation AHE resistance R_{A} as functions of V_g. Error bars represent standard errors. All the measurements are performed at 1.9K. Figures are adapted with permission from ref. [58] (Y. Fan's publication).

Besides the anisotropy coefficient K and the saturation AHE resistance R_{A} , the magnetization magnitude M_{S} also varies with V_g . In order to estimate the magnetization magnitude M_{S} under different gate voltages V_g, we first measured the Curie temperature T_{C} of the Cr-doped TI film in the Au(electrode)/Al_2O_3/Cr-TI/GaAs structure under different gate voltages V_g using the same method as discussed in Section 3.2 (Fig. 3-2c). T_{C} shows a monotonic decrease as V_g increases from -10V to +10V, as displayed in Fig. 3-6a, which is consistent with our previous studies [108,109] and in accordance with the out-of-plane anisotropy coefficient change with respect to V_g (Fig. 3-5d). Meanwhile, within the accessibility of our SQUID measurement system, we carried out the magnetization versus magnetic field measurement at 5K, 8K, 10K and 11K when no gate voltage was applied on the sample. The magnetization magnitude M_{S} can be obtained after subtracting the linear background at large field, and the results are plotted in Fig. 3-6b as the solid squares. It can be seen that M_{S} is almost 0 at $T = 11\mathrm{K}$, consistent with the Curie temperature at $V_g = 0\mathrm{V}$ (Fig. 3-6a). Furthermore, it is known that the $M_{\mathrm{S}} - T$ relation follows the power law [156] $M_{\mathrm{S}} = M_0(1 - \frac{T}{T_{\mathrm{C}}})^{\beta}$ in near the Curie temperature region. Subsequently, we

carried out the fitting using the measured data, as shown by the purple curve ($V_g = 0$V) in Fig. 3-6b, and find $M_0 = 9.6$ emu/cm^3, $\beta = 0.6$. After that, we use the same power law formula but different T_C values as presented in Fig. 3-6a to estimate the $M_\mathrm{S} - T$ relation under various gate voltages. The obtained results are plotted in Fig. 3-6b. It can be seen that at $T = 1.9$K, which is the experimental temperature we mostly used, the magnetization magnitude M_S does not change much. In Fig. 3-6c, we plot the M_S, obtained from the fittings in Fig. 3-6b, versus the gate voltage V_g for $T = 1.9$K. We can observe that M_S changes from 8.6 emu/cm^3 ($V_g = -10$V) to 8.3 emu/cm^3 ($V_g = +10$V), which is modulated by less than 5% and indicates that the change in magnetization magnitude M_S is almost negligible in the gate-controlled experiments that we have carried out.

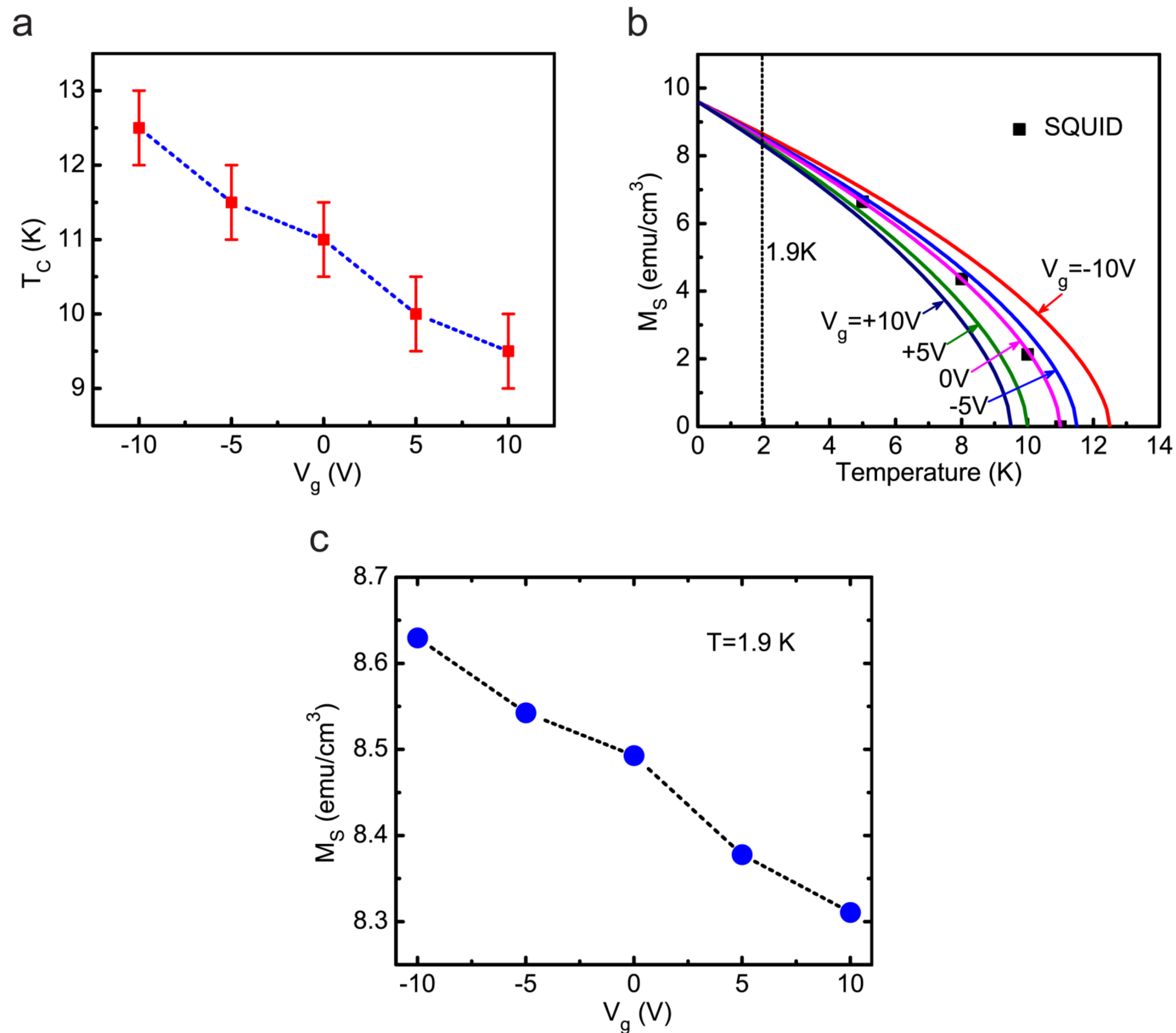

Figure 3-6. Curie temperature T_{C} as a function of gate voltage V_g in the Au(electrode)/Al_2O_3/Cr-TI/GaAs structure. **b**, Solid squares represent the magnetization magnitude M_{S} measured from SQUID at different temperatures when no gate voltage is applied. Different curves show the theoretical fittings of the $M_{\mathrm{S}} - T$ relation under different gate voltages. Dashed line denotes $T = 1.9$ K. **c**, Magnetization magnitude M_{S} obtained from the fitting for $T = 1.9$ K as a function of the gate voltage V_g. Figures are adapted with permission from ref. [58] (Y. Fan's publication).

3.4 Estimation of the Two Surfaces' Carrier Densities and Mobilities in the Cr-doped TI Film under Different Gate Voltages

In this section, we analyze in detail the carrier densities and mobilities of the two surfaces in the Cr-doped TI film under different gate voltages. The best method to evaluate the top surface and the bottom surface carrier densities under different V_g is to study the quantum oscillations (*e.g.*, SdH oscillations) [132,153,157-159] from these surface carriers when an out-of-plane magnetic field is applied. However, in the Cr-doped TI materials, since the carrier mobility is normally very low, as shown in Fig. 3-8, the relevant quantum oscillations are very difficult to observe. Alternatively, we have grown a 10 QL un-doped $(Bi_{0.53}Sb_{0.47})_2Te_3$ thin film which has a similar Bi : Sb ratio to the Cr-doped TI film as used in Section 3.3, and made it into a gate controllable Hall bar device following the same fabrication procedure. This un-doped TI thin film has a high carrier mobility (up to 3100 $cm^2/(V \cdot s)$ at 0.3K) [153], and the SdH oscillations from the two surface carriers can be successfully observed at low temperature. In Fig. 3-7a, we show the second derivative of the longitudinal resistance, d^2R_{L}/dB^2, as a function of both the inverse of the magnetic field, $1/B$, and the gate voltage V_g at 0.3 K. Intriguingly, we notice that there are V_g-dependent peaks as accentuated by the white dashed lines. These peaks originate from the formation of Landau levels of Dirac fermions on the top surface of the TI film, and the gate-dependent shift of the peaks is due to the modulation of the top surface carrier density as V_g is scanned from +2V to +11V. At the same time, there are other V_g-independent peaks at high magnetic field, as indicated by the black dashed lines. These peaks are attributed to the formation of Landau levels of the bottom surface Dirac fermions. It is noted that the bottom surface SdH oscillation frequency remains almost constant within the whole gate voltage range ($-11\mathrm{V} \leq V_g \leq +11\mathrm{V}$), indicating little or almost no change of the bottom surface carrier density

presumably due to the screening effect of the top surface carriers and the high dielectric constant (ε_r ~ 75) of TI materials [102,154].

The surface Dirac fermions feature can be confirmed from the Landau fan diagram (Fig. 3-7b) and the quadratic relationship between the Fermi level E_{F} and the surface carrier density n_{2D} (Fig. 3-7c). The Landau fan diagram for various gate voltage values is plotted in Fig. 3-7b, where the $1/B$ values corresponding to the peaks in Fig. 3-7a are plotted as a function of the Landau level index [132,153,157-159]. The solid symbols represent the top surface Dirac fermions, demonstrating a systematic shift depending on the gate bias. The open symbols represent the bottom surface Dirac fermions, which show almost no dependence on the gate bias. It is known that in the SdH oscillations, the Landau level index n is related to the cross section area of the Fermi surface (S_{F}) by $2\pi(n+\gamma) = \hbar S_{\mathrm{F}}/(eB)$, where e is the electron charge, $\hbar$ is the reduced Plank constant, B is the magnetic flux density, and $\gamma = 1/2$ or 0 represents the Berry phase of π or 0 [132,153,157-159]. Linear fits yield intercepts at the abscissa of 0.51 ± 0.04, as shown in Fig. 3-7b, confirming the presence of surface massless Dirac fermions carrying a π Berry phase. From the Landau fan diagram and the E-K dispersion relation from the ARPES results [153], the surface Fermi level E_{F} and the surface carrier density n_{2D} can be estimated. Figure 3-7c displays the Fermi level E_{F} as a function of the surface carrier density n_{2D}. The n_{top} can be effectively tuned from 1.1×10^{12} cm^{-2} to 1.6×10^{12} cm^{-2} by scanning the gate voltage from +2V to +11V, while the n_{bottom} remains the same at 5.7×10^{12} cm^{-2} for all the gate voltages. A quadratic relationship of $E_{\mathrm{F}} \propto n^{1/2}$ can be fitted, as shown by the red curve in Fig. 3-7c, confirming the linear E-K relationship of the surface Dirac cone.

In this non-doped TI Hall bar structure, the SdH oscillation frequency changes with respect to the gate voltage V_g, as shown in Fig. 3-7a, which demonstrates that the SdH oscillations are

from the surface Dirac electrons (not holes). At $V_g = 0\mathrm{V}$, the top surface SdH oscillation spectrum almost disappears, suggesting that the top surface Fermi level almost reaches the Dirac point at $V_g = 0\mathrm{V}$. It is also found that at $V_g = 0\mathrm{V}$ the whole film is at near the neutral state [153]. When $V_g < 0\mathrm{V}$, as shown in Fig. 3-7a, the top surface SdH oscillation spectrum completely disappears while the bottom surface one still persists, indicating the accumulation of a large amount of ordinary holes on the top surface which reduce the overall carrier mobility [153]. When $0\mathrm{V} < V_g < 11\mathrm{V}$, the top surface has Dirac electrons but the density is always smaller than that of the bottom surface, as shown in Fig. 3-7c, which is probably due to the different interfacial properties (*e.g.*, different band bending) [160] at the two surfaces of the TI film.

Now we will estimate the carrier densities and mobilities on the top surface and bottom surface of the Cr-doped TI film in the Au(electrode)/Al_2O_3/Cr-TI/GaAs structure under different gate voltages. Compared with the un-doped TI film where the bulk is mostly insulating [102,153,154], the Cr dopants can induce hole carriers throughout the Cr-TI film and make the bulk non-insulating [108,109], as evidenced by the effective Hall carrier density c_{eff} at $V_g = 0\mathrm{V}$ in Fig. 3-5b in Section 3.3. Considering the value of c_{eff} at $V_g = 0\mathrm{V}$ and the uniform Cr-doping profile in the Cr-doped TI film, it is reasonable to think that there are a considerable amount of topological surface states electrons on the bottom surface of the Cr-doped TI film which are immune to the top gate voltage V_g, similar to the non-doped TI film as discussed above. In Section 3.3, the effective Hall carrier density c_{eff} (sheet density) is defined as, $c_{\mathrm{eff}} = 1/(e\alpha)$, where α is the out-of-plane ordinary Hall slope. Generally, when there are both electrons and holes in a semiconducting film, the effective Hall carrier density can be derived as $c_{\mathrm{eff}} = \frac{(p\mu_{\mathrm{h}}+n\mu_{\mathrm{e}})^2}{p\mu_{\mathrm{h}}^2-n\mu_{\mathrm{e}}^2}$, where

p is the hole density (sheet density), n is the electron density (sheet density), μ_{h} is the hole mobility and μ_{e} is the electron mobility.

When the Cr-doped TI film is biased to the *p*-type regime, as shown in Fig. 3-5b region I in Section 3.3, c_{eff} changes almost linearly with V_g. In this regime, the top gate can most effectively control the top surface accumulated hole density because of the screening effect characterized by the small Debye length [109]. In this case, $\frac{dp_{\mathrm{top}}}{dV_g} \cong \frac{dp}{dV_g} \cong \frac{dc_{\mathrm{eff}}}{dV_g} = 9 \times 10^{10}$ cm^{-2}/V, where p_{top} is the top surface accumulated hole density. In this region, the longitudinal sheet conductance of the Cr-doped TI film, $G_{\mathrm{S}} = 1/R_{\mathrm{S}}$ (R_{S} is the longitudinal sheet resistance), also changes linearly, as shown in Fig. 3-8a. Consequently, the top surface accumulated hole mobility can be derived as $\mu_{\mathrm{h}} = \frac{dG_{\mathrm{S}}}{dV_g} / (e \frac{dp_{\mathrm{top}}}{dV_g}) = 85$ cm^2/(V s). When the Cr-doped TI film is biased to the *n*-type regime, as shown in Fig. 3-5b region III in Section 3.3, c_{eff} almost reaches the linear region and the overall topological surface states electrons (from both top and bottom surfaces) dominate the transport. Using similar argument by considering both c_{eff} and R_{S}, the topological surface states Dirac electron mobility can be estimated as $\mu_{\mathrm{D}} = 100$ cm^2/(V s). When the Cr-doped TI film is biased to region II in Fig. 3-5b in Section 3.3, R_{L} reaches a peak at $V_g = +3$V which means the top surface carriers are mostly depleted, and meanwhile $c_{\mathrm{eff}} = \frac{(p_{\mathrm{bulk}}\mu_{\mathrm{h}} + n_{\mathrm{SS,b}}\mu_{\mathrm{D}})^2}{p_{\mathrm{bulk}}\mu_{\mathrm{h}}^2 - n_{\mathrm{SS,b}}\mu_{\mathrm{D}}^2}$ diverges. Here, p_{bulk} is the bulk ordinary hole density (sheet density) and $n_{\mathrm{SS,b}}$ is the bottom topological surface states electron density. By combining $p_{\mathrm{bulk}}\mu_{\mathrm{h}}^2 - n_{\mathrm{SS,b}}\mu_{\mathrm{D}}^2 = 0$ and $e(p_{\mathrm{bulk}}\mu_{\mathrm{h}} + n_{\mathrm{SS,b}}\mu_{\mathrm{D}}) = 1/R_{\mathrm{S,peak}}$, we find that $n_{\mathrm{SS,b}} = 1.02 \times 10^{12}$cm^{-2} and $p_{\mathrm{bulk}} = 1.4 \times 10^{12}$ cm^{-2}. Here, $R_{\mathrm{S,peak}}$ is the sheet resistance at $V_g = +3$V and in our device geometry, $R_{\mathrm{S,peak}} = R_{\mathrm{L}}(V_g = +3\mathrm{V})$. Based on the simple capacitor model and the carrier-attracting rate (9×10^{10} cm^{-2}/V) by the top gate,

the top surface carrier density under different gate voltages V_g can be obtained, as plotted in the upper panel of Fig. 3-10 in Section 3.6. We find that the bottom topological surface states electron density $n_{\mathrm{SS,b}}$ is always larger than the top topological surface states electron density $n_{\mathrm{SS,t}}$ in the whole n-type regime, which is consistent with the two surface carrier distributions in the non-doped TI film under different gate voltages as discussed above.

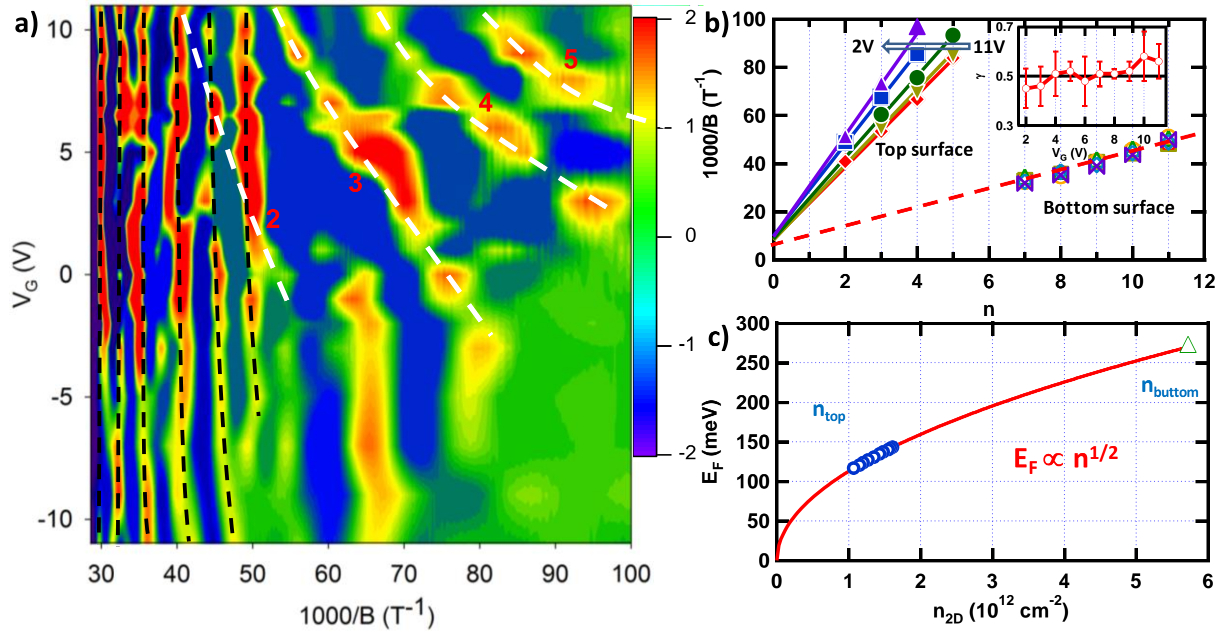

Figure 3-7. SdH quantum oscillations from the top and bottom surface states in the $(Bi_{0.53}Sb_{0.47})_2Te_3$ thin film. (**a**) d^2R_{L}/dB^2 as a function of $1/B$ and V_g. Both gate dependent and independent peaks are observed. The peaks which change with V_g originate from the formation of Landau levels of Dirac fermions on the top surface (white dashed lines, Landau levels 2 to 5 are marked). The V_g-independent peaks come from the formation of Landau levels of the bottom surface Dirac fermions (black dashed lines). (**b**) Landau fan diagram of the peaks. The peaks of the top surface Landau levels (solid symbols) show systematic change depending on the gate voltage, while those of the bottom surface Landau levels are almost constant. Inset: The

intercept γ as a function of the gate voltage. The black line indicates $\gamma = 0.5$. (**c**) The carrier density of the top (circles) and bottom (triangle) surface states as a function of Fermi level E_F extracted from the corresponding SdH oscillations for various gate voltages. A quadratic relationship is shown. The measurement was carried out at 0.3K. This figure is adapted with permission from ref. [153] (Y. Fan's publication).

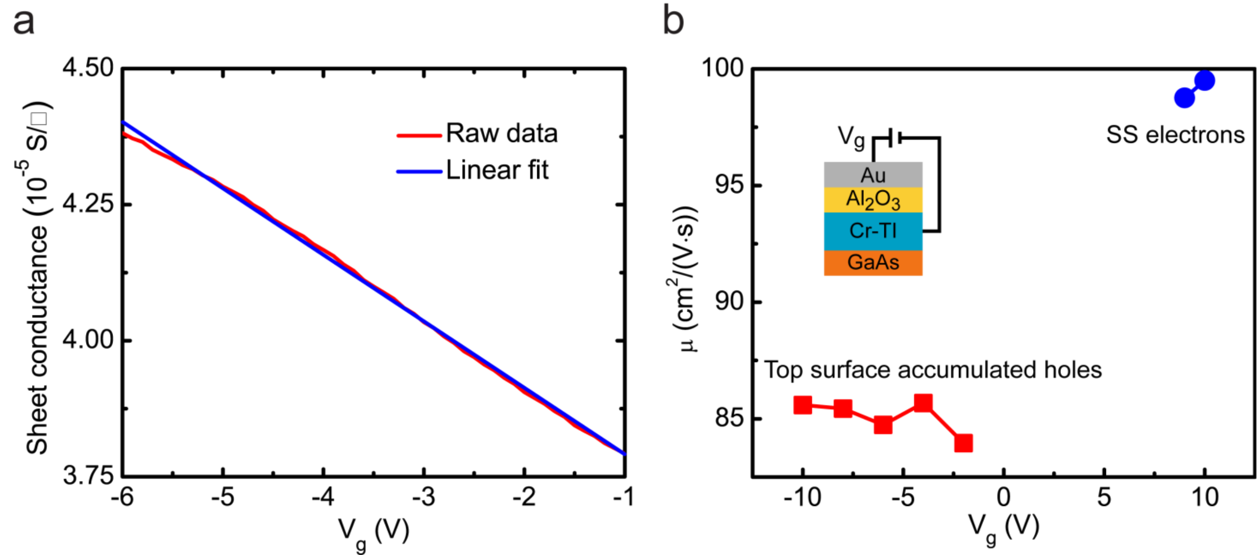

Figure 3-8. Longitudinal sheet conductance and surface carrier mobility in the Cr-doped TI film under different gate voltages. **a**, The longitudinal sheet conductance G_S as a function of the gate voltage V_g in the *p*-type regime in the Au(electrode)/Al_2O_3/Cr-TI/GaAs Hall bar structure. **b**, The extracted surface carrier mobilities as functions of the gate voltage V_g in both *p* and *n*-type regimes in the Au(electrode)/Al_2O_3/Cr-TI/GaAs Hall bar structure. The transport experiments were performed at 1.9K. Inset: schematic of the structure and the applied gate voltage. Figures are adapted with permission from ref. [58] (Y. Fan's publication).

3.5 Electric-Field Control of Spin-Orbit Torque and Magnetization Switching Behaviors in the Au(electrode)/Al_2O_3/Cr-TI/GaAs (substrate) Structure

Based on the above results, we carried out the second harmonic experiment to probe the effective spin-orbit field B_{SO} under different V_g. In Fig. 3-9a, we present $R_{AHE}^{2\omega}$ as a function of B_y for different V_g from -10V to +10V. The AC current applied is 4μA (*rms* value) and the low frequency used is 15.8Hz. The solid lines represent the fittings proportional to $1/(|B_y| - K)$ in the large field region according to equation (2-5). In Fig. 3-9b, we plot the obtained B_{SO} versus V_g for the $B_y > 0$ case. Remarkably, B_{SO} can be tuned from 19.8 mT ($V_g = -10\text{V}$) up to 79.5 mT ($V_g = +3\text{V}$), reflecting a factor of 4 in modulation which is almost two orders of magnitude larger than that reported in the gate-controlled HMFHs [148]. B_{SO} is peaked at around $V_g = +3\text{V}$, which corresponds to the situation when the top surface of the Cr-doped TI film is most insulating (neutral point) and the spin-polarized current mainly flows through the bottom surface states [82,90,91,94,95] and consequently produces the largest SOT. When $V_g > +3\text{V}$, *e.g.*, the Cr-doped TI film enters region III as shown in Fig. 3-5b, the top surface can also have spin-momentum locked surface states electrons which will share the current flowing through the film. However, these top surface states electrons will generate opposite SOT compared to the bottom surface states electrons due to the different spin-momentum locking direction with respect to the bottom surface normal vector [82,90,91,94,95]. On the other hand, when $V_g < +3\text{V}$, *e.g.*, the Cr-TI film enters region I as shown in Fig. 3-5b, the accumulated holes on the top surface will also share the current flowing through the film. But a large amount of these holes are ordinary and they cannot generate much SOT. The rest amount of holes are Dirac-like and similarly will generate opposite SOT compared to the bottom surface states electrons. In both cases (V_g gets

larger or smaller from +3V), the overall current-induced SOT in the film decreases as evidenced in Fig. 3-9b. It is noted that the SOT does not change sign in the whole region from -10V to +10V, indicating that the bottom surface states electrons always dominate in generating the SOT. Combined with the modulation of magnetization magnitude M_S by V_g (see Section 3.3), the SOT strength can vary from $7.4 \times 10^{11}(\frac{\hbar}{2e})$ A cm^{-3} (at $V_g = -10\text{V}$) to $2.87 \times 10^{12}(\frac{\hbar}{2e})$ A cm^{-3} (at $V_g = +3\text{V}$) within the accessible voltage range, which demonstrates the effective gate electric-field control of SOT (by a factor of 4) in the Au(electrode)/Al_2O_3/Cr-TI/GaAs structure.

For potential applications, we further investigated the gate electric-field effect on the magnetization switching behaviors of the Cr-doped TI film in the presence of both the in-plane field B_y and the longitudinal DC current I_{dc}. Intriguingly, the switching behaviors can be significantly modified by V_g in both the (I_{dc}-fixed, B_y-dependent) and the (B_y-fixed, I_{dc}-dependent) magnetization switching experiments. For example, in Fig. 3-9c, we summarize the switching phase diagrams under $V_g = -10\text{V}, +1.5\text{V}, +10\text{V}$, respectively. It can be seen that the switching phase diagram has been changed dramatically by the gate voltage and the switching boundaries shrink towards the central region for $V_g = +1.5\text{V}$ compared with the other two cases ($V_g = -10\text{V}, +10\text{V}$), indicating a smaller longitudinal I_{dc} is required for switching for $V_g = +1.5\text{V}$ in the presence of a fixed in-plane B_y. In fact, this is expected because the current-induced SOT efficiency is higher for $V_g = +1.5\text{V}$ than the other two cases ($V_g = -10\text{V},\ +10\text{V}$). Furthermore, we carried out the (I_{dc}-fixed, B_y-fixed, V_g-dependent) experiments to study the direct manipulation of magnetization by scanning V_g. The initial magnetization state can be prepared to be $M_z < 0$ for X: ($I_{\text{dc}} = 20\mu\text{A},\ B_y = 0.1\text{T}$) and $M_z > 0$ for Y: ($I_{\text{dc}} = 20\mu\text{A},\ B_y = -0.1\text{T}$) under $V_g = -10\text{V}$, as shown in Fig. 3-9c. After that, both I_{dc} and B_y are fixed and we

scan V_g from -10V to +3V while the AHE resistance R_{AHE} is simultaneously measured. The obtained results are plotted in Fig. 3-9d, and it can be clearly seen that the magnetization state is switched from $M_z < 0$ to $M_z > 0$ for X: ($I_{\mathrm{dc}} = 20\mu\mathrm{A},\ B_y = 0.1\mathrm{T}$) and from $M_z > 0$ to $M_z < 0$ for Y: ($I_{\mathrm{dc}} = 20\mu\mathrm{A},\ B_y = -0.1\mathrm{T}$) by scanning V_g from -10V to +3V, successively. The final magnetization states are consistent with the deterministic states for X and Y under $V_g = +3\mathrm{V}$, respectively, as shown in Fig. 3-9c. Consequently, the switching induced by scanning V_g in the presence of fixed I_{dc} and B_y demonstrates that the gate electric-field control of SOT can provide an effective way to determine and manipulate the magnetization state in the Cr-doped TI film.

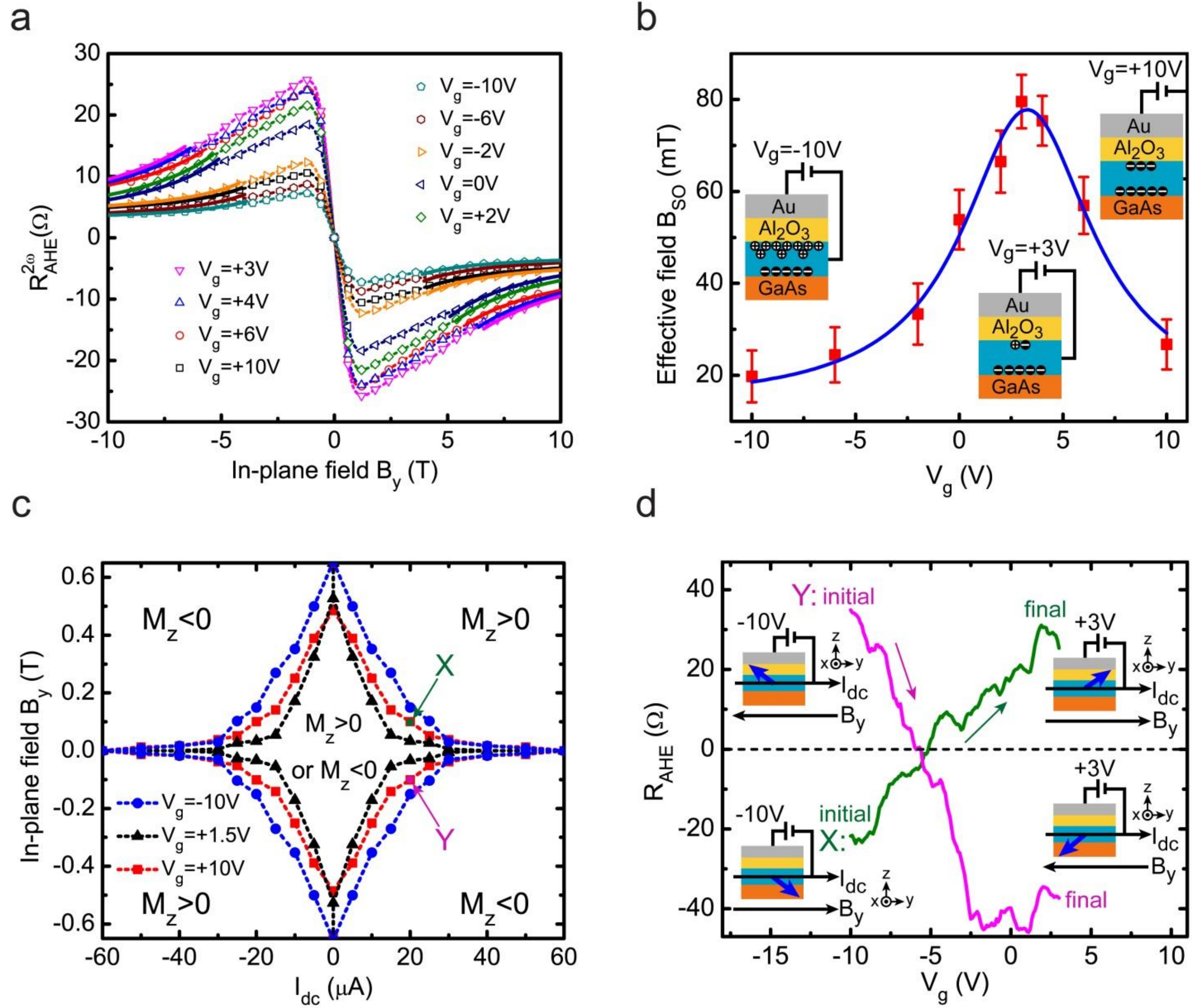

Figure 3-9. Second harmonic measurements under different gate voltages and voltage-induced magnetization switching behaviors. **a**, Second harmonic AHE resistance as a function of the in-plane magnetic field under different V_g from -10V to +10V. The AC current applied is 4μA (*rms* value) and the frequency used is 15.8 Hz. Solid lines represent the fittings proportional to $1/(|B_y| - K)$ in the large field regions. **b**, Effective spin-orbit field B_{SO} as a function of V_g for the $B_y > 0$ case as extracted from figure **a**. Error bars represent standard errors and blue curve shows the Lorentz fitting. Insets show the schemes of surface carrier distribution in the Cr-doped TI layer under $V_g = -10\mathrm{V}, +3\mathrm{V}$ and $+10\mathrm{V}$. **c**, Magnetization switching phase diagrams under

$V_g = -10\text{V}$, $+1.5\text{V}$ and $+10\text{V}$ in the presence of both B_y and I_{dc}. The dashed lines and symbols (extracted from experiments) represent the boundaries between the different states. **d**, Magnetization switching induced by scanning V_g in the presence of constant B_y and I_{dc} for X: ($I_{\text{dc}} = 20\mu\text{A}$, $B_y = 0.1\text{T}$) and Y: ($I_{\text{dc}} = 20\mu\text{A}$, $B_y = -0.1\text{T}$). Insets show the corresponding initial and final magnetization configurations. All the measurements are performed at 1.9K. Figures are adapted with permission from ref. [58] (Y. Fan's publication).

3.6 Discussion on Correlations between the Topological Surface Current and the Electric-Field Control of Spin-Orbit Torque in the Structure

In this section, we attempt to explore the correlations between the surface carrier densities, surface currents, surface band structures and the measured electric-field control of SOT in the top-gate Hall bar device. As discussed before, the bottom surface states electron density $n_{\mathrm{SS,b}}$ remains unchanged through the whole voltage range while the top surface carriers can be tuned from *p*-type to *n*-type by V_g. Based on a simple capacitor model and the carrier-attracting rate by the top gate, we plot both the top and bottom surface carrier densities as functions of V_g in Fig. 3-10 upper panel. Also depicted are the corresponding top and bottom surface band structures for different voltage regions. It is clear that the bottom surface states electron density $n_{\mathrm{SS,b}}$ is always larger than the top surface states electron density $n_{\mathrm{SS,t}}$ in the whole *n*-type regime. Since the top and bottom surface states carriers have opposite spin-momentum locking directions, we define a net spin-polarized surface current $I_{\mathrm{SS}}^{\mathrm{net}} = I_{\mathrm{SS}}^{\mathrm{bot}} - I_{\mathrm{SS}}^{\mathrm{top}}$, where $I_{\mathrm{SS}}^{\mathrm{top}}$ and $I_{\mathrm{SS}}^{\mathrm{bot}}$ are the top and bottom surface states currents, respectively. Then, the ratio $I_{\mathrm{SS}}^{\mathrm{net}}/I_{\mathrm{tot}}$ (I_{tot} is the total current passing through the film) will quantify the percentage of current that is responsible for producing the SOT. In the region $+3\mathrm{V} < V_g < +10\mathrm{V}$, $\frac{I_{\mathrm{SS}}^{\mathrm{net}}}{I_{\mathrm{tot}}} = \left(n_{\mathrm{SS,b}} - n_{\mathrm{SS,t}}\right) e \mu_{\mathrm{D}} R_{\mathrm{S}}$, where R_{S} is the sheet resistance of the film. In Fig. 3-10 lower panel, we plot both the $I_{\mathrm{SS}}^{\mathrm{net}}/I_{\mathrm{tot}}$ ratio and the current-induced effective field B_{SO} which is obtained from Fig. 3-9b. Surprisingly, the $I_{\mathrm{SS}}^{\mathrm{net}}/I_{\mathrm{tot}}$ ratio and the measured B_{SO} show a quite similar trend in $+3\mathrm{V} < V_g < +10\mathrm{V}$ with $I_{\mathrm{SS}}^{\mathrm{net}}/I_{\mathrm{tot}}$ changing from 0.46 to 0.12 and B_{SO} changing from 79.5mT to 22mT, indicating that $I_{\mathrm{SS}}^{\mathrm{net}}$ is indeed the origin of the induced SOT. In the $-10\mathrm{V} < V_g < +3\mathrm{V}$ region, by assuming that 57% of the top surface accumulated holes are Dirac holes, the $I_{\mathrm{SS}}^{\mathrm{net}}/I_{\mathrm{tot}}$ ratio can also exhibit a trend similar to the B_{SO}

curve. Consequently, the intrinsic spin-torque ratio from $I_{\mathrm{SS}}^{\mathrm{net}}$ can be derived as: $\vartheta_{\mathrm{ST}} = \frac{2eM_{\mathrm{S}}B_{\mathrm{SO}}wt_{\mathrm{S}}t_{\mathrm{Cr-TI}}}{\hbar(I_{\mathrm{SS}}^{\mathrm{net}}/I_{\mathrm{tot}})I_{\mathrm{ac}}^{\mathrm{peak}}}$, where $t_{\mathrm{S}} \cong 1.5\mathrm{nm}$ is the surface states penetration depth [161]. Taking in all the parameters, we find $\vartheta_{\mathrm{ST}} = 116$ and it is independent of V_g. The large ϑ_{ST} value again shows the giant spin-torque efficiency that the TI surface states possess over conventional materials, such as HMFHs.

Here, we would like to mention that by engineering the interface roughness of the film, the current-induced SOT can also be dramatically changed, which again demonstrates the interfacial surface states origin of the SOT (see Section 3.7). The effective electric-field control of SOT, together with the giant spin-torque efficiency of TI [57,59,60] and the high quality of TI/magnetic insulator structures [104], suggests that TI-based magnetic structures may find wide implications in the gate-controlled ultralow power spin-torque devices that are compatible with modern field-effect semiconductor technologies.

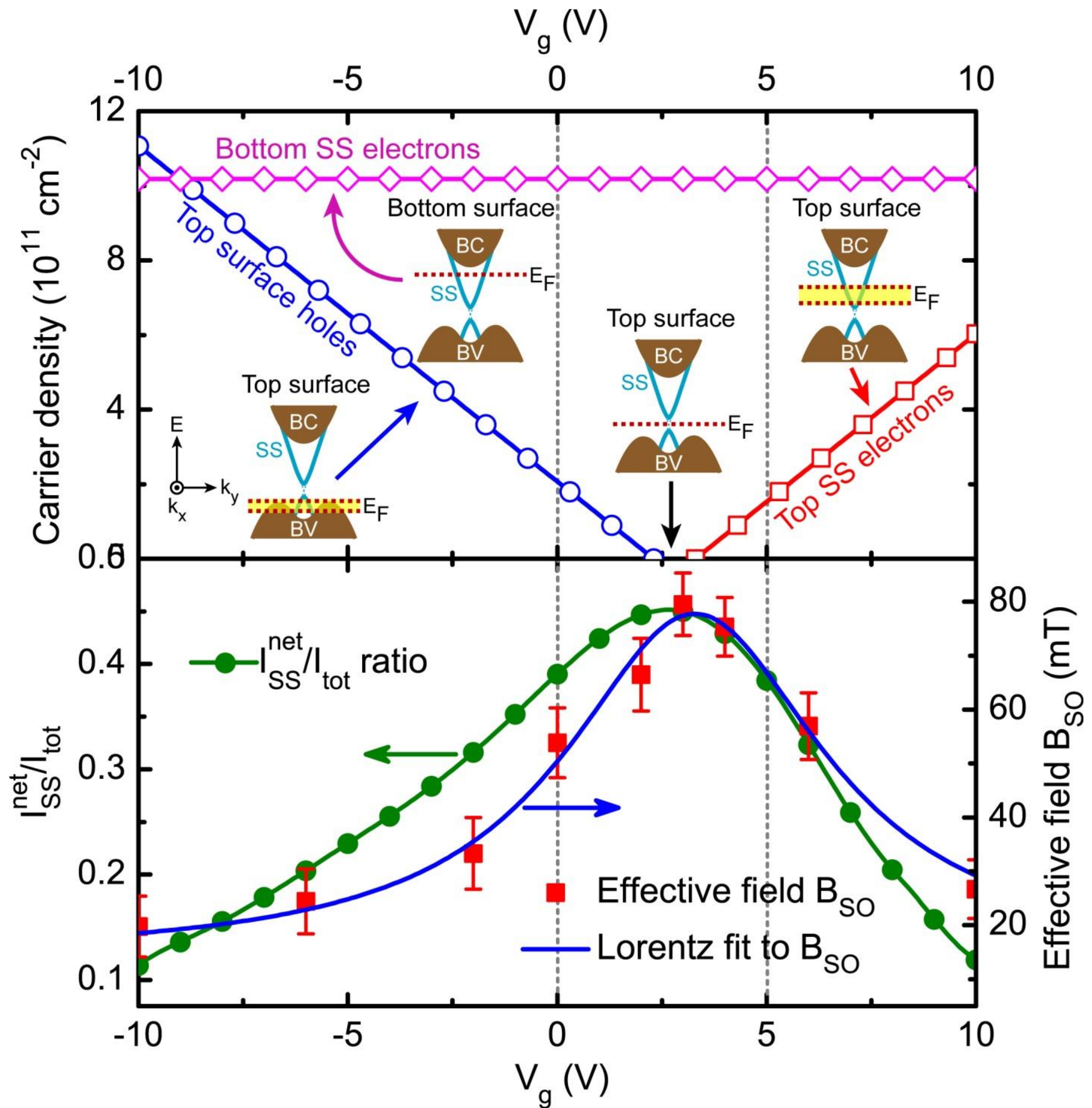

Figure 3-10. Correlations between the surface carrier densities, surface currents, surface band structures and the measured electric-field control of SOT in the top-gate Hall bar device. Upper panel: Top and bottom surface carrier densities as functions of V_g. Insets show the top and bottom surface band structures in different gate voltage regions. Yellow colored area in the top surface band structure shows the tune range of the top surface Fermi level E_F within the

corresponding gate voltage region. Lower panel: comparison between the ratio $I_{\mathrm{SS}}^{\mathrm{net}}/I_{\mathrm{tot}}$ (net spin-polarized surface current over total current) and the effective spin-orbit field B_{SO}, as functions of V_g. The net spin-polarized surface current is defined as $I_{\mathrm{SS}}^{\mathrm{net}} = I_{\mathrm{SS}}^{\mathrm{bot}} - I_{\mathrm{SS}}^{\mathrm{top}}$. B_{SO} is re-plotted here as from Fig. 3-9b. Error bars represent standard errors and blue curve shows the Lorentz fitting. Figure is adapted with permission from ref. [58] (Y. Fan's publication).

3.7 Comparison of the Current-induced Spin-Orbit Torques in Cr-doped TI Films Grown on GaAs Substrates with Smooth and Rough Surface Morphologies

In this section, we address the influence of interface qualities on the surface states transport and current-induced SOT in the Cr-doped TI film in the Al_2O_3/Cr-TI/GaAs(substrate) structure. In Section 3.2, we have mentioned that the atomically flat GaAs (111)B substrate was annealed at 580 ˚C for 5 minutes under Se rich environment (*i.e*, with Se vapor protection) to remove native surface oxide on the substrate. During this procedure, a strained GaSe single atomic layer was formed on the surface, which can protect the substrate surface to be flat after the pre-annealing and improve the growth of the Cr-doped TI film later on [153]. If we perform the pre-annealing without the Se vapor protection, due to the evaporation of As elements, the GaAs surface will evolve into a 3D feature surface structure after reconstruction. In Fig. 3-11a, we show the RHEED patterns of the GaAs substrates after pre-annealing with and without Se vapor protection. It is obvious that the one with Se vapor protection shows streaky patterns which are the 2D feature of the substrate surface, suggesting the surface is atomically flat. In contrast, the one without Se vapor protection shows dotted patterns which are the 3D feature of the substrate surface. This indicates the pre-annealing without Se vapor protection can make the GaAs surface quite rough.

After the pre-annealing, a Cr-doped TI film was grown on the rough GaAs substrate following the same procedure as used in Section 3.2. Here, we present both the HRSTEM and atomic force microscope (AFM) studies of the Cr-doped TI films grown on the smooth GaAs substrate (as prepared in Section 3.2) and on the rough GaAs substrate (pre-annealed without Se vapor protection). As can be seen in Fig. 3-11b, the Cr-doped TI grown on the smooth GaAs substrate shows very nice crystallinity and atomically sharp interface with the substrate.

However, the Cr-doped TI grown on the rough GaAs substrate shows poor crystallinity and a lot of defects at the interface, as indicated by the rectangular box in Fig. 3-11b right panel. When preparing the samples for the HRSTEM study, the top Al_2O_3 protection capping layer was removed and a Pt metal layer was deposited on top of the Cr-doped TI films for the Focused Ion Beam (FIB) process [108]. As a result, we cannot directly study the interface between the capping layer Al_2O_3 and the Cr-doped TI film by HRSTEM. Alternatively, we performed the AFM studies of the two Cr-doped TI films (one grown on smooth GaAs substrate and one on rough GaAs substrate) to probe the top surface morphologies. We find the Cr-doped TI grown on the smooth GaAs substrate shows atomically flat surface morphology, as shown in Fig. 3-11c, while the Cr-doped TI grown on the rough GaAs substrate exhibits many pinholes, as illustrated in Fig. 3-11d, presumably because the GaAs substrate is too rough. In Fig. 3-11e and Fig. 3-11f, we present the surface roughness of the two films along the lines as indicated in Fig. 3-11c and Fig. 3-11d, respectively. Again, the Cr-doped TI grown on the smooth GaAs substrate shows very small roughness while the Cr-doped TI grown on the rough GaAs substrate shows pinholes with the depth even larger than the Cr-doped TI thickness. This indicates that these holes are deep into the GaAs substrate and agrees with the 3D feature RHEED pattern as shown in Fig. 3-11a lower panel.

Furthermore, we have performed both the magneto-transport and second harmonic measurements in the Al_2O_3/Cr-TI/(rough GaAs substrate) Hall bar structure device. The Cr-doped TI film again shows pronounced ferromagnetism (as shown in Fig. 3-12a) and second harmonic signals (as shown in Fig. 3-12b). Intriguingly, the second harmonic AHE resistance, $R_{\mathrm{AHE}}^{2\omega}$, as shown in Fig. 3-12b, changes polarity compared with the one measured in the Al_2O_3/Cr-TI/(smooth GaAs substrate) Hall bar structure (see Fig. 3-4e in Section 3.2). This

means the current-induced SOT has changed sign. In Fig. 3-12c, we plot the effective spin-orbit field B_{SO}, extracted from Fig. 3-12b, as a function of the AC current I_{ac} (*rms* value), and find the effective field versus current ratio is $\frac{|B_{\mathrm{SO}}|}{I_{\mathrm{ac}}^{\mathrm{peak}}} = 2.9\ \mathrm{mT}/\mu\mathrm{A}$ by linear fitting, which is much smaller than the one measured in the Al_2O_3/Cr-TI/(smooth GaAs substrate) structure (see Section 3.2). One possible explanation for the change in the sign of the current-induced SOT in the Al_2O_3/Cr-TI/(rough GaAs substrate) structure is that the large amount of defects at the Cr-TI/(rough GaAs substrate) interface induce many spin-dependent scatterings which can contaminate the bottom surface spin-polarized current, and leaving the top surface spin-polarized current dominant in generating the SOT.

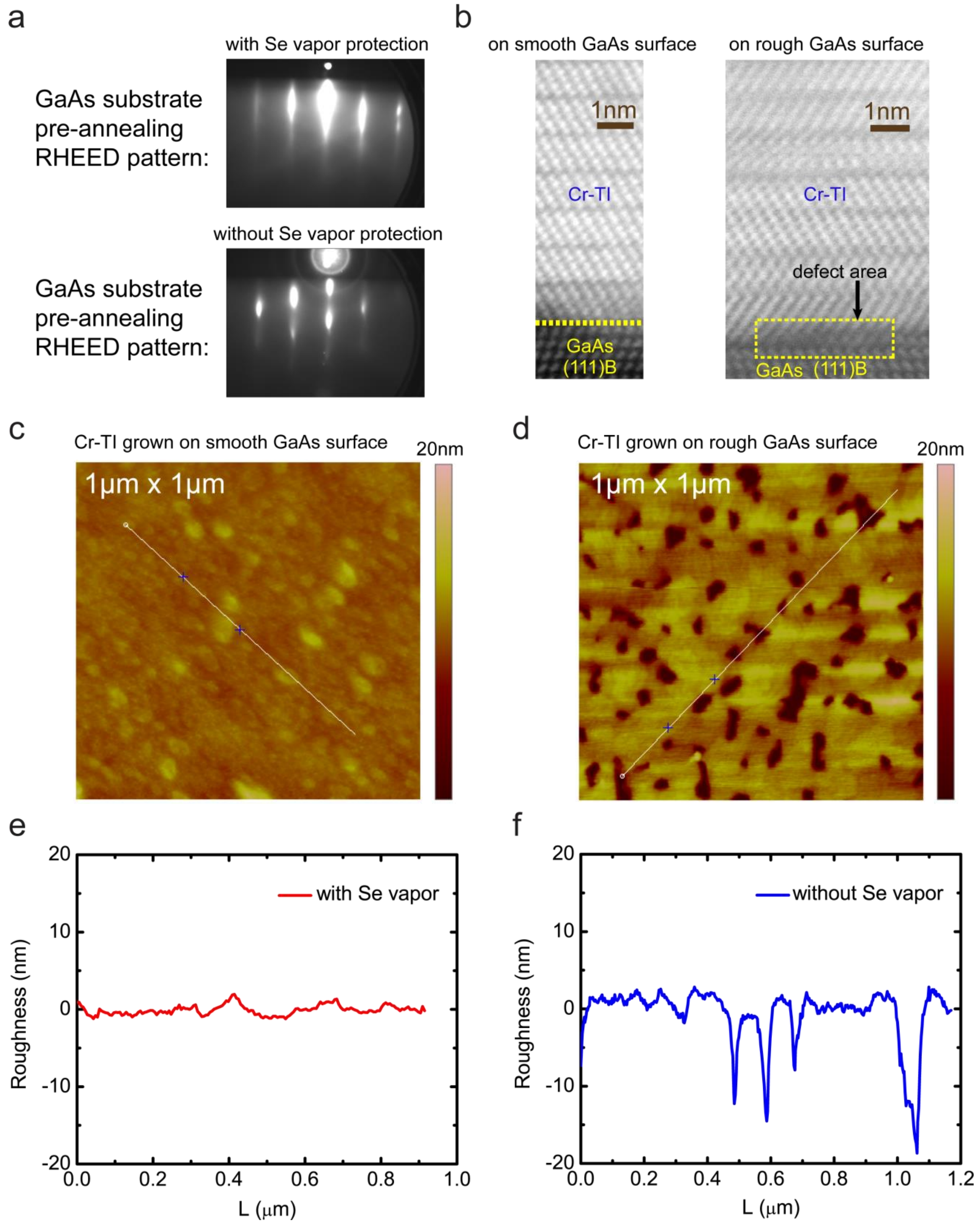

Figure 3-11. Surface morphologies and interfacial properties of the Cr-doped TI films grown on GaAs (111)B substrates pre-annealed with / without Se vapor protection. **a**, RHEED patterns of GaAs (111)B substrates after annealed at 580 ˚C for 5 minutes with / without Se vapor protection.

b, HRSTEM images of the Cr-doped TI films grown on smooth / rough GaAs substrates. **c** and **d**, AFM images of the Cr-doped TI films grown on smooth / rough GaAs substrates, respectively. **e** and **f**, Surface roughness of the Cr-doped TI films along the lines as indicated in **c** and **d**, respectively. Figures are adapted with permission from ref. [58] (Y. Fan's publication).

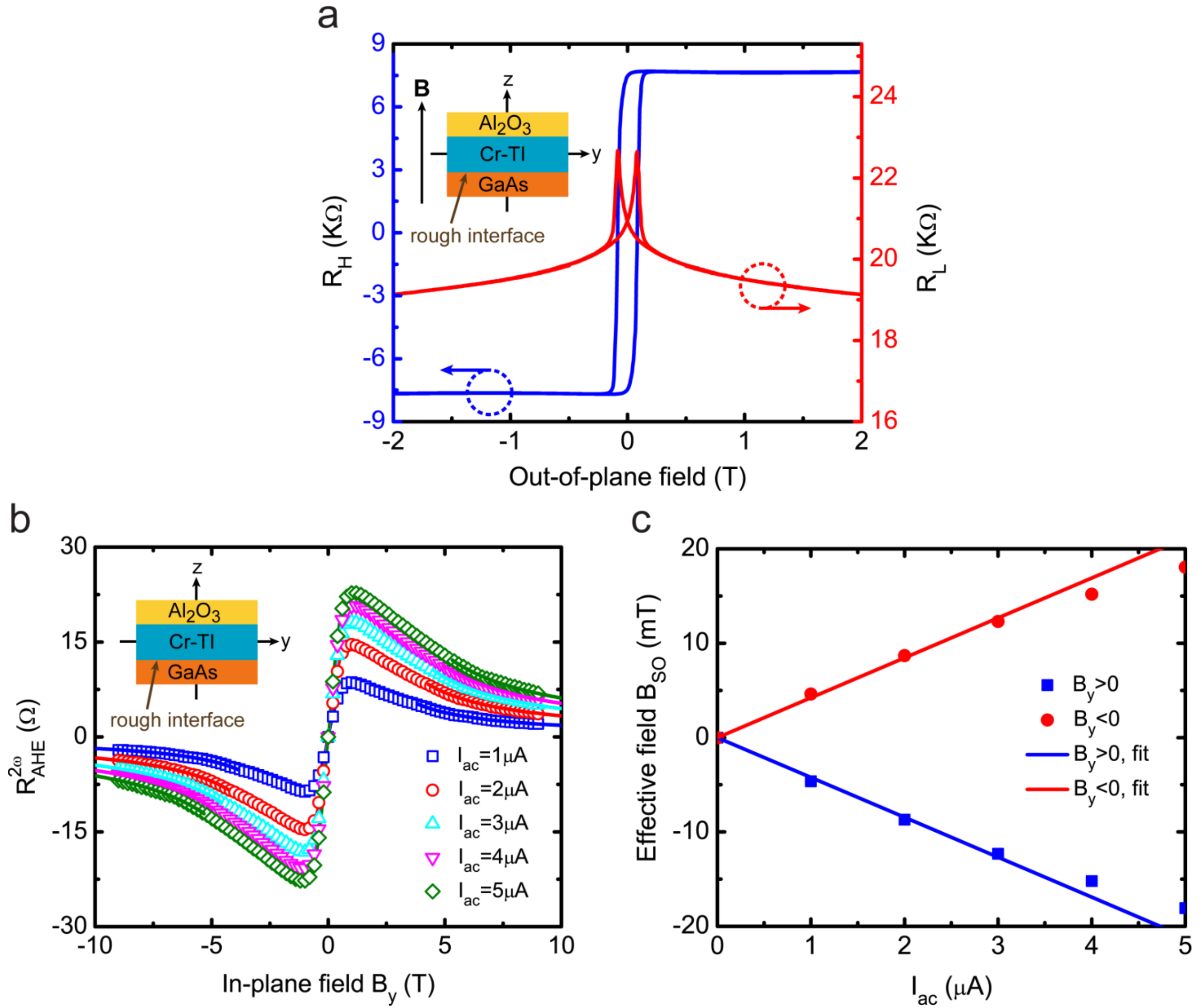

Figure 3-12. Magneto-transport and second harmonic measurements in the Al_2O_3/Cr-TI/(rough GaAs substrate) structure. **a**, Transverse Hall resistance R_H and longitudinal resistance R_L as functions of the out-of-plane magnetic field. Inset: configuration of the applied magnetic field. **b**, Second harmonic AHE resistance as a function of the in-plane magnetic field for AC current

with different *rms* values. The frequency used is 15.8 Hz. Solid lines indicate the fittings proportional to $1/(|B_y| - K)$ in the large field regions. **c**, Effective spin-orbit field B_{SO} as a function of the AC current I_{ac} (*rms* value) for both the $B_y > 0$ and $B_y < 0$ cases as extracted from **b**. Straight lines are the linear fittings. All the measurements are performed at 1.9K. Figures are adapted with permission from ref. [58] (Y. Fan's publication).

Chapter 4

Summary

4.1 Conclusion

In this dissertation we have successfully demonstrated the current-induced giant SOT in the TI/Cr-doped TI bilayer heterostructure and the uniformly Cr-doped TI thin film. Moreover, we have also revealed the effective electric-field control of SOT in the uniformly Cr-doped TI using the top-gate field-effect transistor structure. The giant SOT efficiency and the effective electric-field control of SOT in TI-based magnetic structures may lead to the next generation of gate-controlled ultralow power dissipation spintronic memory and logic devices.

First, the giant SOT was discovered in the TI/Cr-doped TI bilayer heterostructure. The giant SOT was manifested by the current-induced magnetization switching in the bilayer heterostructure in the presence of a fixed in-plane external magnetic field. The critical current density required for switching is below 8.9×10^4 A/cm^2 at 1.9 K. Furthermore, the SOT was calibrated by measuring the effective spin-orbit field using second harmonic methods. Both the effective field to current ratio and the spin-torque ratio are found to be almost three orders of magnitude larger than those reported in HMFHs.

Second, we have demonstrated the effective electric-field control of the giant SOT in a Cr-doped TI thin film using a top-gate field-effect transistor structure. The SOT strength can be modulated by a factor of 4 within the accessible gate voltage range, and it shows strong correlation with the spin-polarized surface current in the Cr-doped TI thin film. Moreover, we have realized the magnetization switching by scanning gate voltage with constant current and in-

plane magnetic field applied in the film. The gate controllability of the SOT in the Cr-doped TI film is almost two orders of magnitude larger than those reported in the gate-controlled HMFHs.

The giant current-induced SOT, the effective electric-field control of SOT and the efficient current-induced magnetization switching exhibited by the Cr-doped TI thin films and modulation-doped heterostructures may lead to the innovation of ultralow power dissipation gate-controlled spin-torque devices (such as spin-torque memory and logic devices) that are compatible with modern field-effect semiconductor technologies. Because the Curie temperature of magnetic TIs is very low (generally below 30 K), to utilize the giant SOT revealed in the TI-based magnetic structures for room temperature applications will require search of high Curie temperature magnetic TIs or other alternative room temperature insulating (or high resistivity) magnetic materials which can couple efficiently with TIs. Since the surface states of TIs are protected by the bulk topology and the spin-momentum locking feature is robust even at room temperature, the giant SOT generated by TIs can in principle sustain up to room temperature, as has been demonstrated by the ST-FMR measurements in TI/ferromagnetic metal structures [59,60]. Therefore, our findings in the magnetic TI thin films and modulation-doped heterostructures, together with other reported progresses in the topological spintronics research field, may lead to the innovation of new SOT devices based on TIs that exhibit much better performance.

4.2 Outlook

Currently, the topological spintronics research field is a quite hot research field. Besides the giant SOT-enabled magnetization switching we have observed in the TI/Cr-doped TI bilayer heterostructure [57] and the uniformly Cr-doped TI thin film [58], other techniques have also been explored to probe the surface spin-related phenomena in TI-based structures, such as the ST-FMR measurement [59,60] and spin-pumping induced spin-to-charge conversion experiment [61-65] in TI/ferromagnet bilayers, the spin-polarized tunneling measurement in the TI/oxide/ferromagnet structure [66] and the electrical detection of surface spin-polarized current in TIs [91,94-98]. All these new advances contribute to the formation of the research field on topological spintronics [99]. For the future potential research opportunities in this field, I would like to address the following material/structure systems --- the TI/ferromagnetic material structures, the TI/antiferromagnet structures, the TI/skyrmion structures, as well as their potential applications.

For the TI/ferromagnetic material structures, after the demonstration of the giant SOT [57,59], it becomes a necessity to find the right ferromagnetic material and structure that has the potential for enabling room-temperature SOT applications. Since the Curie temperature of magnetically doped TIs is very low (usually below 30 K), to search for other alternative room-temperature ferromagnetic materials that can couple efficiently with TIs becomes a priority in the research. Although the TI/ferromagnetic metal structures have been reported capable of generating pronounced SOT [59,60], they suffer from huge shunting problem because of the impedance mismatch issue. Then it comes to TI/magnetic insulator structures (*e.g.*, TI/ YIG) which would most likely offer the right material/structure candidates for room-temperature SOT applications. Indeed, high quality TI/magnetic insulator material and high temperature magnetic proximity

effect have been reported in these structures recently [104,162], and the SOT-related effects are under extensive investigation.

In addition to ferromagnetic materials, the antiferromagnets have become a hot topic recently, due to their unique merits such as insensitive to external disturbing magnetic field, producing no stray field no matter how densely the antiferromagnetic elements are arranged in the device, and the high-frequency (~THz) spin-wave excitations. Moreover, it has been reported that the Neel order in antiferromagnets can be electrically switched [163] through current-induced SOT. Since TIs can produce giant SOT, it would be nice to study the interaction between TIs and antiferromagnets, which might lead to novel spintronic applications. Indeed, recently the Cr-doped TI/antiferromagnet heterostructures and superlattices have been studied [164], which show an enhancement of the Curie temperature of Cr-doped TI due to the exchange coupling between the magnetic TI layer and the antiferromagnet. The TI/antiferromagnet structures seem to be very interesting and the possible SOT effect awaits more explorations.

As we know, TIs have nontrivial band topology in the momentum space. Similarly, there is another class of materials/structures, the so-called skyrmions, which have spin textures with nontrivial topology in the real space. Thus it becomes very reasonable to combine TIs and skyrmions to study the coupling between nontrivial topologies in both the momentum space and the real space. The skyrmions are tiny topological spin textures with potential to serve as carriers of information in future devices. Currently, the room-temperature skyrmions are only realized in magnetic layer/heavy metal heterostructures [165,166] (such as CoFeB/Ta) with large interfacial Dzyaloshinskii-Moriya interaction due to the strong SOC at the magnetic layer/heavy metal interface. Moreover, it has been shown that the skyrmions in these structures can be driven by the current-induced SOT [165,166], suggesting potential electrically-controllable spintronic

applications. Since TIs are even more efficient in generating SOT than heavy metals, it looks promising to combine TIs with skyrmion materials so as to enhance the interfacial Dzyaloshinskii-Moriya interaction as well as the SOT efficiency when a charge current is passing through. Therefore, more research efforts are needed to address these proposed ideas.

Application wise, using the giant SOT generated by TI, the TI/ferromagnetic material structures might enable ultralow power-dissipation memory devices, such as the 3-terminal MTJ structures in MRAM. When combined with CMOS logic circuitry, TI/ferromagnetic material structures may also offer efficient non-volatile spin logic devices. By carefully designing the structure geometry and dimension, these TI/ferromagnetic material structures may further enable energy-efficient SOT oscillators. Compared with the TI/ferromagnetic material structures, the TI/antiferromagnet structures might find applications in the high-frequency spintronic devices, such as THz spin-wave generators and high-frequency magnonic oscillators. For the TI/skyrmion structures, they may find applications in the ultralow power-dissipation racetrack memories that have very high density and consume very low power. In summary, the feasibility of combining TIs with various magnetic materials/structures and their rich applications will spur further research in this vigorous topological spintronics field based on TIs.

References

1. Wolf, S.A. *et al.*, Spintronics: A Spin-Based Electronics Vision for the Future. *Science* **294**, 1488-1495 (2001).
2. Žutić, I., Fabian, J., & Das Sarma, S., Spintronics: Fundamentals and applications. *Rev. Mod. Phys.* **76**, 323-410 (2004).
3. Bader, S.D. & Parkin, S.S.P., Spintronics. *Annu. Rev. Condens. Matter Phys.* **1**, 71-88 (2010).
4. *International Technology Roadmap of Semiconductors (ITRS)*. (2015).
5. Datta, S. & Das, B., Electronic analog of the electro-optic modulator. *Appl. Phys. Lett.* **56**, 665-667 (1990).
6. Sugahara, S. & Tanaka, M., A spin metal–oxide–semiconductor field-effect transistor using half-metallic-ferromagnet contacts for the source and drain. *Appl. Phys. Lett.* **84**, 2307-2309 (2004).
7. Kent, A.D. & Worledge, D.C., A new spin on magnetic memories. *Nature Nanotech.* **10**, 187-191 (2015).
8. Ralph, D.C. & Stiles, M.D., Spin transfer torques. *J. Magn. Magn. Mater.* **320**, 1190-1216 (2008).
9. Garello, K. *et al.*, Symmetry and magnitude of spin-orbit torques in ferromagnetic heterostructures. *Nature Nanotech.* **8**, 587-593 (2013).
10. Slonczewski, J.C., Conductance and exchange coupling of two ferromagnets separated by a tunneling barrier. *Phys. Rev. B* **39**, 6995-7002 (1989).
11. Slonczewski, J.C., Current-driven excitation of magnetic multilayers. *J. Magn. Magn. Mater.* **159**, L1-L7 (1996).

12 Berger, L., Emission of spin waves by a magnetic multilayer traversed by a current. *Phys. Rev. B* **54**, 9353-9358 (1996).

13 Stiles, M.D. & Zangwill, A., Anatomy of spin-transfer torque. *Phys. Rev. B* **66**, 014407 (2002).

14 Brataas, A., Kent, A.D., & Ohno, H., Current-induced torques in magnetic materials. *Nature Mater.* **11**, 372-381 (2012).

15 Myers, E.B., Ralph, D.C., Katine, J.A., Louie, R.N., & Buhrman, R.A., Current-Induced Switching of Domains in Magnetic Multilayer Devices. *Science* **285**, 867-870 (1999).

16 Katine, J.A., Albert, F.J., Buhrman, R.A., Myers, E.B., & Ralph, D.C., Current-Driven Magnetization Reversal and Spin-Wave Excitations in Co/Cu/Co Pillars. *Phys. Rev. Lett.* **84**, 3149-3152 (2000).

17 Julliere, M., Tunneling between ferromagnetic films. *Phys. Lett. A* **54**, 225-226 (1975).

18 Moodera, J.S., Kinder, L.R., Wong, T.M., & Meservey, R., Large Magnetoresistance at Room Temperature in Ferromagnetic Thin Film Tunnel Junctions. *Phys. Rev. Lett.* **74**, 3273-3276 (1995).

19 Miyazaki, T. & Tezuka, N., Giant magnetic tunneling effect in Fe/Al_2O_3/Fe junction. *J. Magn. Magn. Mater.* **139**, L231-L234 (1995).

20 Wang, D., C., N., M., D.J., Zhenghong, Q., & J., F., 70% TMR at room temperature for SDT sandwich junctions with CoFeB as free and reference Layers. *IEEE Trans. Magn.* **40**, 2269-2271 (2004).

21 Butler, W.H., Zhang, X.G., Schulthess, T.C., & MacLaren, J.M., Spin-dependent tunneling conductance of Fe|MgO|Fe sandwiches. *Phys. Rev. B* **63**, 054416 (2001).

22 Yuasa, S., Nagahama, T., Fukushima, A., Suzuki, Y., & Ando, K., Giant room-temperature magnetoresistance in single-crystal Fe/MgO/Fe magnetic tunnel junctions. *Nature Mater.* **3**, 868-871 (2004).

23 Parkin, S.S.P. *et al.*, Giant tunnelling magnetoresistance at room temperature with MgO (100) tunnel barriers. *Nature Mater.* **3**, 862-867 (2004).

24 Min, T. *et al.*, A Study of Write Margin of Spin Torque Transfer Magnetic Random Access Memory Technology. *IEEE Trans. Magn.* **46**, 2322-2327 (2010).

25 Bernevig, B.A. & Vafek, O., Piezo-magnetoelectric effects in *p*-doped semiconductors. *Phys. Rev. B* **72**, 033203 (2005).

26 Chernyshov, A. *et al.*, Evidence for reversible control of magnetization in a ferromagnetic material by means of spin-orbit magnetic field. *Nature Phys.* **5**, 656-659 (2009).

27 Sinova, J., Valenzuela, S.O., Wunderlich, J., Back, C.H., & Jungwirth, T., Spin Hall effects. *Rev. Mod. Phys.* **87**, 1213-1260 (2015).

28 Hoffmann, A., Spin Hall Effects in Metals. *IEEE Trans. Magn.* **49**, 5172-5193 (2013).

29 Jungwirth, T., Wunderlich, J., & Olejnik, K., Spin Hall effect devices. *Nature Mater.* **11**, 382-390 (2012).

30 Maekawa, S. & Takahashi, S., *Spin Current*. (Oxford University Press, New York, 2012).

31 Valenzuela, S.O. & Kimura, T., *Spin Current*. (Oxford University Press, New York, 2012).

32 Murakami, S., Nagaosa, N., & Zhang, S.-C., Dissipationless Quantum Spin Current at Room Temperature. *Science* **301**, 1348-1351 (2003).

33 Sinova, J. *et al.*, Universal Intrinsic Spin Hall Effect. *Phys. Rev. Lett.* **92**, 126603 (2004).

34 Nagaosa, N., Sinova, J., Onoda, S., MacDonald, A.H., & Ong, N.P., Anomalous Hall effect. *Rev. Mod. Phys.* **82**, 1539-1592 (2010).

35 Dyakonov, M.I. & Perel, V.I., Current-induced spin orientation of electrons in semiconductors. *Phys. Lett. A* **35**, 459-460 (1971).

36 Zhang, S., Spin Hall Effect in the Presence of Spin Diffusion. *Phys. Rev. Lett.* **85**, 393-396 (2000).

37 Hirsch, J.E., Spin Hall Effect. *Phys. Rev. Lett.* **83**, 1834-1837 (1999).

38 Liu, L. *et al.*, Spin-Torque Switching with the Giant Spin Hall Effect of Tantalum. *Science* **336**, 555-558 (2012).

39 Kato, Y.K., Myers, R.C., Gossard, A.C., & Awschalom, D.D., Observation of the Spin Hall Effect in Semiconductors. *Science* **306**, 1910-1913 (2004).

40 Wunderlich, J., Kaestner, B., Sinova, J., & Jungwirth, T., Experimental Observation of the Spin-Hall Effect in a Two-Dimensional Spin-Orbit Coupled Semiconductor System. *Phys. Rev. Lett.* **94**, 047204 (2005).

41 Miron, I.M. *et al.*, Perpendicular switching of a single ferromagnetic layer induced by in-plane current injection. *Nature* **476**, 189-193 (2011).

42 Liu, L., Lee, O.J., Gudmundsen, T.J., Ralph, D.C., & Buhrman, R.A., Current-Induced Switching of Perpendicularly Magnetized Magnetic Layers Using Spin Torque from the Spin Hall Effect. *Phys. Rev. Lett.* **109**, 096602 (2012).

43 Yu, G. *et al.*, Switching of perpendicular magnetization by spin-orbit torques in the absence of external magnetic fields. *Nature Nanotech.* **9**, 548-554 (2014).

44 Ando, K. *et al.*, Electric Manipulation of Spin Relaxation Using the Spin Hall Effect. *Phys. Rev. Lett.* **101**, 036601 (2008).

45 Liu, L., Moriyama, T., Ralph, D.C., & Buhrman, R.A., Spin-Torque Ferromagnetic Resonance Induced by the Spin Hall Effect. *Phys. Rev. Lett.* **106**, 036601 (2011).

46 Wang, Z., Sun, Y., Wu, M., Tiberkevich, V., & Slavin, A., Control of Spin Waves in a Thin Film Ferromagnetic Insulator through Interfacial Spin Scattering. *Phys. Rev. Lett.* **107**, 146602 (2011).

47 Demidov, V.E. *et al.*, Control of Magnetic Fluctuations by Spin Current. *Phys. Rev. Lett.* **107**, 107204 (2011).

48 Wang, Z. *et al.*, Electric control of magnetization relaxation in thin film magnetic insulators. *Appl. Phys. Lett.* **99**, 162511 (2011).

49 Padrón-Hernández, E., Azevedo, A., & Rezende, S.M., Amplification of spin waves in yttrium iron garnet films through the spin Hall effect. *Appl. Phys. Lett.* **99**, 192511 (2011).

50 Kajiwara, Y. *et al.*, Transmission of electrical signals by spin-wave interconversion in a magnetic insulator. *Nature* **464**, 262-266 (2010).

51 Miron, I.M. *et al.*, Fast current-induced domain-wall motion controlled by the Rashba effect. *Nature Mater.* **10**, 419-423 (2011).

52 Haazen, P.P.J. *et al.*, Domain wall depinning governed by the spin Hall effect. *Nature Mater.* **12**, 299-303 (2013).

53 Emori, S., Bauer, U., Ahn, S.-M., Martinez, E., & Beach, G.S.D., Current-driven dynamics of chiral ferromagnetic domain walls. *Nature Mater.* **12**, 611-616 (2013).

54 Qi, X.-L. & Zhang, S.-C., Topological insulators and superconductors. *Rev. Mod. Phys.* **83**, 1057-1110 (2011).

55 Hasan, M.Z. & Kane, C.L., Colloquium: Topological insulators. *Rev. Mod. Phys.* **82**, 3045-3067 (2010).

56 Moore, J.E., The birth of topological insulators. *Nature* **464**, 194-198 (2010).

57 Fan, Y. *et al.*, Magnetization switching through giant spin-orbit torque in a magnetically doped topological insulator heterostructure. *Nature Mater.* **13**, 699-704 (2014).

58 Fan, Y. *et al.*, Electric-field control of spin–orbit torque in a magnetically doped topological insulator. *Nature Nanotech.* **11**, 352-359 (2016).

59 Mellnik, A.R. *et al.*, Spin-transfer torque generated by a topological insulator. *Nature* **511**, 449-451 (2014).

60 Wang, Y. *et al.*, Topological Surface States Originated Spin-Orbit Torques in Bi_2Se_3. *Phys. Rev. Lett.* **114**, 257202 (2015).

61 Shiomi, Y. *et al.*, Spin-Electricity Conversion Induced by Spin Injection into Topological Insulators. *Phys. Rev. Lett.* **113**, 196601 (2014).

62 Deorani, P. *et al.*, Observation of inverse spin Hall effect in bismuth selenide. *Phys. Rev. B* **90**, 094403 (2014).

63 Jamali, M. *et al.*, Giant Spin Pumping and Inverse Spin Hall Effect in the Presence of Surface and Bulk Spin-Orbit Coupling of Topological Insulator Bi_2Se_3. *Nano Lett.* **15**, 7126-7132 (2015).

64 Baker, A.A., Figueroa, A.I., Collins-McIntyre, L.J., van der Laan, G., & Hesjedal, T., Spin pumping in Ferromagnet-Topological Insulator-Ferromagnet Heterostructures. *Sci. Rep.* **5**, 7907 (2015).

65 Rojas-Sánchez, J.C. *et al.*, Spin to Charge Conversion at Room Temperature by Spin Pumping into a New Type of Topological Insulator: α-Sn Films. *Phys. Rev. Lett.* **116**, 096602 (2016).

66 Liu, L. *et al.*, Spin-polarized tunneling study of spin-momentum locking in topological insulators. *Phys. Rev. B* **91**, 235437 (2015).

67 Pai, C.-F. *et al.*, Spin transfer torque devices utilizing the giant spin Hall effect of tungsten. *Appl. Phys. Lett.* **101**, 122404 (2012).

68 Niimi, Y. *et al.*, Giant Spin Hall Effect Induced by Skew Scattering from Bismuth Impurities inside Thin Film CuBi Alloys. *Phys. Rev. Lett.* **109**, 156602 (2012).

69 Zhang, H. *et al.*, Topological insulators in Bi_2Se_3, Bi_2Te_3 and Sb_2Te_3 with a single Dirac cone on the surface. *Nature Phys.* **5**, 438-442 (2009).

70 Qi, X.-L., Hughes, T.L., & Zhang, S.-C., Topological field theory of time-reversal invariant insulators. *Phys. Rev. B* **78**, 195424 (2008).

71 Bernevig, B.A., Hughes, T.L., & Zhang, S.C., Quantum spin Hall effect and topological phase transition in HgTe quantum wells. *Science* **314**, 1757-1761 (2006).

72 Konig, M. *et al.*, Quantum spin hall insulator state in HgTe quantum wells. *Science* **318**, 766-770 (2007).

73 Fu, L. & Kane, C.L., Topological insulators with inversion symmetry. *Phys. Rev. B* **76**, 045302 (2007).

74 Roth, A. *et al.*, Nonlocal Transport in the Quantum Spin Hall State. *Science* **325**, 294-297 (2009).

75 Qi, X.L. & Zhang, S.C., The quantum spin Hall effect and topological insulators. *Phys. Today* **63**, 33-38 (2010).

76 Liu, C.-X. *et al.*, Model Hamiltonian for topological insulators. *Phys. Rev. B* **82**, 045122 (2010).

77 Fu, L., Kane, C.L., & Mele, E.J., Topological insulators in three dimensions. *Phys. Rev. Lett.* **98**, 106803 (2007).

78 Hsieh, D. *et al.*, A topological Dirac insulator in a quantum spin Hall phase. *Nature* **452**, 970-U975 (2008).

79 Chen, Y.L. *et al.*, Experimental Realization of a Three-Dimensional Topological Insulator, Bi_2Te_3. *Science* **325**, 178-181 (2009).

80 Chen, Y.L. *et al.*, Massive Dirac Fermion on the Surface of a Magnetically Doped Topological Insulator. *Science* **329**, 659-662 (2010).

81 Xia, Y. *et al.*, Observation of a large-gap topological-insulator class with a single Dirac cone on the surface. *Nature Phys.* **5**, 398-402 (2009).

82 Hsieh, D. *et al.*, A tunable topological insulator in the spin helical Dirac transport regime. *Nature* **460**, 1101-1105 (2009).

83 Hsieh, D. *et al.*, Observation of Unconventional Quantum Spin Textures in Topological Insulators. *Science* **323**, 919-922 (2009).

84 Hsieh, D. *et al.*, Observation of Time-Reversal-Protected Single-Dirac-Cone Topological-Insulator States in Bi_2Te_3 and Sb_2Te_3. *Phys. Rev. Lett.* **103**, 146401 (2009).

85 Xu, S.-Y. *et al.*, Topological Phase Transition and Texture Inversion in a Tunable Topological Insulator. *Science* **332**, 560-564 (2011).

86 Pan, Z.H. *et al.*, Electronic Structure of the Topological Insulator Bi_2Se_3 Using Angle-Resolved Photoemission Spectroscopy: Evidence for a Nearly Full Surface Spin Polarization. *Phys. Rev. Lett.* **106**, 257004 (2011).

87 McIver, J.W., HsiehD, SteinbergH, Jarillo Herrero, P., & GedikN, Control over topological insulator photocurrents with light polarization. *Nature Nanotech.* **7**, 96-100 (2012).

88 Jozwiak, C. *et al.*, Photoelectron spin-flipping and texture manipulation in a topological insulator. *Nature Phys.* **9**, 293-298 (2013).

89 Park, C.-H. & Louie, S.G., Spin Polarization of Photoelectrons from Topological Insulators. *Phys. Rev. Lett.* **109**, 097601 (2012).

90 Yazyev, O.V., Moore, J.E., & Louie, S.G., Spin Polarization and Transport of Surface States in the Topological Insulators Bi_2Se_3 and Bi_2Te_3 from First Principles. *Phys. Rev. Lett.* **105**, 266806 (2010).

91 Tang, J. *et al.*, Electrical Detection of Spin-Polarized Surface States Conduction in $(Bi_{0.53}Sb_{0.47})_2Te_3$ Topological Insulator. *Nano Lett.* **14**, 5423-5429 (2014).

92 Baibich, M.N. *et al.*, Giant Magnetoresistance of (001)Fe/(001)Cr Magnetic Superlattices. *Phys. Rev. Lett.* **61**, 2472-2475 (1988).

93 Binasch, G., Grünberg, P., Saurenbach, F., & Zinn, W., Enhanced magnetoresistance in layered magnetic structures with antiferromagnetic interlayer exchange. *Phys. Rev. B* **39**, 4828-4830 (1989).

94 Li, C.H. *et al.*, Electrical detection of charge-current-induced spin polarization due to spin-momentum locking in Bi_2Se_3. *Nature Nanotech.* **9**, 218-224 (2014).

95 Ando, Y. *et al.*, Electrical Detection of the Spin Polarization Due to Charge Flow in the Surface State of the Topological Insulator $Bi_{1.5}Sb_{0.5}Te_{1.7}Se_{1.3}$. *Nano Lett.* **14**, 6226-6230 (2014).

96 Tian, J. *et al.*, Topological insulator based spin valve devices: Evidence for spin polarized transport of spin-momentum-locked topological surface states. *Solid State Commun.* **191**, 1-5 (2014).

97 Tian, J., Miotkowski, I., Hong, S., & Chen, Y.P., Electrical injection and detection of spin-polarized currents in topological insulator Bi_2Te_2Se. *Sci. Rep.* **5**, 14293 (2015).

98 Dankert, A., Geurs, J., Kamalakar, M.V., Charpentier, S., & Dash, S.P., Room Temperature Electrical Detection of Spin Polarized Currents in Topological Insulators. *Nano Lett.* **15**, 7976-7981 (2015).

99 Kim, J.-V., Solid-state physics: Siphoning spins. *Nature* **511**, 418-419 (2014).

100 Roushan, P. *et al.*, Topological surface states protected from backscattering by chiral spin texture. *Nature* **460**, 1106-1109 (2009).

101 Zhang, T. *et al.*, Experimental Demonstration of Topological Surface States Protected by Time-Reversal Symmetry. *Phys. Rev. Lett.* **103**, 266803 (2009).

102 Kong, D. *et al.*, Ambipolar field effect in the ternary topological insulator $(Bi_xSb_{1-x})_2Te_3$ by composition tuning. *Nature Nanotech.* **6**, 705-709 (2011).

103 Xu, Y. *et al.*, Observation of topological surface state quantum Hall effect in an intrinsic three-dimensional topological insulator. *Nature Phys.* **10**, 956-963 (2014).

104 Lang, M. *et al.*, Proximity Induced High-Temperature Magnetic Order in Topological Insulator - Ferrimagnetic Insulator Heterostructure. *Nano Lett.* **14**, 3459-3465 (2014).

105 Wei, P. *et al.*, Exchange-Coupling-Induced Symmetry Breaking in Topological Insulators. *Phys. Rev. Lett.* **110**, 186807 (2013).

106 Yang, Q.I. *et al.*, Emerging weak localization effects on a topological insulator-insulating ferromagnet (Bi_2Se_3-EuS) interface. *Phys. Rev. B* **88**, 081407 (2013).

107 Kou, X.F. *et al.*, Magnetically doped semiconducting topological insulators. *J. Appl. Phys.* **112**, 063912 (2012).

108 Kou, X. *et al.*, Interplay between Different Magnetisms in Cr-Doped Topological Insulators. *ACS Nano* **7**, 9205-9212 (2013).

109 Kou, X. *et al.*, Manipulating Surface-related Ferromagnetism in Modulation-doped Topological Insulators. *Nano Lett.* **13**, 4587-4593 (2013).

110 Kou, X. *et al.*, Scale-Invariant Quantum Anomalous Hall Effect in Magnetic Topological Insulators beyond the Two-Dimensional Limit. *Phys. Rev. Lett.* **113**, 137201 (2014).

111 Kou, X., Fan, Y., Lang, M., Upadhyaya, P., & Wang, K.L., Magnetic topological insulators and quantum anomalous hall effect. *Solid State Commun.* **215-216**, 34-53 (2015).

112 Chang, C.-Z. *et al.*, Experimental Observation of the Quantum Anomalous Hall Effect in a Magnetic Topological Insulator. *Science* **340**, 167-170 (2013).

113 Chang, C.-Z. *et al.*, High-precision realization of robust quantum anomalous Hall state in a hard ferromagnetic topological insulator. *Nature Mater.* **14**, 473-477 (2015).

114 Checkelsky, J.G. *et al.*, Trajectory of the anomalous Hall effect towards the quantized state in a ferromagnetic topological insulator. *Nature Phys.* **10**, 731-736 (2014).

115 Wray, L.A. *et al.*, A topological insulator surface under strong Coulomb, magnetic and disorder perturbations. *Nature Phys.* **7**, 32-37 (2011).

116 Kim, J. *et al.*, Layer thickness dependence of the current-induced effective field vector in Ta|CoFeB|MgO. *Nature Mater.* **12**, 240-245 (2013).

117 Suzuki, T. *et al.*, Current-induced effective field in perpendicularly magnetized Ta/CoFeB/MgO wire. *Appl. Phys. Lett.* **98**, 142505 (2011).

118 Miron, I.M. *et al.*, Current-driven spin torque induced by the Rashba effect in a ferromagnetic metal layer. *Nature Mater.* **9**, 230-234 (2010).

119 Pi, U.H. *et al.*, Tilting of the spin orientation induced by Rashba effect in ferromagnetic metal layer. *Appl. Phys. Lett.* **97**, 162507 (2010).

120 Vedyayev, A., Strelkov, N., Chshiev, M., Ryzhanova, N., & Dieny, B., Spin Transfer Torques induced by Spin Hall Effect. *http://arxiv.org/abs/1108.2589v1* (2011).

121 Manchon, A., Spin Hall effect versus Rashba torque: a Diffusive Approach. *http://arxiv.org/abs/1204.4869* (2012).

122 Wang, X. & Manchon, A., Diffusive Spin Dynamics in Ferromagnetic Thin Films with a Rashba Interaction. *Phys. Rev. Lett.* **108**, 117201 (2012).

123 Pesin, D.A. & MacDonald, A.H., Quantum kinetic theory of current-induced torques in Rashba ferromagnets. *Phys. Rev. B* **86**, 014416 (2012).

124 Haney, P.M., Lee, H.-W., Lee, K.-J., Manchon, A., & Stiles, M.D., Current induced torques and interfacial spin-orbit coupling: Semiclassical modeling. *Phys. Rev. B* **87**, 174411 (2013).

125 Kim, K.-W., Seo, S.-M., Ryu, J., Lee, K.-J., & Lee, H.-W., Magnetization dynamics induced by in-plane currents in ultrathin magnetic nanostructures with Rashba spin-orbit coupling. *Phys. Rev. B* **85**, 180404 (2012).

126 Wang, X. & Manchon, A., Rashba spin torque in an ultrathin ferromagnetic metal layer. *http://arxiv.org/abs/1111.5466* (2011).

127 Fischer, M.H., Vaezi, A., Manchon, A., & Kim, E.-A., Large Spin Torque in Topological Insulator/Ferromagnetic Metal Bilayers. *http://arxiv.org/abs/1305.1328* (2013).

128 Mahfouzi, F., Nagaosa, N., & Nikolic, B.K., Spin-Orbit Coupling Induced Spin-Transfer Torque and Current Polarization in Topological-Insulator/Ferromagnet Vertical Heterostructures. *Phys. Rev. Lett.* **109**, 166602 (2012).

129 Tserkovnyak, Y. & Loss, D., Thin-Film Magnetization Dynamics on the Surface of a Topological Insulator. *Phys. Rev. Lett.* **108**, 187201 (2012).

130 Checkelsky, J.G., Ye, J., Onose, Y., Iwasa, Y., & Tokura, Y., Dirac-fermion-mediated ferromagnetism in a topological insulator. *Nature Phys.* **8**, 729-733 (2012).

131 Chang, C.-Z. *et al.*, Thin Films of Magnetically Doped Topological Insulator with Carrier-Independent Long-Range Ferromagnetic Order. *Adv. Mater.* **25**, 1065-1070 (2013).

132 He, L. *et al.*, Surface-Dominated Conduction in a 6 nm thick Bi_2Se_3 Thin Film. *Nano Lett.* **12**, 1486-1490 (2012).

133 Kou, X. *et al.*, Metal-to-insulator switching in quantum anomalous Hall states. *Nat. Commun.* **6**, 8474 (2015).

134 Lang, M. *et al.*, Revelation of Topological Surface States in Bi_2Se_3 Thin Films by In Situ Al Passivation. *ACS Nano* **6**, 295-302 (2012).

135 Hong, S.S., Cha, J.J., Kong, D.S., & Cui, Y., Ultra-low carrier concentration and surface-dominant transport in antimony-doped Bi_2Se_3 topological insulator nanoribbons. *Nat. Commun.* **3** (2012).

136 Arakane, T. *et al.*, Tunable Dirac cone in the topological insulator $Bi_{2-x}Sb_xTe_{3-y}Se_y$. *Nat. Commun.* **3** (2012).

137 Garate, I. & Franz, M., Inverse Spin-Galvanic Effect in the Interface between a Topological Insulator and a Ferromagnet. *Phys. Rev. Lett.* **104**, 146802 (2010).

138 Nomura, K. & Nagaosa, N., Electric charging of magnetic textures on the surface of a topological insulator. *Phys. Rev. B* **82**, 161401 (2010).

139 Ohno, H. *et al.*, Electric-field control of ferromagnetism. *Nature* **408**, 944-946 (2000).

140 Chiba, D., Yamanouchi, M., Matsukura, F., & Ohno, H., Electrical Manipulation of Magnetization Reversal in a Ferromagnetic Semiconductor. *Science* **301**, 943-945 (2003).

141 Xiu, F. *et al.*, Electric-field-controlled ferromagnetism in high-Curie-temperature $Mn_{0.05}Ge_{0.95}$ quantum dots. *Nature Mater.* **9**, 337-344 (2010).

142 Chiba, D. *et al.*, Magnetization vector manipulation by electric fields. *Nature* **455**, 515-518 (2008).

143 Tokura, Y., Multiferroics as Quantum Electromagnets. *Science* **312**, 1481-1482 (2006).

144 Eerenstein, W., Mathur, N.D., & Scott, J.F., Multiferroic and magnetoelectric materials. *Nature* **442**, 759-765 (2006).

145 Heron, J.T. *et al.*, Deterministic switching of ferromagnetism at room temperature using an electric field. *Nature* **516**, 370-373 (2014).

146 Maruyama, T. *et al.*, Large voltage-induced magnetic anisotropy change in a few atomic layers of iron. *Nature Nanotech.* **4**, 158-161 (2009).

147 Amiri, P.K. & Wang, K.L., Voltage-controlled magnetic anisotropy in spintronic devices. *Spin* **02**, 1240002 (2012).

148 Liu, R.H., Lim, W.L., & Urazhdin, S., Control of current-induced spin-orbit effects in a ferromagnetic heterostructure by electric field. *Phys. Rev. B* **89**, 220409 (2014).

149 Bauer, U. *et al.*, Magneto-ionic control of interfacial magnetism. *Nature Mater.* **14**, 174-181 (2015).

150 Tserkovnyak, Y. & Bender, S.A., Spin Hall phenomenology of magnetic dynamics. *Phys. Rev. B* **90**, 014428 (2014).

151 Lang, M. *et al.*, Competing Weak Localization and Weak Antilocalization in Ultrathin Topological Insulators. *Nano Lett.* **13**, 48-53 (2013).

152 Skinner, B., Chen, T., & Shklovskii, B.I., Why Is the Bulk Resistivity of Topological Insulators So Small? *Phys. Rev. Lett.* **109**, 176801 (2012).

153 He, L. *et al.*, Evidence of the two surface states of $(Bi_{0.53}Sb_{0.47})_2Te_3$ films grown by van der Waals epitaxy. *Sci. Rep.* **3**, 3406 (2013).

154 Zhang, J. *et al.*, Band structure engineering in $(Bi_{1-x}Sb_x)_2Te_3$ ternary topological insulators. *Nat. Commun.* **2**, 574 (2011).

155 Wang, J., Lian, B., & Zhang, S.-C., Electrically Tunable Magnetism in Magnetic Topological Insulators. *arXiv:1412.8237* (2015).

156 Hook, J.R. & Hall, H.E., *Solid State Physics, 2nd Edition*. (Willey, 1995).

157 Qu, D.X., Hor, Y.S., Xiong, J., Cava, R.J., & Ong, N.P., Quantum Oscillations and Hall Anomaly of Surface States in the Topological Insulator Bi_2Te_3. *Science* **329**, 821-824 (2010).

158 Ren, Z., Taskin, A.A., Sasaki, S., Segawa, K., & Ando, Y., Large bulk resistivity and surface quantum oscillations in the topological insulator Bi_2Te_2Se. *Phys. Rev. B* **82**, 241306 (2010).

159 Analytis, J.G. *et al.*, Two-dimensional surface state in the quantum limit of a topological insulator. *Nature Phys.* **6**, 960-964 (2010).

160 Yu, X. *et al.*, Separation of top and bottom surface conduction in Bi_2Te_3 thin films. *Nanotechnology* **24**, 015705 (2013).

161 Zhang, W., Yu, R., Zhang, H.-J., Dai, X., & Fang, Z., First-principles studies of the three-dimensional strong topological insulators Bi_2Te_3, Bi_2Se_3 and Sb_2Te_3. *New J. Phys.* **12**, 065013 (2010).

162 Katmis, F. *et al.*, A high-temperature ferromagnetic topological insulating phase by proximity coupling. *Nature* **533**, 513-516 (2016).

163 Wadley, P. *et al.*, Electrical switching of an antiferromagnet. *Science* (2016).

164 He, Q.L. *et al.*, Tailoring Exchange Couplings in Magnetic Topological Insulator/Antiferromagnet Heterostructures. *arXiv:1605.04854* (2016).

165 Jiang, W. *et al.*, Blowing magnetic skyrmion bubbles. *Science* **349**, 283-286 (2015).

166 Yu, G. *et al.*, Room-Temperature Creation and Spin–Orbit Torque Manipulation of Skyrmions in Thin Films with Engineered Asymmetry. *Nano Lett.* **16**, 1981-1988 (2016).